Summer 2017

Novel applications of pulse pre-pump Brillouin Optical Time Domain Analysis for behavior evaluation of structures under thermal and mechanical loading

Yi Bao

Department: Civil, Architectural and Environmental Engineering

NOVEL APPLICATIONS OF PULSE PRE-PUMP BRILLOUIN OPTICAL TIME DOMAIN ANALYSIS FOR BEHAVIOR EVALUATION OF STRUCTURES UNDER THERMAL AND MECHANICAL LOADING

by

YI BAO

A DISSERTATION

Presented to the Faculty of the Graduate School of the

MISSOURI UNIVERSITY OF SCIENCE AND TECHNOLOGY

In Partial Fulfillment of the Requirements for the Degree

DOCTOR OF PHILOSOPHY

in

CIVIL ENGINEERING

2017

Approved by

Dr. Genda Chen, Advisor
Dr. Lesley Sneed
Dr. John Myers
Dr. Mohamed ElGawady
Dr. Xiaodong Yang

ABSTRACT

This study aims to: (1) develop an analytical model for the strain transfer effect of distributed fiber optic sensors in a uniform or non-uniform stress field; (2) develop a measurement approach to monitor strains in concrete and detect damage (e.g. crack and delamination) in bonded and unbonded concrete overlays; (3) characterize the strain and temperature sensitivities of distributed fiber optic sensors at elevated temperatures; (4) develop a thermal annealing approach to enhance the thermal stability and temperature sensitivity of the distributed sensors; and (5) apply the distributed sensors to assess structural behaviors of concrete and steel structures exposed to fire. The pulse pre-pump Brillouin Optical Time Domain Analysis (PPP-BOTDA) was employed to measure strain and temperature distributions along a fused silica single-mode optical fiber. Strain distributions in concrete were measured from the distributed fiber optic sensors embedded in bonded and unbonded concrete overlays. Peaks of the strain distributions represent the effect of concrete cracks and delamination. The strain sensitivity coefficient of distributed sensors was reduced from 0.054 MHz/με to 0.042 MHz/με when temperature increased from 22 ºC to 750 ºC. The temperature sensitivity coefficient of distributed sensors was reduced from 1.349×10^{-3} GHz/ºC to 0.419×10^{-3} GHz/ºC when temperature increased from 22 ºC to 1000 ºC. The distributed sensors embedded in concrete beams measured non-uniform temperature distributions with local peaks representing a sudden increase of temperature through concrete cracks. Temperature distributions measured from the distributed sensors attached on steel beams enabled an enhanced thermo-mechanical analysis to understand the structural behaviors of steel beams subjected to fire.

ACKNOWLEDGEMENTS

I would like to express my sincere gratitude to Dr. Genda Chen for offering great opportunities and providing consistent guidance, advice, and encouragement to support my study at Missouri University of Science and Technology (MST). I am deeply grateful for the great opportunities and wonderful working environment offered by Dr. Chen. It has been a great privilege and a pleasure to have worked with him.

Appreciation is extended to the members of the advisory committee, Dr. Lesley Sneed, Dr. John J. Myers, Dr. Mohamed ElGawady, and Dr. Xiaodong Yang, for their valuable time and efforts to review my dissertation.

I really appreciate the opportunities offered by Dr. Kamal H. Khayat and Dr. John J. Myers for collaborative, cutting-edge researches, and the strong supports of Dr. Franklin Y. Cheng, Dr. Chen, and Dr. Joel Burken for enabling me to independently teach a course *Structural Analysis* for two semesters, which was an exceptional opportunity to a Ph.D. student. I appreciate the assistance from my fellow colleagues and friends during the memorable hours inside and outside of the National Fire Research Laboratory at National Institute of Standards and Technology and the Highbay Structures Laboratory at MST, including Matthew Hoehler, Christopher Smith, Matthew Bundy, Garry Abott, Brian, Greg, Jason, John, Mahdi, Fujian, Yizheng, Yan, Steve, Liang and Zhaochao. Mahdi provided some important data of the mechanical properties of the ultra-high-performance concrete as seen in Section 3.3.2. I also received much assistance from Jeannie, Jody, Darlene, Becky, Marsha and Angel.

I would like to acknowledge the financial supports from National Institute of Standards and Technology [grant number 70NANB13H183], U.S. Department of Transportation [grant numbers DTRT06-G-0014-NUTC], Mid-America Transportation Center [grant number 25-1121-0003-196], and the Missouri University of Science and Technology Inaugural Franklin Y. Cheng Teaching Scholar Program.

Finally, I wish to express special and sincere gratitude to my parents, Guofang Zhang and Jianshe Bao, my parents-in-law, Xianqing Liang and Jinhua Meng, my wife Weina, my sister Yan, and my brother-in-law Liwei for their consistent love, care, understanding, encouragement and supports.

TABLE OF CONTENTS

LIST OF ILLUSTRATIONS

Page

LIST OF TABLES

Page

1. INTRODUCTION

1.1. BACKGROUND

Civil infrastructures are aging worldwide, in particular, in developed countries such as the United States. For instance, the ages of most constructed bridges are approaching their designed service life. Thus, the health conditions of civil infrastructures concern public welfare and safety. For example, collapse of bridges or buildings, leaking fuel, or cracks in nuclear reactors can lead to catastrophic disasters. Therefore, structural health monitoring is of critical importance to society. Financial investments, personal properties, and human lives can be protected by identifying the signs of structural failure early and then preventing catastrophes from occurring. To date, a variety of structural health monitoring technologies have been developed to address different parts of potential structural problems.

Vibrations of structures under the environmental excitations or stimulations applied by human beings have been analyzed to identify the changes of structural system's parameters, such as natural frequency and stiffness, which indicate the changes of structural health conditions. Typically, dynamic data of accelerations, velocities, or displacements are measured to identify the structural system's parameters. A reduction in stiffness could indicate initiation or propagation of damages such as cracks. However, this category of approaches has some issues (Farrar and Worden 2007, Farrar and Lieven 2007). First, low frequency global vibration modes tend to be insensitive to local damages of a structure. Second, there are a large number of factors that influence the measured system responses.

For these reasons, a variety of other structural health monitoring technologies have been developed, based on the development of nondestructive evaluation or sensing technologies. Various nondestructive evaluation techniques have been proposed and successfully implemented to detect deterioration in concrete structures, such as magnetic waves (Jammalamadaka et al. 2008), ultrasonic wave (Blackshire and Sathish 2002), acoustic wave (Semperlotti and Conlon 2010), and thermography (Wang et al. 2006). However, to detect cracks inside concrete is a real challenge due to the highly-heterogeneous material properties of concrete. More importantly, it is difficult to quantify

the initiation and propagation of interfacial delamination with the nondestructive evaluation techniques. Among the various technologies, fiber optic sensors have been extensively studied in the past few decades, due to their unique characteristics such as high sensitivity, high accuracy, immunity to electromagnetic interference, multiplexing capability, and excellent resistance to corrosion and harsh environments (e.g. high temperature, acidic, high pressure, etc.). In the literature, a variety of fiber optic sensors have been developed to provide effective tools for measurement of physical parameters (e.g. temperature, strain, pressure, refractive index, current/voltage, etc.) and chemicals.

1.2. LITERATURE REVIEW ON FIBER OPTIC SENSORS

Fiber optic sensors are made of optical fibers, which have been fabricated using various transparent materials such as fused silica, sapphire, polymers, and etc. According to the number of waveguide modes, optical fibers can be categorized into single-mode fibers (SMFs) and multi-mode fibers (MMFs). Only one transverse mode is allowed in SMFs, while MMFs allow for multiple modes due to the increased dimension of fiber core. Typically, an SMF consists of a fiber core (8.2 μm), a cladding (125 μm), and one or multiple layers of protective coating to enhance the mechanical performance, as illustrated in Figure 1.1(a). A light wave is launched from one end of the fiber, and travels along the fiber length through total internal reflection at the core-cladding interface, as shown in Figure 1.1(b).

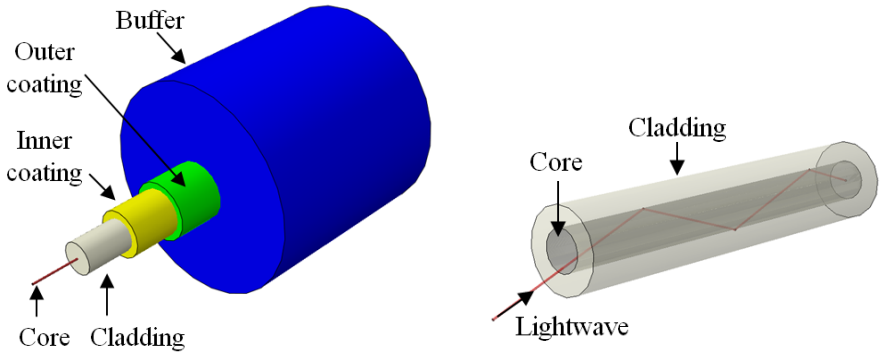

(a) Structure (b) Waveguide

Figure 1.1. Illustration of a typical single-mode fiber

In general, fiber optic sensors can be categorized into grating sensors, interferometer sensors, and distributed sensors (Bao and Chen 2011, 2012). Compared with the distributed sensors that allow for the fully distributed measurements of temperature and strain (Bao and Chen 2015), grating sensors and interferometric sensors are referred to as point (or localized) sensors, which only allow for the measurement at the location where the sensor is deployed. Grating sensors were multiplexed and achieve simultaneous measurements at multiple locations (Kersey et al. 1993). However, since the number of measuring locations is limited, the multiplexed sensors are namely quasi-distributed sensors. A point sensor is relatively short in length, and typically provides a single measurement location over its gage length. A distributed sensor can be far longer than the point sensors and provide spatially-distributed measurements, which are promising for structural health monitoring of large scale structures (Chen and Bao 2011). The fundamental principles, structures, fabrications, and recent development of grating sensors, interferometer sensors, and distributed sensors are reviewed in this section.

1.2.1. Fiber Grating Sensors. Fiber optic grating sensors are based on gratings inscribed in an optical fiber. Optical fiber gratings represent periodic perturbation of the refractive index along the fiber length. In optical fiber gratings, the phase-matching condition can be described by equation (1.1) (Bhatia and Vengsarkar 1996):

$$\beta_1 - \beta_2 = \Delta\beta = 2\pi/\Lambda \tag{1.1}$$

where Λ represents the period of the grating, β_1 and β_2 are the two propagation constants of the modes being coupled, and $\Delta\beta$ is the difference between the two propagation constants. Depending on the period, fiber gratings are classified into fiber Bragg gratings (FBGs) and long period fiber gratings (LPFGs). In an FBG, the forward-propagating fundamental mode (LP_{01}, $\beta_1 = \beta_{01}$) couples to the reverse-propagating fundamental mode ($\beta_2 = -\beta_{01} < 0$), resulting in a large $\Delta\beta$ and thus a small period, which is typically less than 1 μm. However, an LPFG couples the fundamental mode to forward-propagating cladding modes ($\beta_2 > 0$), resulting in relatively long periods, which are typically greater than 100 μm.

In an FBG sensor, a narrow band of the incident optical field within the fiber is reflected by successive, coherent scattering from the index variations, as illustrated in

Figure 1.2. The strongest interaction or mode coupling occurs at the Bragg wavelength (Hill and Meltz 1997), as described by equation (1.2):

$$\lambda_B = 2n_{eff}\Lambda_B \quad (1.2)$$

where λ_B, n_{eff} , and Λ_B represents the Bragg wavelength of FBG, effective refractive index of the fiber core, and the period of grating. Equation (2) indicates that the Bragg wavelength is governed by n_{eff} and Λ_B. Thus, any factor that causes a change of n_{eff} or Λ_B leads to a wavelength shift. Typically, FBGs deployed as sensors have lengths of the order of 5 mm.

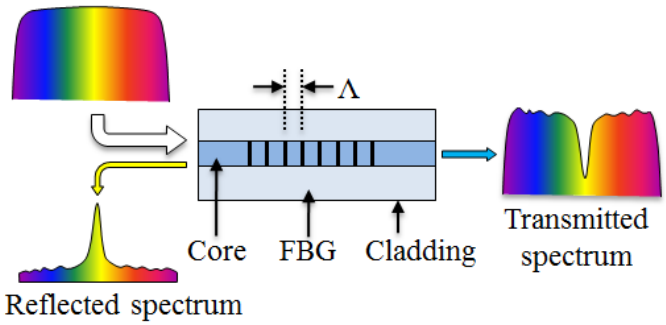

Figure 1.2. Illustration of reflection of FBG

FBGs were first fabricated using the internal writing (Hill et al. 1978) and the holographic technique (Meltz et al. 1989). Both these methods have been superseded by the phase mask technique (Hill et al. 1993; Anderson et al. 1993), which is available to fabricate gratings with controlled spectral response characteristics. However, the phase mask approach requires photosensitivity of the fiber core material. Another method to fabricate gratings is to use the point-by-point writing technique, which is not very efficient for gratings with many index perturbations. However, it is effective for making LPFGs that have coarse gratings with pitches of the order of 100 μm (Hill et al. 1990).

The formation process of gratings has significant effects on their sensing characteristics, in particular, stability at high temperature. Based on the formation mechanism, traditionally, FBGs have been primarily categorized into Type I and Type II (Canning 2008). Type I gratings form through a single ultraviolet (UV) photon absorption process that excites oxygen deficiency centers in fiber core (Meltz et al. 1989). At elevated temperatures, Type I gratings decay as a result of the thermal

depopulation of trapped excited states that are created during the grating formation, because atoms at excited state can absorb energy and return to the ground state. Thus, Type I gratings are typically unsuitable for applications over 400 °C. The refractive index change is almost completely annealed at temperatures over 600 °C. Type II gratings are formed using high power pulsed UV laser sources to locally damage the fiber core or the core-cladding interface, resulting in periodic perturbation of refractive index (Archambault et al. 1993). The damage-type gratings in fused silica fiber were reported to be stable at temperatures more than 1000 °C (Askins et al. 1994). Therefore, Type II gratings are more suitable for high temperature applications.

The thermal stability of gratings can be enhanced by regenerated grating techniques. Regenerated gratings were developed through a hydrogen loading process for high temperature applications (Fokine 2004; Bandyopadhyay et al. 2008; Canning et al. 2008; Lindner et al. 2009). An optical fiber is exposed to high pressure hydrogen gas at room temperature until saturated with hydrogen gas that permeates the glass matrix. The fiber is then exposed to UV irradiation that results in formation of highly reflective seed gratings, which are completely or partially bleached out in a thermal annealing treatment (Fokine 2004). Then, further heating at high temperature generates new gratings, namely regenerated gratings, which have smooth spectra and are stable at temperatures above 1000 °C for silica fibers (Zhang and Kahrizi 2007; Li et al. 2009). With a regenerated FBG, temperature measurements up to 1295 °C have been demonstrated (Canning et al. 2008). The drawbacks of regenerated gratings include cumbersome production and low reflectivity which to some extent limits the capability to be connected in series and form a quasi-distributed sensor.

In recent years, microfabrication techniques using femtosecond (fs) lasers has been extensively exploited to write FBGs in optical fibers without requirement of photosensitivity of the fiber core (Martinez et al. 2004; Mihailov et al. 2004). Both Type I and Type II gratings have been formed using femtosecond laser and a phase mask (Smelser et al. 2005). Optical fiber absorbs energy from femtosecond laser through nonlinear phenomena such as multiphoton, tunneling, and avalanche ionization (Mihailov 2012). The absorbed energy causes material damages, which lead to formation of void like grating structures (Mihailov et al. 2004). FBGs fabricated in fused silica fibers using

femtosecond laser allowed for stable measurements at 1000 °C for about 400 hours, but a permanent drift of the central wavelength was observed at 1050 °C (Grobnic et al. 2006). Thermal annealing at high temperature was applied to enhance the thermal stability of FBGs fabricated using femtosecond laser (Li et al. 2008). After pre-annealing treatment at 1100 °C, the FBGs demonstrated sustained reflectivity at up to 1200 °C for more than 20 hours (Li et al. 2009).

The operating temperature of gratings is limited by the softening/melting point of the fiber material. The softening points of silica fibers are around 1200–1600 °C, depending on the content of additive materials. Single-crystal sapphire has a melting point around 2050 °C and thus might be a good option to overcome the temperature limit of fused silica fiber optic sensors. FBGs inscribed in sapphire fibers have been reported to allow for the measurements up to 1850 °C (Grobnic et al. 2004; Busch et al. 2009; Mihailov et al. 2010; Elsmann et al. 2013). Femtosecond lasers were used to fabricate the FBGs in sapphire fibers, since they provided high peak intensities and multi-photon processes to permanently change the refractive index. However, being different from the fused silica fibers, sapphire fibers typically do not have fiber cladding and are multimode fibers, which involve more significant signal loss and need more complex interrogators. Besides, sapphire fibers have relatively rough surface compared with silica fibers. Thus, light waves are constrained by the interface between fiber core and the environment. The guiding properties of sapphire fibers are very sensitive to the environmental conditions and surface defects.

Conventional FBG sensors were used to measure gas temperature in a down-scale tunnel during a fire experiment (Lonnermark et al. 2008). The FBG sensors were subjected to varying temperatures that were less than 300 °C. Thus, FBG sensors offered temperature measurement results that were believed to be closer to the true gas temperatures than the measurement results from thermocouples. Regenerated FBG sensors were placed close to the surface of two concrete beams that were exposed to ISO 834 fire in a furnace for one hour (Rinaudo et al. 2015). During the test the FBG sensors measured temperatures of about 970 °C and were directly subjected to flames and high temperature increments in the order of 200 °C/min. The FBG sensor results were validated by thermocouples that were installed close to the FBG sensors on the concrete

beams. The validated regenerated FBG sensors were then used to measure temperature in a reinforced concrete beam (Torres Górriz et al. 2017). The measured temperature was up to 953 °C.

Different from FBGs, which are short fiber gratings that only involve waveguide in the core surrounded by cladding, there are two waveguide structures in an optical fiber with LPFG: (1) the core surrounded by cladding, and (2) the cladding surrounded by the environment (e.g. air). Phase matching of the guided core mode and a forward-propagating cladding mode occurs at the resonance wavelength λ, which is described in equation (1.3) (James and Tatam 2003):

$$\lambda = [n_{eff}(\lambda) - n^{i}_{clad}(\lambda)]\, \Lambda \tag{1.3}$$

where $n_{eff}(\lambda)$ is the effective refractive index of the propagating core mode at the wavelength λ, and $n^{i}_{clad}(\lambda)$ is the refractive index of the i^{th} cladding mode.

The high attenuation of the cladding modes of LPFG results in the transmission spectrum of the fiber containing a series of attenuation bands centered at discrete wavelengths, each attenuation band corresponding to the coupling to a different cladding mode (James and Tatam 2003). The exact form of the spectrum and the center wavelengths of the attenuation bands are sensitive to the period and length of the LPFG and to the local environment: temperature, strain, bending radius, and the refractive index of the medium surrounding the fiber (Chen et al. 2016). Changes in these parameters can modify the period of LPFG and/or the differential refractive index of the core and cladding modes. Typically, a higher order of coupling mode corresponds to a greater romance wavelength and larger intensity of transmission loss. As temperature changes, the resonance wavelengths are shifted, and the shifted quantity of resonance wavelength can be measured to calibrate the temperature sensitivity of the LPFG.

Typically, the period of LPFG is in the range 100 μm to 1 mm, and the length of LPFG is at the order of 30 mm. The phase mask technique and point-by-point writing technique used to fabricate FBGs also can be used to fabricate LPFGs (James and Tatam 2003). While the phase mask and UV exposure method is widely used for fabrication of FBGs, the point-by-point writing technique is convenient to use for fabrication of LPFGs because of the relatively large periodicity. Besides UV irradiation, CO_2 lasers (Davis et al. 1998) and femtosecond laser (Kondo et al 1999) have been used. Moreover, LPFGs

have been fabricated by ion implantation (Guan et al. 2000), diffusion of dopants (Dianov et al. 1997), relaxation of mechanical stress (Kim et al. 2000), and electrical discharges (Rego et al. 2001). In a PCF, LPFGs were fabricated by periodically collapsing the holes of the fiber using CO_2 laser (Kakarantzas et al. 2002). Femtosecond lasers have been used to fabricate LPFGs based on densification of the glass. The fabricated LPFG allowed for measurements at temperatures up to 500 °C (Kondo et al. 1999). LPFGs fabricated by CO_2 laser irradiation were reported to be stable at 1200 °C (Davis et al. 1998). Electric arc fabrication of an LPFG relies upon a combination of up to four effects to generate the periodic modulation of the fiber properties. The mechanisms exploited include the induction of microbends into the fiber (Hwang et al. 1999), the periodic tapering of the fiber (Kakarantzas et al. 2001), the diffusion of dopants (Dianov et al. 1997), and the relaxation of internal stresses (Rego et al. 2001). Such LPFGs have been shown to operate at temperatures up to 800 °C without permanent modification of their properties (Humbert and Malki 2002), and, if annealed appropriately, they may operate at temperatures up to 1190 °C (Rego et al. 2001).

1.2.2. In-line Fiber Optic Interferometers. A fiber optic interferometer operates on the interference between two light beams that travel along different optical paths of a single fiber or two different fibers. Thus far, four representative types of interferometers have been demonstrated in optical fibers, which include Fabry-Perot interferometers (FPIs), Mach-Zehnder interferometers (MZIs), Michelson interferometers (MIs), and Sagnac interferometers (SIs).

In MZI, MI, and SI, the incident light is split into two arms by a fiber splitter and then recombined by a fiber combiner. Early MZI, MI, and SI had two arms, and thus had disadvantages such as the complicated structure, big size, high susceptibility to environmental changes, etc. Recently, various in-line fiber optic core-cladding-mode interferometers (CCMI) were proposed to replace the two-arm interferometers. Typically, the in-line fiber optic CCMI sensors have been demonstrated in both Mach-Zehnder and Michelson types. The CCMI operates on the interference between the core and the cladding modes, which also requires the splitter and the combiner to realize the coupling and re-coupling between the core mode and the cladding modes. The reference arm and the sensing arm of CCMI are within the same optical fiber, but have different optical

paths owing to the modal dispersion. The CCMIs are more compact and very effective. In general, an in-line FPI consists of two parallel reflecting surfaces separated by a cavity with a physical length of *L*. Typically, in-line FPIs can be categorized into extrinsic FPI (EFPI) which is discontinuous at the cavity and intrinsic FPI (IFPI) which is continuous at the cavity, as illustrated in Figures 1.3(a) and (b). Because of the discontinuity at the cavity, the relative displacement between the two reflecting surfaces is not limited by the strain limit of the optical fiber, and thus, EFPI potentially can be used to measure large strains. Besides, the fabrication of EFPI does not need expensive equipment due to its simple structure. The reflector can be one end of an optical fiber or a mirror with high reflectivity. However, EFPI was reported to have some disadvantages such as low coupling efficiency, requiring careful alignment, and packaging problems. On the other hand, the sensing element of the IFPI is a short section of fiber sandwiched between two reflecting components. Since the light signal of an IFPI propagates in the fiber all the time, a higher intensity optical signal will be obtained, which is better for signal demodulation. However, typically, the fabrication of IFPI requires expensive equipment for the cavity fabrication or special fibers or dangerous chemicals.

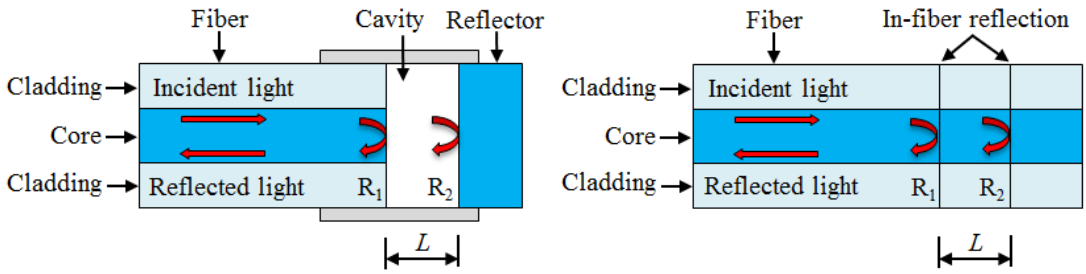

(a) EFPI (b) IFPI

Figure 1.3. Illustration of Fabry-Perot interferometers

Interference occurs between the reflected and transmitted light signals that are coherent waves, at the two reflecting surfaces (R1 and R2). The reflection spectrum of an FPI can be described as the wavelength dependent intensity modulation of the input light spectrum, which is mainly caused by the optical phase difference between two reflected light beams. Constructive interference occurs if the reflected beams are in phase, and this corresponds to a high-transmission peak (Rao 2006). If the reflected beams are out-of-

phase, destructive interference occurs and this corresponds to a reflection minimum. Whether the multiple reflected beams are in phase or not depends on the wavelength (λ) of the incident light (in vacuum), the angle (θ) with which the incident light travels through the reflecting surfaces, the physical length (L) of the cavity, and the refractive index (n) of the material between the reflecting surfaces.

The phase difference between each reflected pair of the EFPI is given as:

$$\phi = \frac{2\pi}{\lambda} 2nL\cos(\theta) \tag{1.4}$$

When perturbation is introduced to an FPI, the phase difference is influenced with the variation in the optical path distance of the interferometer (Rao 2006). Applying longitudinal strain to the FPI sensor, for instance, changes the physical length of the cavity, which results in phase variation. By measuring the shift of the wavelength spectrum, the applied strain can be quantified. FPIs have demonstrated high sensitivity and stability of measurements at high temperature. A number of techniques have been reported to form FPIs, such as thin film deposition (Lee et al. 1988, Mathew et al. 2015), forming a micro-notch by use of femtosecond lasers (Wei et al. 2008), offset structures (Duan et al. 2011), chemical etching (Machavaram et al. 2007, Tafulo et al. 2012), splicing technology (Duan et al. 2012), etc. An FPI sensor was fabricated by creating an internal mirror in fiber by depositing a thin layer (100 nm) of TiO_2 and demonstrated operation at temperatures up to 1050 °C (Lee et al. 1988). Following the same concept, a thin layer of Cr was deposited to enable the FPI sensor to be operated at 1100 °C with a stability of about 10 °C for a duration time of more than 300 hours (Mathew et al. 2015). Micro-machining technique using femtosecond laser was used to fabricate miniature FPIs that were operated at temperatures up to 1100 °C (Wei et al. 2008). An easy-to-fabricate FPI was presented by simply splicing two sections of two fibers with a large lateral offset (~62.5 μm), and allowed for measurement at temperatures up to 1000 °C (Duan et al. 2011). Recently, photonic crystal fibers (PCFs) have attracted worldwide interests because of their unique waveguide mechanisms and modal properties due to their holey structures. A section of PCF was sliced to an SMF to form an FPI, which was operated at temperatures up to 1200 °C (Zhu et al. 2010). Miniature FPIs with a micro-size air bubble were formed by splicing PCF and SMF (Li et al. 2008, Villatoro et al. 2009, Deng et al.

2011). The FPI sensors were operated at temperatures up to 1000 °C (Zhu et al. 2012). Moreover, sapphire fibers have been used to fabricate FPIs that were operated at temperatures exceeding 1000 °C (Wang et al. 2010, Huang et al. 2015).

In-line CCMIs require a splitting and re-coupling mechanism between the core and cladding modes, which are guided by the core-cladding and cladding-ambient interfaces, respectively. The differential phase of the core and cladding modes allow CCMIs to sense many environmental parameters. Typically, there are two types of CCMIs, which are MZI and MI, as illustrated in Figures 1.4(a) and (b), respectively. Both of their structures involve a reference arm and a sensing arm. The main difference between MZI and MI is the MZI requires two couplers, while the MI only needs one coupler that splits and re-combines the two beams due to the use of mirrors in the reference and sensing arms. Therefore, MZI and MI sensors measure the transmitted signals and reflected signals, respectively.

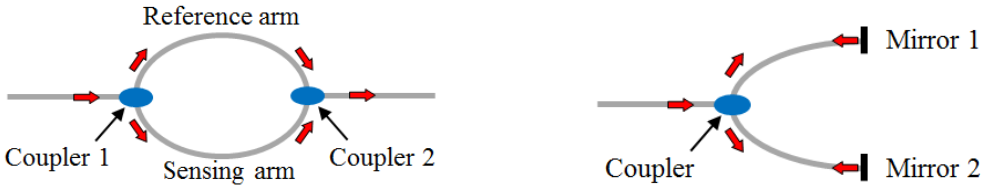

(a) MZI (b) MI

Figure 1.4. Illustration of core-cladding-mode interferometers

In a MZI, there are a splitter to partially couple the energy of the core mode into cladding modes and a combiner to recombine the cladding modes into the core. The phase difference of the core and cladding modes could be described as:

$$\Phi_{MZI} = \frac{2\pi[n_{eff}(\lambda) - n^{i}_{clad}(\lambda)]L}{\lambda} \tag{1.5}$$

where $n_{eff}(\lambda)$ is the effective refractive index of the propagating core mode at the wavelength λ, $n^{i}_{clad}(\lambda)$ is the refractive index of the i^{th} cladding mode, and L is the physical fiber length between the splitter and the combiner.

A pair of LPFGs was used as the splitters/combiners to form a MZI, as illustrated in Figure 1.5(a) (Allsop et al. 2002). The operating temperature and wavelength of the MZI were limited by the LPFGs. Besides, the fabrication of LPFGs requires expensive

equipment. An easy way to partially couple the core mode beam to cladding modes is to splice two fibers with a small lateral offset, as depicted in Figure 1.5(b). The number of coupled cladding modes can be controlled by adjusting the amount of offset. Another method for splitting the beam in a fiber is to use the fibers having different core sizes as shown in Figures 1.5(c) and (d). In Figure 1.5(c), a short piece of multimode fiber is spliced to a conventional SMF at two points (Villatoro and Monzón-Hernández 2006, Ngyuen et al. 2008). In Figure 1.5(d), a small length of fiber with small core is spliced in between two conventional SMFs (Zhu et al. 2010). Those sensors have been operated at temperatures up to 850–1000 °C. Collapsing air holes of a PCF is another good way of making an in-line MZI, as shown in Figure 1.5(e) (Choi et al. 2007). It was pointed out that the sensor potentially could be operated at high temperature. However, the high temperature sensing performance was not investigated. Figures 1.5(f) and (g) show the in-line MZIs with air-holes which was formed using a femtosecond laser based microfabrication technique (Jiang et al. 2011, Wang et al. 2010). The MZIs were proven to allow for the measurement of temperatures up to 1100°C to 1200 °C. Moreover, a tapered structure was proposed to form an effective in-line MZI as shown in Figure 1.5(h) (Monzón-Hernández et al. 2006, Lu et al. 2009). The tapering increases the core mode diameter, so the core mode and cladding modes could be coupled. However, the high temperature sensing performance has not been evaluated.

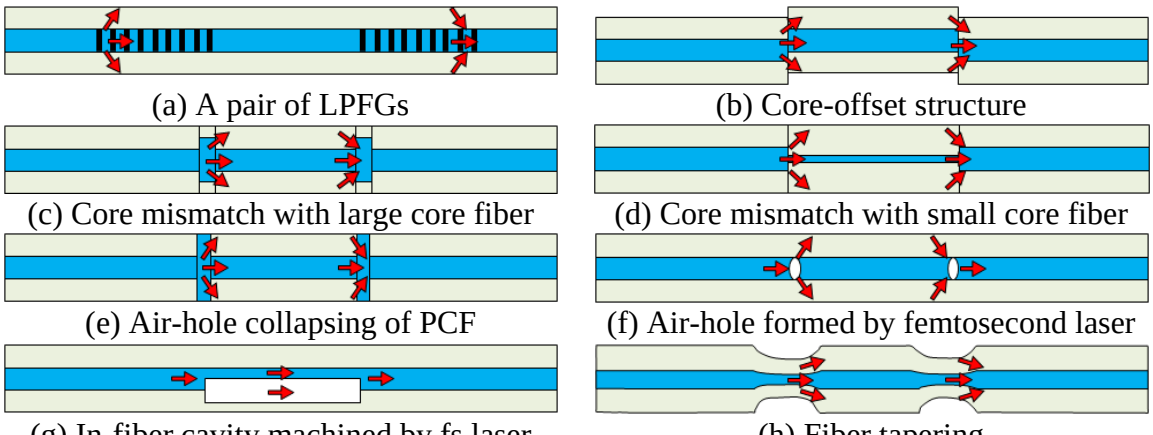

Figure 1.5. Configuration of various types of in-line Mach-Zehnder interferometers

In an MI, each beam is reflected at the end of each arm. The phase difference of the core and cladding modes could be described as:

$$\Phi_{MI} = \frac{4\pi[n_{eff}(\lambda) - n^{i}_{clad}(\lambda)]L}{\lambda} \tag{1.6}$$

where $n_{eff}(\lambda)$ is the effective refractive index of the propagating core mode at the wavelength λ; $n^{i}_{clad}(\lambda)$ is the refractive index of the i^{th} cladding mode; and L is the physical fiber length between the coupler and the mirrors.

The structure of an MI is like a half of the structure of an MZI, as illustrated in Figures 1.6(a)–(d) (Swart 2004, Tian et al. 2008a,b, Li et al. 2006). The fabrication method and the operation principle of MIs are almost the same as MZIs. Since MIs use reflection modes, they are compact and handy in practical uses and installation.

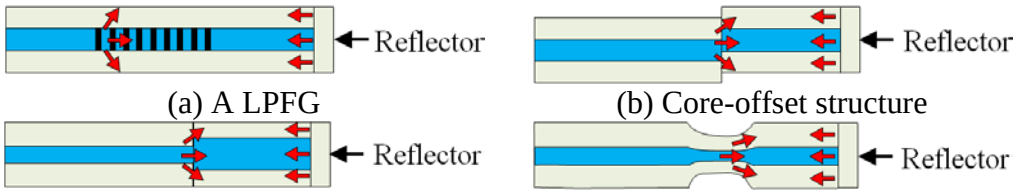

(a) A LPFG (b) Core-offset structure

(c) Core mismatch (d) Fiber taper

Figure 1.6. Configuration of two types of in-line Michelson interferometers

1.2.3. Distributed Fiber Optic Sensors. Unlike the grating and interferometer sensors, fused silica SMFs can be used as distributed fiber optic sensors based on light scatterings (Bao and Chen 2011), with no dependence on gratings or cavity, and thus, the distributed sensors can potentially be operated at higher temperatures. Distributed fiber optic sensing technologies have attracted intensive research interests worldwide due to their cost-effectiveness and fully-distributed sensing ability. When light propagates in an optical fiber, it interacts with the atoms/molecules of the medium, generating scattering signals. Typically, there are three types of scatterings in an optical fiber, including Rayleigh scattering, Brillouin scattering, and Raman scattering, as illustrated in Figure 1.7 (Bao and Chen 2012).

Rayleigh scattering results from the interaction between light wave and tiny particles in the medium. It is an elastic scattering process which does not involve any

frequency change. Different from Rayleigh scattering, Brillouin scattering and Raman scattering are inelastic scatterings that involve frequency changes. Brillouin scattering results from the interactions between light and acoustic waves. Raman scattering is caused by the interactions between light wave and molecular vibrations. Raman spectra usually contain many sharp bands separated by the electronic vibration, each resulting from molecular rotation or reorientation excitations. Based on light scatterings, different distributed fiber optic sensing technologies have been developed in the literature.

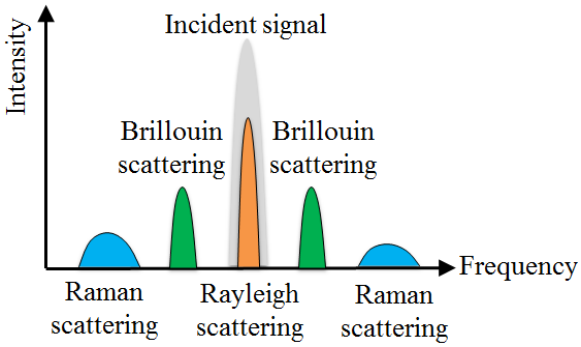

Figure 1.7. Light scatterings in optical fiber

The intensity of Rayleigh backscattering was mapped along the length of an optical fiber using an optical time domain reflectometry (OTDR) technology, which was first developed to detect fault in telecommunication cables (Barnoski et al. 1977). Later, it was applied to measure strain, temperature, and displacement (Yilmaz and Karlik 2006, Pinto et al. 2006, Wan and Leung 2007). A coherent OTDR was developed by mixing the backscattered and reference lights with a coherent detection technique (Takada et al. 1991). Because the distances between scattering centers (i.e. particles) are smaller than the wavelength of light in the optical fiber, the secondary light waves from Rayleigh scattering are coherent. Generally, the spatial resolutions of OTDR technologies are related to the pulse width in optical domain and thus the bandwidth of the detector, electrical amplifier and digitizer in electronic and digital domains. Millimeter spatial resolution measurement will require a bandwidth in the range of tens of GHz and will thus require a very expensive and sophisticated system (Bao and Chen 2011, 2012). Alternatively, optical frequency domain reflectometry (OFDR) can convert the frequency response into time domain by Fourier transform so that the spatial resolution with OFDR

does not depend on bandwidth of the detector or digitizer (Soller et al. 2005). The intensity of Raman scattering is dependent on temperature, which provides the physical basis for measurement of absolute temperature using an optical fiber (Dakin et al. 1985). Based on Raman scattering, Raman optical time domain reflectometry (ROTDR) and Raman frequency time domain reflectometry (ROFDR) have been developed for temperature measurement (Dakin et al. 1985, Bao and Chen 2011). Typically, the spatial resolution of ROTDR was limited to about 1 m with a measurement distance of 10 km, due to the relatively low intensity of Raman scattering. The 1 m spatial resolution is insufficient for many applications, such as detection of fire or hot spots along the steam pipes of power plants, where spatial resolution much better than 1 m is required. Recently, a superconducting nanowire single-photon detector was developed and utilized to improve the spatial resolution of ROTDR to the order of 1 cm at 1550 nm wavelength in a SMF (Tanner et al. 2011).

The first demonstration of distribution of Brillouin scattering spectrum along the length of an optical fiber was achieved through Brillouin optical time domain analysis (BOTDA) (Horiguchi et al. 1989). BOTDA measures the backscattering signal in an optical fiber due to the combined effect of strains and temperatures as a result of a forward-propagating pulse pump light wave and a back-propagating continuous probe wave. When the probe wave is at the Stokes frequency, Brillouin gain will happen. If the pump and probe waves are tuned to have time-varying frequency differences corresponding to the Brillouin frequency of optical fiber, the Brillouin gain as a function of position can be determined by the time-varying probe wave. In this way, the Brillouin frequency can be mapped along the optical fiber, which enables the measurements of strain and temperature distributions (Brown and Hartog 2002, Belal et al. 2010). Brillouin optical time domain reflectometry (BOTDR) was proposed with the advantage of one-end measurement (Shimizu et al. 1993). However, the spatial resolution is at a meter order, which is mainly limited by the pulse width. Narrower bandwidth pulse can lead to higher resolution. However, it may not be able to stimulate sufficient acoustic waves. To generate significant stimulated Brillouin scattering, the pulse bandwidth must be longer than the phonon relaxation time. It has been demonstrated that 28 ns is required to get the phonon fully stimulated, which corresponds to a ~3 m spatial resolution. To resolve this

problem, pulse pre-pump BOTDA (PPP-BOTDA) was proposed to take advantage of a pre-pump pulse that stimulates the phonon before a narrow bandwidth pulse arrives and thus a spatial resolution at centimeter level has been achieved, as illustrated in Figure 1.8 (Kishida and Li 2006). On the other hand, frequency domain distributed sensing technologies have been developed such as Brillouin optical frequency domain analysis (BOFDA) (Garus et al. 1997) and Brillouin optical correlation domain analysis (BOCDA) (Hotate and Hasegawa 2000). In a short distance (e.g. ~10 m), the spatial resolution was 3 cm by BOFDA and 1 cm by BOCDA (Hotate and Tanaka 2002). The spatial resolution was 7 cm for a 1 km measurement distance (Hotate 2011).

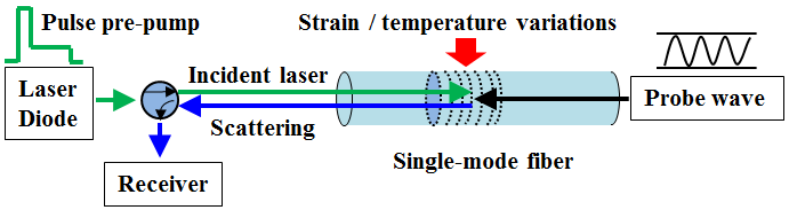

Figure 1.8. Illustration of PPP-BOTDA

The frequency of Brillouin backscattering in an optical fiber is denoted as ν_B, which is on the order of 9 GHz to 13 GHz for light waves of a wavelength of 1.3 μm to 1.6 μm in a SMF, and can be given by (Bao and Chen 2012):

$$\nu_B = \frac{2\nu_0}{C} n_{eff} V_a \tag{1.7}$$

where ν_0 denotes the frequency of the input light wave, n_{eff} denotes the effective refractive index of the optical fiber, V_a denotes the speed of acoustic wave or sound, C (= 3.0×10^8 m/s) denotes the speed of light in vacuum.

The speed of the acoustic wave is in turn given by (Bao and Chen 2012):

$$V_a = \sqrt{\frac{(1-\mu)E}{(1+\mu)(1-2\mu)\rho}} \tag{1.8}$$

where μ, E, and ρ denote the Poisson's ratio, the Young's modulus, and the density of fused silica fiber, respectively. The Poisson's ratio and the Young's modulus are related to temperature. The refractive index and density are related to temperature and strain. Therefore, the Brillouin frequency depends on both strain and temperature.

A fused silica SMF with side-holes was characterized as a distributed temperature sensor with BOTDA at temperatures up to 1000 ºC (Wang 2013). A linear relationship between the Brillouin frequency and temperature was reported. Nonlinear relationships were demonstrated by other investigators using fused silica SMFs without side-holes (Fellay 2003, Li et al. 2003). The distributed temperature sensor allowed for the measurements of temperature up to 850 ºC (Li et al. 2003). Bao and Chen (2016a) developed an annealing treatment approach to increase the thermal stability and temperature sensitivity of fused silica SMF. The operating temperature was increased to 1000 ºC with an excellent heating-cooling stability. Besides the measurement of temperature, Bao and Chen (2016b) investigated the strain sensing performance of a distributed fiber optic sensor at temperatures up to 800 ºC. The distributed fiber optic sensor was passed through the furnace back and forth and formed a loop with the Neubrescope for PPP-BOTDA measurement. The two portions of the fiber passing through the furnace were parallel and closely spaced. One portion was free of strain, referred to as temperature sensor, while the other was fixed to the translation stage and subjected to strain, referred to as strain/temperature sensor. The temperature sensor provided temperature compensation to the measurement by the strain/temperature sensor.

1.2.4. Applications of Fiber Optic Sensors in Damage Detection. Point sensing and nondestructive evaluation technologies have been developed to monitor strain and cracking in concrete structures. For example, vibrating wires and FBG were embedded in concrete pavement to measure local strains and, by identifying sudden jumps in the strain measurements, perhaps detected one or more cracks when they happen to cross the sensors over their gauge length (Lu and Xie 2007, Azenha et al. 2009, Stephen 2012). Multiple FBG sensors were connected in series and multiplexed to increase the likelihood of crack detection with a quasi-distributed fiber optic sensor network (Zhao and Ansari 2001). Micro-electromechanical sensors and piezoelectric sensors were embedded in pavement to measure localized temperature and strain (Ceylan et al. 2011, Lajnef et al. 2013, Xu et al. 2015, Alavi et al. 2016).

In general, point sensors have three disadvantages: (i) low in success rate for the detection of unknown cracks, (ii) costly for a long distance deployment of highway roads, and (iii) inaccurate in strain measurement in thin pavement overlays, since the dimension

of sensors is often comparable with the overlay's thickness, and thus can significantly influence the strain field. Distributed sensing technology may be advantageous over the point sensing and nondestructive evaluation technologies. For example, coaxial cable sensors were invented and successfully applied to measure strain distributions and detect a wide range of cracks from visually invisible to excessive corresponding to the failure of a full-scale reinforced concrete girder (Chen et al. 2005). However, coaxial cable sensors are presently unavailable in market and their measurement is potentially affected by passing vehicles on highways since the electromagnetic signals travelling in the cables are not immune to electromagnetic interference.

Considering these constraints, distributed fiber optic sensors are likely a better choice for this application due to cost effectiveness, immunity to electromagnetic interference, and robustness in harsh environments (Bao and Chen 2012). Optical time domain reflectometry (OTDR) was used to detect multiple cracks in concrete based on Rayleigh scattering. In this case, the crack orientations must be known and their associated strains cannot be measured (Leung et al. 2000). Both BOTDA and BOTDR were developed and applied to measure strain and temperature distributions over a long distance (Bao and Chen 2012). However, the spatial resolution of conventional BOTDA and BOTDR is generally low to detect multiple micro cracks (Wu et al. 2008). The best spatial resolution of 150 mm was reported by using a multiple peak fitting technique (Deif et al. 2010). A special installation of the sensor was applied to manipulate delamination between the optical fiber and the monitored host (Glisic and Inaudi 2011). The delamination resulted in an extra length to average the crack induced length change in the optical fiber, which enable submillimeter cracks to be detected using BOTDA (Glisic and Inaudi 2011). Rayleigh scattering based technologies have also been implemented for distributed strain measurements with improved spatial resolution (Hoult et al. 2014). However, compared with stimulated Brillouin scattering technologies (e.g., BOTDA), the maximum sensing length is limited for Rayleigh scattering and spontaneous Brillouin scattering based technologies (Hoult et al. 2014). PPP-BOTDA was proposed to stimulate the phonon in optical fiber with a long-duration pulse before a short-duration pulse arrives, achieving 20-mm spatial resolution (Kishida et al. 2005).

1.3. RESEARCH OBJECTIVES AND SCOPE OF WORK

The primary research objectives of this study include development, validation, and applications of effective sensing tools for measurement of strain and temperature distributions and detection of damages in concrete and steel structures under normal and high temperature conditions, aiming to improve safety and security of civil infrastructures, extend the service life, and reduce the maintenance costs. To achieve these objectives, the following six tasks were conducted.

1.3.1. Development of Strain Transfer Models for Distributed Fiber Optic Sensors. It is essential to understand the strain transfer effect for distributed fiber optic sensors embedded in different host matrix, in order to use the distributed sensors to measure strain distributions of the host matrix. In this study, a mechanical model of distributed fiber optic sensors embedded in host matrix is employed, and analytical formulae with explicit expressions are derived for different strain field conditions of the host matrix, including uniform and different non-uniform strain fields.

1.3.2. Monitoring of Early-Age Behaviors of Bonded Ultra-High Performance Concrete Overlay. Due to the very low water-to-cementitious materials ratio, typically, ultra-high performance concrete (UHPC) is subjected to relatively large autogenous shrinkage, which may cause cracks and delamination in laminated composite structures at early age. In this study, distributed fiber optic sensors made of telecommunication-grade fused silica SMFs were used to measure autogenous shrinkage of UHPC, and monitor the initiation and propagation of delamination at the interface between existing concrete substrate and UHPC overlay cast on the top of the substrate. A finite element model incorporating cohesive elements was established to understand the interfacial delamination induced by the shrinkage of UHPC overlay.

1.3.3. Measurement of Strain Distribution and Detection of Cracks in Unbonded Concrete Pavement Overlay. Unbonded concrete pavement overlay is easy and fast to construct and less susceptible to damages in the existing substrate. However, under truck loads, unbonded concrete overlays are subjected to relatively large stress and tend to crack, compared with bonded overlays, in which the overlay and substrate are integrated to resist the vehicle loads. In this study, distributed fiber optic sensors were embedded in concrete overlay to measure the strain distributions along the optical fiber.

1.3.4. Development and Characterization of Distributed Fiber Optic Sensors for High Temperature Applications. A telecommunication-grade fused silica SMF was characterized as a distributed sensor with the PPP-BOTDA technology at temperatures up to 1000 °C. The strain and temperature sensitivity coefficients were experimentally calibrated. A thermal annealing procedure was developed and implemented to enhance the thermal stability of the distributed sensor at high temperature.

1.3.5. Temperature Measurement and Damage Detection in Concrete Beams Exposed to Fire. The distributed fiber optic sensors were embedded in concrete beams which were subjected to fire. The beams were tested at different fire levels which were controlled via the burner's heat release rate. Temperature distributions within the concrete beams were measured from the distributed fiber optic sensors with the PPP-BOTDA technology. Heat transfer analyses were performed to understand the measured temperature distributions. Since the presence of cracks in concrete can change the heat transfer behavior and thus the temperature distributions in concrete beams, the measured temperature distributions enabled detection and localization of cracks in concrete exposed to fire.

1.3.6. Temperature Measurement and Thermomechanical Analysis of Steel Beams Exposed to Fire. The distributed fiber optic sensors were attached on steel beams which were exposed to fire. The beams were tested at different fire levels which were controlled via the burner's heat release rate. Temperature distributions over the entire steel beams and strains at the locations where the sensors were deployed were measured with the PPP-BOTDA technology. Based on the measured temperature distributions, an enhanced thermomechanical analysis was performed to understand the behaviors of the steel beams at elevated temperatures.

1.4. ORGANIZATION OF THIS DISSERTATION

This dissertation consists of eight sections. Each of the first seven sections has been organized as one or two stand-alone papers including a detailed technical review. Section 1 presents a literature review of fiber optic sensors, objectives and scope of work of this study, and the technical tasks that are addressed in the following sections. Section 2 develops the strain transfer models for distributed fiber optic sensors. Section 3 reports

the early age behaviors of ultra-high-performance concrete (UHPC) and UHPC bonded overlay, which have been published in two journal papers on Materials Letters (2015) and Smart Materials and Structures (2017). Both experimental and numerical studies were carried out at different stages of investigation. Section 4 presents a unique application of the distributed fiber optic sensors for measurement of strain distributions and detection of damages in unbonded concrete pavement overlays, which have been published on Optical Engineering (2015) and Smart Structures and Systems (2016). Section 5 presents the development, characterization, and validation of distributed fiber optic sensors for measurement of strain and temperature distributions at elevated temperatures. It is based on two journal papers, which were published on Measurement Science and Technology (2016) and Optics Letters (2016). Sections 6 and 7 respectively report unique applications of the distributed fiber optic sensors in concrete and steel beams subjected to fire. Section 6 is based on a journal paper published on Journal of Structural Engineering (2016). The main research outcomes, findings, and future studies are summarized in Section 8, which also lists the published papers and papers submitted or to be submitted for publication on journals.

2. STRAIN TRANSFER EFFECT IN DISTRIBUTED FIBER OPTIC SENSORS

2.1. BACKGROUND

Fiber optic sensors are typically packaged with protective coating to enhance the mechanical strength and workability for various applications. The strain changes sensed by embedded fiber optic sensors are not necessarily the same as those in the host matrix because of the presence of coatings. This is known as the strain transfer effect, which has been reported for point fiber optic sensors.

Pak (1992) conducted a theoretical study of the strain transfer of a coated fiber optic sensor embedded in host composite matrix based on the mechanics of elasticity. He assumed the host matrix to be infinite and subjected to a far-field longitudinal shear load parallel to both the optical and the structural fibers. He derived closed-form solutions for the strains and strain transfer ratio based on the idealizations, and the model was experimentally validated by Sirkis and Haslach (1991). He deduced that the strain transfer ratio was related to the coating thickness and the ratio of the coating's and the matrix's elastic moduli. Cox (1952) presented a theoretical study of the load transfer from matrix to fiber, namely, shear-lag theory.

Ansari and Yuan (1998) proposed a strain transfer model for a coated optical fiber embedded in a host matrix, based on the shear-lag theory, and experimentally validated the model using a white light Michelson interferometric sensor. They assumed that all materials were linearly elastic, adjacent interfaces were well bonded, and the optical fiber had the same strain change ratio as the matrix at the middle of the sensor. They found that the strain transfer ratio was influenced by the mechanical properties of the coating material and the sensor length. They claimed that for coated optical fibers it was impossible for the strain transfer ratio to achieve 1.0. Subsequently, Duck and Michel (2000) derived an expression of the axial strain distribution for an embedded fiber optic sensor packaged with elastic coating material under an arbitrary strain field. They compared the analytical results with finite element simulations. Li et al. (2002) proposed a theoretical strain transfer model incorporating an ideal elastoplastic coating material. They studied the strain transfer ratio when the coating material worked at different stages (elastic, elastoplastic, plastic, and post-plastic), and experimentally validated the model

using a white light Michelson interferometric sensor. Li et al. (2006) improved the strain transfer model developed by Ansari and Libo (1998). Zhou et al. (2007) developed a strain transfer model for a fiber Bragg grating (FBG) sensor. They conducted parametric studies and came up with a modification factor of about 0.90 to 0.95 based on the strain transfer ratio. Li et al. (2007) presented and experimentally validated a strain transfer model for FBG sensors under non-axial stress and subsequently carried out an error analysis. They found that the sensor's orientation could influence the strain transfer ratio that was up to 0.90 to 0.92. The preceding models did not consider the influence of the host material's mechanical properties on the strain transfer effect. Ling et al. (2005) presented a strain transfer model for a FBG sensor embedded in composite host under a non-uniform strain field. The model incorporated the influence of a multi-layer host matrix. The FBG's reflection spectrum was observed to be broadened or even split into multiple peaks, which was different from a single sharp peak found in a uniform strain field. Li et al. (2009) presented studies on the strain transfer for FBG sensors embedded in different host matrix materials. They demonstrated that the strain transfer ratio was around 0.95 to 0.96. Jiang et al. (1998) proposed theoretical studies that included the impact of the fiber optic sensor on the host matrix.

The previous studies of the strain transfer effect focused on the localized strain sensors, such as FBG and interferometer sensors. Due to the limited sensing length, a localized strain sensor can usually be considered working in uniform strain fields. However, this is not necessarily satisfied for the distributed sensors, which are typically used for measuring non-uniform strain distributions (Bao et al. 2015; Bao and Chen 2016). Therefore, the strain transfer effect on strain measurements using distributed fiber optic sensors needs to be investigated. In addition, the previously-derived formulas for the localized strain sensors were validated in an average sense. Since the localized sensors cannot provide fully-distributed strain measurement, the average strain transfer ratios were derived and correlated to the strain measurements from the localized strain sensors (Ansari and Yuan 1998; Li et al. 2007).

In this study, analytical formulas of the strain transfer for distributed fiber optic sensors packaged with a dual-layer polymer coating was derived based on the shear-lag theory. A general formulation for optical fibers with multi-layer coatings was deduced.

Uniform and non-uniform strain fields were considered. The theoretical formulas were directly validated by the measurements from distributed fiber optic sensors based on the PPP-BOTDA.

2.2. CHARACTERIZATION OF OPTICAL FIBER

In real applications, the optical fiber is usually packaged with protective coatings to prevent the fragile fiber from damage, as illustrated in Figure 1.1. In this study, a SMF (SMF-28e$^+$), referred to as bare fiber (BF), were used as a distributed fiber optic sensor. Each fiber consisted of a glass core (diameter: 8.2 μm), a glass cladding (outer diameter: 125 μm), and two layers of polymeric coating (outer diameter: 242 μm). The inner coating (outer diameter: 190 μm) is usually a soft, rubbery material that cushions the silica from external mechanical loads. The outer coating is stiff and meant to protect the fiber from abrasions and environmental exposure. Both coatings are composed of complex mixtures of raw materials, such as monomers, oligomers, photoinitiators, and additives (Kouzmina *et al*. 2010). The elastic moduli of the silica fiber (E_f), inner coating (E_i), and outer coating (E_o), are 72 GPa, 0.6 MPa, and 2 MPa, respectively. The Poisson's ratios of the fused silica fiber (μ_f), inner coating (μ_i), and outer coating (μ_o), are 0.26, 0.48, and 0.42, respectively.

2.2.1. Mechanical Properties. To understand the strength and deformability, ten optical fibers with a gage length of 250 mm were tested to rupture in tension at a displacement rate of 1 mm/min. Their mechanical properties were evaluated at room temperature (22 °C). Considering the fragility of glass, each fiber was reinforced with protective sleeves at both ends in direct contact with grips of the load frame that had a load capacity of 100 N. The applied load and the fiber elongation were simultaneously recorded so that the load-strain relation can be obtained (Bao et al. 2016). Their average tensile strength and average strain are 22.6 N and 23.3×10^3 με, respectively.

2.2.2. Sensitivity Calibration with PPP-BOTDA. An optical fiber was tested in tension under increasing loads as shown in Figure 2.1(a). At each load, the strain in the optical fiber was simultaneously measured using the Neubrescope and the load frame.

The Neubrescope measures the Brillouin frequency shift that can be correlated to the strain change when the ambient temperature is kept constant. Given the initial length

of the optical fiber, the strain values can be calculated from the elongation measurement by an extensometer of the load frame. Figure 2.1(b) shows the directly measured Brillouin frequency shift as a function of the applied strain obtained from the load frame. The R^2 value for the regression linear line is close to 1.0, indicating a good correlation. The slope of the line (= 5.43×10^{-5} GHz/με) represents the strain sensitivity coefficient.

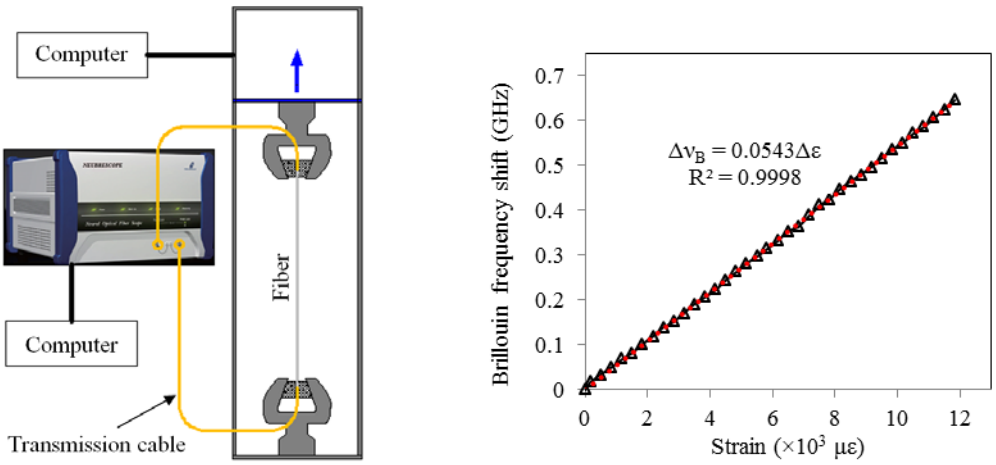

(a) Test setup (b) Strain sensitivity coefficient

Figure 2.1. Calibration of the strain sensitivity of the distributed fiber optic sensor with PPP-BOTDA

2.3. MECHANICAL MODEL OF DISTRIBUTED FIBER OPTIC SENSOR

In this section, first, the controlling equations of strain transfer are derived. Similar work has been introduced by other researchers for localized strain sensors. Then, the general and particular solutions of the controlling equations are sought for distributed fiber optic sensors. Finally, different uniform and non-uniform strain fields are investigated.

2.3.1. Controlling Equations. The following assumptions are employed for the sake of simplicity: (1) all materials work linearly elastically; (2) all interfaces are well bonded; (3) only stresses that are parallel to the optical fiber are considered; (4) the impact of the optical fiber's presence on the host matrix's strain field is neglected.

Figure 2.2 illustrates an arbitrary infinitesimal segment of an optical fiber with a dual-layer coating embedded in host matrix, which is usually cement- or epoxy-based material. Due to symmetry, only a half structure is shown. The shear stresses in the inner

and outer coatings are represented by $\tau_i(x, r)$ and $\tau_o(x, r)$, respectively. The shear stress between the host matrix and the outer coating is represented by $\tau_o(x, r_o)$. The shear stress between the outer and inner coatings is represented by $\tau_i(x, r_i)$. The shear stress at the interface between the inner coating and the fiber core is represented by $\tau_f(x)$. The normal stresses in the fiber core, the outer coating, the inner coating, and the vicinity of host matrix are represented by $\sigma_f(x)$, $\sigma_o(x)$, $\sigma_i(x)$, and $\sigma_h(x)$, respectively. The deformations of the optical fiber, inner coating, outer coating, and the host matrix are represented by δ_f, δ_o, δ_i, and δ_h, respectively, at x with a segment of dx length. The shear strains in the inner and outer coatings are represented by γ_i and γ_o, respectively. For each segment, no deformation is shown on the left side. The deformations in Figure 2.2 represent the total deformation of both sides.

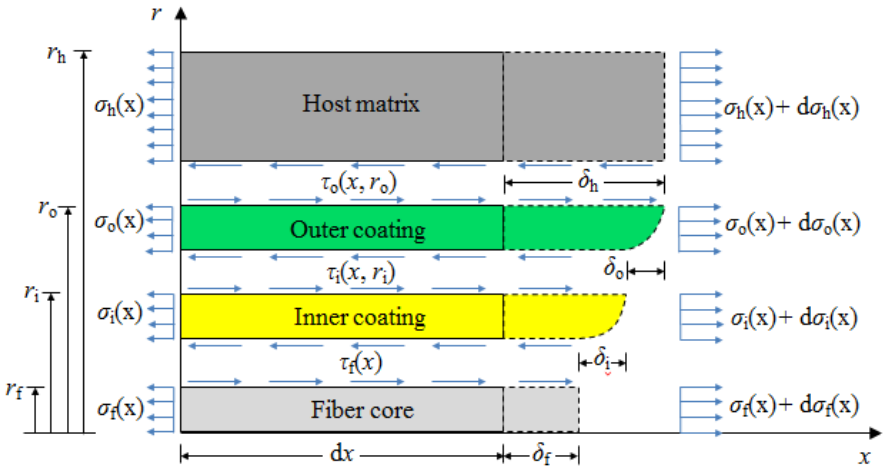

Figure 2.2. Stress analysis for optical fiber embedded in concrete

Equations of equilibrium in the x-direction are:

$$(\pi r_f^2)\,\mathrm{d}\sigma_f(x) + (2\pi r_f)\tau_f(x)\,\mathrm{d}x = 0 \tag{2.1}$$

$$(\pi r^2 - \pi r_f^2)\,\mathrm{d}\sigma_i(x) + (2\pi r_f)\tau_i(x,r)\,\mathrm{d}x = (2\pi r_f)\tau_f(x)\,\mathrm{d}x,\ r_f \le r \le r_i \tag{2.2}$$

$$(\pi r^2 - \pi r_i^2)\,\mathrm{d}\sigma_o(x) + (2\pi r)\tau_o(x,r)\,\mathrm{d}x = (2\pi r_i)\tau_i(x,r_i)\,\mathrm{d}x,\ r_i \le r \le r_o \tag{2.3}$$

Considering no force is directly applied on the coatings at $x = 0$, integrating from 0 to x equations (2.2) and (2.3) can be rewritten as:

$$(\frac{r^2 - r_f^2}{2x})\sigma_i(x) + r\tau_i(x,r) = r_f\tau_f(x),\ r_f \le r \le r_i \tag{2.4}$$

$$(\frac{r^2 - r_f^2}{2x})\sigma_o(x) + r\tau_o(x,r) = r_i\tau_i(x,r_i),\ r_i \le r \le r_o \tag{2.5}$$

Since the diameter of the optical fiber is small compared with its length, the first terms in equations (2.4) and (2.5) vanish, except for the vicinity at the two ends of the optical fiber (Ansari 1998). Then, equations (2.4) and (2.5) can be rewritten as:

$$r\tau_i(x,r) = r_f\tau_f(x),\ r_f \le r \le r_i \tag{2.6}$$

$$r\tau_o(x,r) = r_i\tau_i(x,r_i) = r_f\tau_f(x),\ r_i \le r \le r_o \tag{2.7}$$

According to the 1st assumption, the optical fiber's longitudinal strain can be expressed as:

$$\sigma_f(x) = E_f\varepsilon_f(x) \tag{2.8}$$

Thus, equation (2.1) can be rewritten as:

$$\tau_f(x) = -\frac{E_f r_f}{2}\frac{d\varepsilon_f(x)}{dx} \tag{2.9}$$

Plug equation (2.9) into equations (2.6) and (2.7), respectively:

$$\tau_i(x,r) = -\frac{E_f r_f^2}{2r}\frac{d\varepsilon_f(x)}{dx},\ r_f \le r \le r_i \tag{2.10}$$

$$\tau_o(x,r) = -\frac{E_f r_f^2}{2r}\frac{d\varepsilon_f(x)}{dx},\ r_i \le r \le r_o \tag{2.11}$$

According to the 2nd assumption, the deformations in Figure 2.2 satisfy:

$$\delta_h = \delta_f + \delta_i + \delta_o \tag{2.12}$$

The longitudinal deformations of the host matrix and the glass fiber can be expressed as:

$$\delta_h = \varepsilon_h(x)dx,\ \delta_f = \varepsilon_f(x)dx \tag{2.13}$$

The strain transfer from the host matrix to the optical fiber core depends on the shear strain in the interlayer which is due to the relative deformation between the host matrix and fiber core. Therefore, for the inner and outer coatings:

$$\delta_{\mathrm{i}} = \int_{r_{\mathrm{f}}}^{r_{\mathrm{i}}} \mathrm{d}\gamma_{\mathrm{i}}(x,r)\,\mathrm{d}r = \frac{1}{G_{\mathrm{i}}}\int_{r_{\mathrm{f}}}^{r_{\mathrm{i}}} \mathrm{d}\tau_{\mathrm{i}}(x,r)\,\mathrm{d}r \tag{2.14}$$

$$\delta_{\mathrm{o}} = \int_{r_{i}}^{r_{o}} \mathrm{d}\gamma_{\mathrm{o}}(x,r)\,\mathrm{d}r = \frac{1}{G_{\mathrm{o}}}\int_{r_{i}}^{r_{o}} \mathrm{d}\tau_{\mathrm{o}}(x,r)\,\mathrm{d}r \tag{2.15}$$

where, $\gamma_{\mathrm{i}} = \tau_{\mathrm{i}} / G_{\mathrm{i}}$, and $\gamma_{\mathrm{o}} = \tau_{\mathrm{o}} / G_{\mathrm{o}}$.

Plug equations (2.13) to (2.15) into equation (2.12):

$$\varepsilon_{\mathrm{h}}(x)dx = \varepsilon_{\mathrm{f}}(x)\,\mathrm{d}x + \frac{1}{G_{\mathrm{i}}}\int_{r_{\mathrm{f}}}^{r_{\mathrm{i}}} \mathrm{d}\tau_{\mathrm{i}}(x,r)\,\mathrm{d}r + \frac{1}{G_{\mathrm{o}}}\int_{r_{i}}^{r_{\mathrm{o}}} \mathrm{d}\tau_{\mathrm{o}}(x,r)\,\mathrm{d}r \tag{2.16}$$

By substituting equations (2.10) and (2.11) into equation (2.16), and rearranging the nonzero term *dx*, equation (2.16) can be rewritten as:

$$\varepsilon_{\mathrm{h}}(x) = \varepsilon_{\mathrm{f}}(x) - \frac{\mathrm{E_f r_f^2}}{2}\left[\frac{In(r_{\mathrm{i}} / r_{\mathrm{f}})}{G_{\mathrm{i}}} + \frac{In(r_{\mathrm{o}} / r_{\mathrm{i}})}{G_{\mathrm{o}}}\right]\frac{d^2\varepsilon_{\mathrm{f}}(x)}{dx^2} \tag{2.17}$$

By introducing a positive coefficient *k*, equation (2.17) can be rewritten as:

$$\varepsilon_f''(x) - \mathrm{k}^2\varepsilon_f(x) + \mathrm{k}^2\varepsilon_h(x) = 0\,,\quad \mathrm{k}^2 = \frac{2}{\mathrm{E_f r_f^2}\left[\frac{\mathrm{In}(r_{\mathrm{i}} / r_{\mathrm{f}})}{G_{\mathrm{i}}} + \frac{\mathrm{In}(r_{\mathrm{o}} / r_{\mathrm{i}})}{G_{\mathrm{o}}}\right]} \tag{2.18}$$

where *k* can be determined 55 m^{-1} for the optical fiber packaged with a dual-layer coating, according to the optical fiber's dimensions and material properties.

The strain transfer in optical fibers with multi-layer coatings can be analyzed following the same process. As a matter of fact, equation (2.18) can be extended to a generalized form for optical fibers with multi-layer coatings, as long as k^2 is modified as:

$$\mathrm{k}^2 = \frac{2}{\mathrm{E_f r_f^2}\left[\frac{\mathrm{In}(r_1 / r_{\mathrm{f}})}{G_1} + \frac{\mathrm{In}(r_2 / r_1)}{G_2} + \cdots + \frac{\mathrm{In}(r_n / r_{n-1})}{G_n}\right]}$$

where *n* represents the number of coating layers.

2.3.2. Solutions of Governing Equation. The characteristic equation of equation (2.18) is $\lambda^2 - \mathrm{k}^2 = 0$, which always has two real solutions $\pm k$. Thus, the solution of the nonhomogeneous equation (2.18) can be expressed as (Boyce 2001):

$$\varepsilon_{\mathrm{f}}(x) = C_1 \cosh(\mathrm{k}x) + C_2 \sinh(\mathrm{k}x) + \varepsilon^{\mathrm{p}}(x) \tag{2.19}$$

where the first two terms represent the general solution, and the 3rd term, $\varepsilon^{\mathrm{p}}(x)$, is the particular solution associated with $\varepsilon_{\mathrm{h}}(x)$ that denotes the strain distribution in the host matrix along the optical fiber. The integration constants, C_1 and C_2, are determined by the boundary conditions.

In general, the form of $\varepsilon_{\mathrm{h}}(x)$ can be different in various problems. Thus, the particular solution $\varepsilon^{\mathrm{p}}(x)$ can be different, correspondingly. For an arbitrary condition, $\varepsilon_{\mathrm{h}}(x)$ can be expressed using a Fourier series. However, for a large amount of engineering problems, $\varepsilon_{\mathrm{h}}(x)$ can be segmentally expressed as or approximated by a series of polynomials, as shown in equation (2.20).

$$\varepsilon_{\mathrm{h}}(x) = \sum_{i=0}^{m} a_i x^i \tag{2.20}$$

where m represents the order, and a_i (i=0, 1, 2, … , m) represent the coefficients.

Correspondingly, $\varepsilon^{\mathrm{p}}(x)$ can be determined as a polynomial of the same order within each segment where is $\varepsilon_{\mathrm{h}}(x)$ continuous and differentiable regarding to x (Boyce 2001). Therefore, $\varepsilon^{\mathrm{p}}(x)$ and $\varepsilon_{\mathrm{f}}(x)$ can be written as:

$$\varepsilon^{p}(x) = \sum_{i=0}^{m} b_i x^i \ , \ \varepsilon_{\mathrm{f}}(x) = \mathrm{C}_1 \cosh(\mathrm{k}x) + \mathrm{C}_2 \sinh(\mathrm{k}x) + \sum_{i=0}^{m} b_i x^i \tag{2.21}$$

where b_i (i=0, 1, 2, … , m) represent the coefficients. The relationship between a_i and b_i are as follows.

When m < 2,

$$a_i = b_i \tag{2.22}$$

When m ≥ 2,

$$a_i = \begin{cases} b_i & i = m-1, m \\ b_i - (i+2)(i+1)b_{i+2} / \mathrm{k}^2 & i \le m-2 \end{cases} \tag{2.23}$$

The strain transfer ratio is defined:

$$\alpha(x) = \varepsilon_f(x) / \varepsilon_h(x) \tag{2.24}$$

2.4. STRAIN TRANSFER EFFECTS IN DIFFERENT STRAIN FIELDS

Different cases of strain field are investigated in this section.

2.4.1. Uniform Strain Field. As the simplest case, strain transfer effect in uniform strain field of host matrix is first investigated.

2.4.1.1 Strain transfer in uniform strain field. An optical fiber is embedded along the central axis of a cylinder which is of uniform cross section, as illustrated in Figure 2.3. The cylinder is subjected to a pair of uniaxial forces that are directly applied on the host matrix. The fiber is in a uniform strain field. The axial force, elastic modulus, and cross-sectional area are represented by P, E_h, and A_h, respectively.

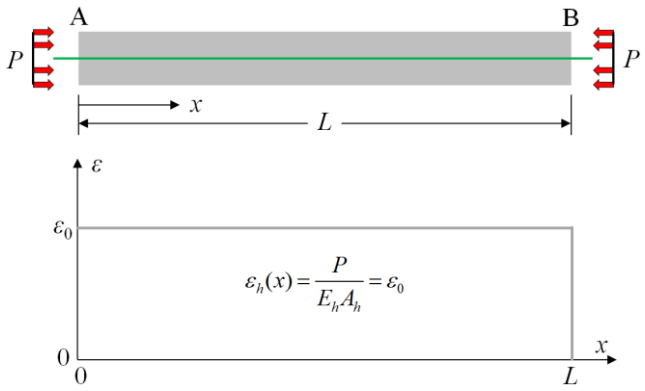

Figure 2.3. Uniaxial tensile test in uniform strain field

The normal strain in the host matrix can be determined: $\varepsilon_h(x) = P/E_hA_h = \varepsilon_0$. Thus, the normal strain in the optical fiber can be determined from equation (2.21), as given in equation (2.25).

$$\varepsilon_f(x) = C_1 \cosh(kx) + C_2 \sinh(kx) + \varepsilon_0 \tag{2.25}$$

Then, the shear stress applied on the optical fiber can be determined from equation (2.10), as given in equation (2.26):

$$\tau_f(x) = -0.5 E_f r_f [kC_1 \sinh(kx) + kC_2 \cosh(kx)] \tag{2.26}$$

The boundary conditions are:

$$\varepsilon_f(x=0)=0,\ \tau_f(x=\mathrm{L}/2)=0 \tag{2.27}$$

By substituting equation (2.27) into equations (2.25) and (2.26), respectively, the coefficients C_1 and C_2 can be determined:

$$C_1=-\varepsilon_0,\ C_0=\varepsilon_0\tanh(\mathrm{kL}/2)$$

Therefore, the normal strain and shear stress are:

$$\varepsilon_f(x)=\varepsilon_0[1-\cosh(\mathrm{k}x)+\tanh(\mathrm{kL}/2)\sinh(\mathrm{k}x)] \tag{2.28}$$

$$\tau_f(x)=-0.5\mathrm{E_f r_f k}\varepsilon_0[\tanh(\mathrm{kL}/2)\cosh(\mathrm{k}x)-\sinh(\mathrm{k}x)] \tag{2.29}$$

The strain transfer ratio is:

$$\alpha(x)=1-\cosh(\mathrm{k}x)+\tanh(\mathrm{kL}/2)\sinh(\mathrm{k}x) \tag{2.30}$$

The strain transfer ratio can be plotted against x ($0 \le x \le$ L/2 for the left half), as shown in Figure 2.4(a). The right half (L/2 < $x \le$ L) is symmetrical to the left half. At each end of the optical fiber, there is a development length where the measured strain is smaller than the real strain due to the strain transfer effect.

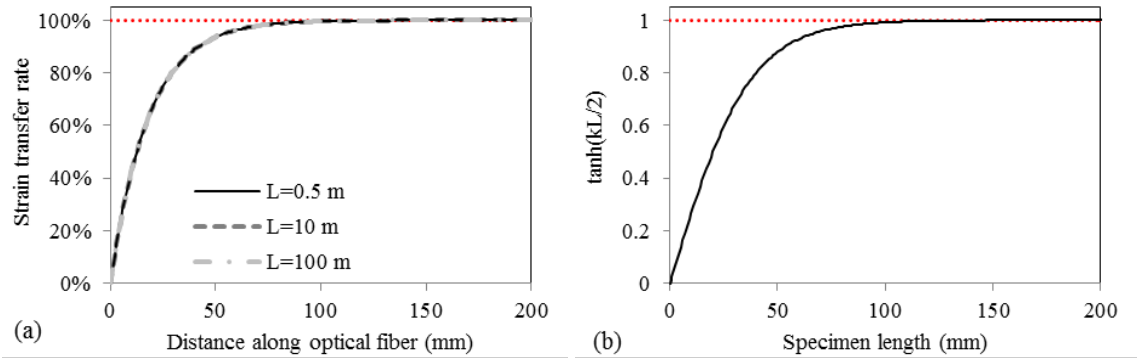

Figure 2.4. Strain transfer ratio in uniform strain field: (a) strain transfer ratio vs. distance; (b) tanh(kL/2) vs. the specimen length

The strain is gradually developed within that length, and the strain transfer ratio will be approximately 1.0 beyond that length. The development length is dependent on k that is related to the material and geometry of the optical fiber and independent of the

applied strain ε_0. For the optical fiber with a dual-layer coating in this study, 95% of the strain could be developed in 55 mm, and 99% of strain could be developed in 84 mm. Equation (30) can be used to correct the measured strains within the development length. With k = 55 m^{-1}, tanh(kL/2) increases to 0.95 at L = 66 mm, in Figure 2.4(b). When the specimen length is longer than 100 mm, the effect of specimen length is negligible.

2.4.1.2 Interaction between optical fiber and host matrix. The presence of optical fiber influences the strain field of the host matrix, which is related to the elastic modulus of the host matrix (Jiang *et al.* 1998; Li *et al.* 2009). The effects of the interaction, which are not considered in the above studies, are discussed in this section.

A finite element model was established to investigate the influence of different host matrixes on the strain transfer effect using ABAQUS®. The host matrix and the optical fiber packaged with polymer coating were modeled using three-dimensional eight-node brick elements with reduced integration (C3D8R). Perfect bonding was assumed for all the interfaces, which was defined using a keyword "Tie". A uniform strain field was considered. A quarter of the cylinder was modeled due to the symmetry, as shown in Figure 2.5. The end and middle section were represented by A and B, respectively. The longitudinal (Z direction) and the lateral (X direction) translations were constrained, respectively, at the longitudinal and vertical (B) cut faces. A uniform compressive deformation of 0.24 mm, which was equivalent to 0.48 mm for a full-length cylinder, was applied on the end surface (A) along the longitudinal direction. For the sake of computational efficiency, the diameter of the cylinder was taken 2 mm, which was not a realistic dimension but did not influence the results significantly.

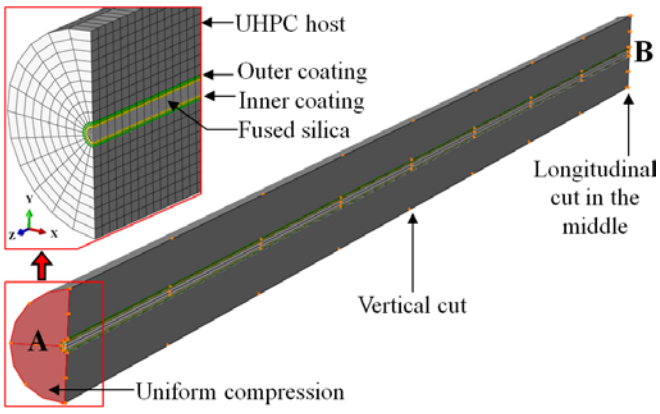

Figure 2.5. Finite element model

Figure 2.6(a) and (b) show the representative simulation results of the normal strain contours within the optical fiber core and host matrix, respectively. Along the longitudinal direction, the compressive strain within the optical fiber increases from the end (A) to the middle (B) sections. However, the compressive strain within the host matrix decreases from A to B.

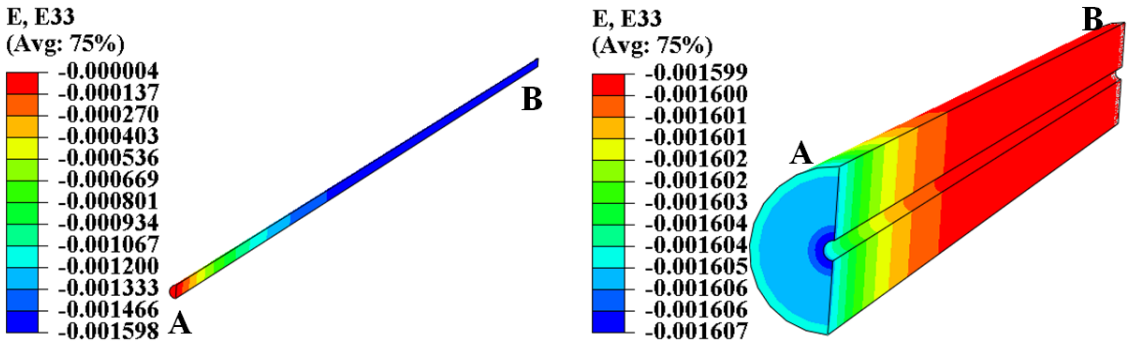

(a) Optical fiber core (b) Host matrix

Figure 2.6. Representative simulation results

The effect of different elastic moduli on the strain transfer behaviors was investigated to account for different host matrixes. The investigated elastic modulus range was 1 GPa to 80 GPa that covered the elastic modulus range of most adhesives. The elastic modulus of epoxy or concrete is typically about 5 GPa to 50 GPa.

The normal strains within the fiber core and host matrix can be respectively plotted against the distance in the longitudinal direction, as shown in Figures 2.7(a) and (b). The change of elastic modulus did not significantly influence the strain distribution in the fiber. However, it highly influenced the strain field of the host matrix, particularly in the vicinity of the end. This was mainly because the load that was carried by the optical fiber was gradually increased from the end to the middle, due to the strain transfer effect.

The compressive strains within the optical fiber and host matrix at the middle section (B) were respectively plotted against the elastic modulus of host matrix, as shown in Figure 2.8. The strain increased with the elastic modulus of host matrix. However, the increase was only 3% as the elastic modulus was increased from 1 GPa to 80 GPa. Therefore, the effect of different elastic moduli on the strain transfer is insignificant for the distributed fiber optic sensor packaged with polymer coating.

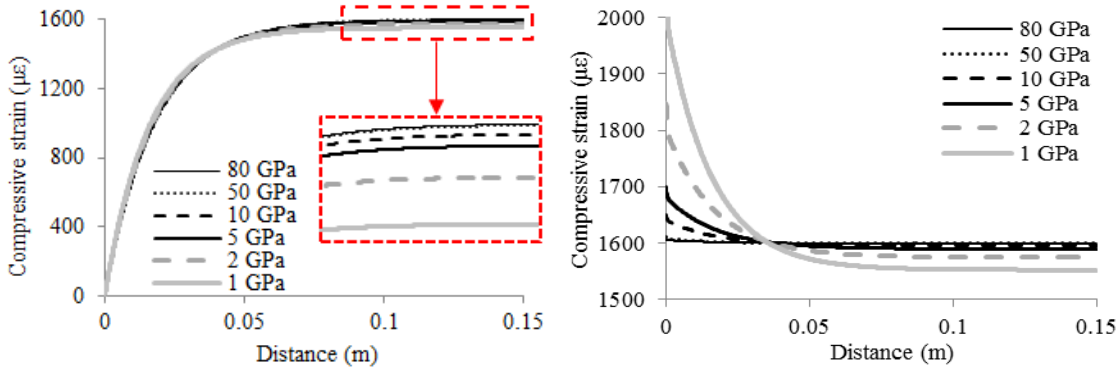

(a) Optical fiber core (b) Host matrix

Figure 2.7. Longitudinal normal strain distributions

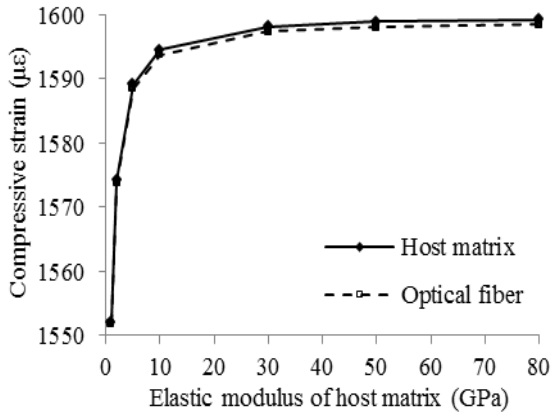

Figure 2.8. Influence of elastic modulus of host matrix on strain transfer

2.4.2. Non-Uniform Strain Fields. Three non-uniform strain fields were investigated, which included discontinuous strain field, continuous strain field with a non-differentiable point, and continuous strain field without any non-differentiable point. Since Equation (27) is based on the assumption that the strain field of the host is continuous and differentiable, when discontinuity or non-differentiable point appears, the structure needs to be cut into segments for analysis.

2.4.2.1 Discontinuous field. A discontinuity section can result from an abrupt material, geometry, or load change. Figure 2.9 illustrates a cylinder subjected to a pair of uniaxial forces (*P*) applied at the cross sections C and D. An optical fiber is deployed at the center of the cylinder. The strain field is discontinuous at C and D, due to the applied load. The cylinder can be divided into three segments: A-C, C-D, and D-B. Among them, A-C and D-B are symmetrical to each other. No external force is applied on the concrete,

but the optical fiber is subjected to a uniaxial force P_f at the cut face. C-D is subjected to both P and P_f. The strain corresponding to P_f is determined: $\varepsilon = P_f / EA$. For the segment A-C ($-a \le x \le 0$), the normal strain in the host material is zero. Thus, equations (2.25) and (2.26) can be rewritten as:

$$\varepsilon_f(x) = C_1 \cosh(kx) + C_2 \sinh(kx) \tag{2.31}$$

$$\tau_f(x) = -0.5 E_f r_f [k C_1 \sinh(kx) + k C_2 \cosh(kx)] \tag{2.32}$$

The boundary conditions are:

$$\varepsilon_f(x=0) = \varepsilon\,,\ \varepsilon_f(x=-a) = 0 \tag{2.33}$$

By substituting equation (2.33) into equations (2.31) and (2.32), respectively, the coefficients C_1 and C_2 can be determined:

$$C_1 = \varepsilon\,,\ C_2 = \varepsilon / \tanh(ka)$$

Then, the normal strain and shear stress distributions are determined:

$$\varepsilon_f(x) = \varepsilon[\cosh(kx) + \sinh(kx)/\tanh(ka)] \tag{2.34}$$

$$\tau_f(x) = -0.5 E_f r_f k\varepsilon[\sinh(kx) + \cosh(kx)/\tanh(ka)] \tag{2.35}$$

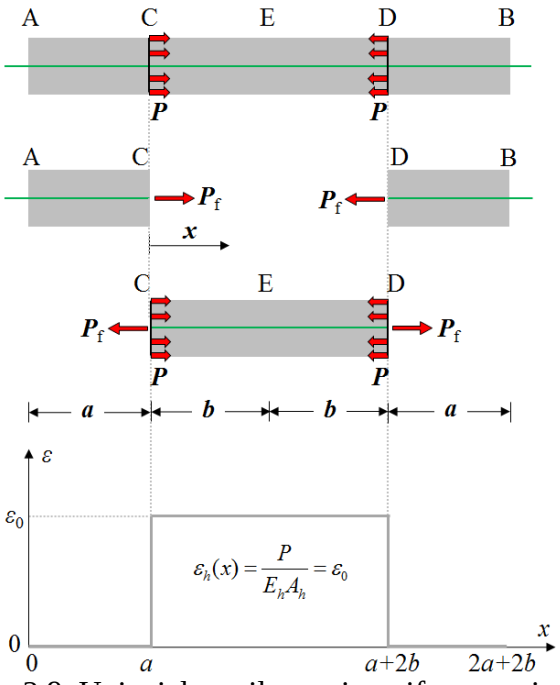

Figure 2.9. Uniaxial tensile test in uniform strain field

For the segment C-D ($0 < x \le b$), the total stresses and strains can be calculated by superposing two loading scenarios respectively corresponding to P and P_f. The normal strain and shear stress corresponding to *P* have been determined in equations (2.28) and (2.29). By replacing *L*/2 with *b*, they can be rewritten as:

$$\varepsilon_{f1}(x) = \varepsilon_0[1 - \cosh(kx) + \tanh(kb)\sinh(kx)] \tag{2.36}$$

$$\tau_{f1}(x) = -0.5E_f r_f k\varepsilon_0[\tanh(kb)\cosh(kx) - \sinh(kx)] \tag{2.37}$$

The normal strain and shear stress corresponding to P_f have been given in equations (2.34) and (2.35). Replacing (-*a*) by *b*, they can be rewritten as:

$$\varepsilon_{f2}(x) = \varepsilon[\cosh(kx) - \tanh(kb)\sinh(kx)] \tag{2.38}$$

$$\tau_{f2}(x) = -0.5E_f r_f k\varepsilon[\sinh(kx) - \tanh(kb)\cosh(kx)] \tag{2.39}$$

The shear stresses at section C are the same in A-C and C-D. Therefore,

$$\tau_{f,AC}(x=0) = \tau_{f,CD}(x=0),\ \tau_{f,CD}(x=0) = \tau_{f1}(x=0) + \tau_{f2}(x=0) \tag{2.40}$$

By substituting equations (3.35), (3.37), and (3.39) into equation (2.40),

$$\varepsilon = \varepsilon_0\left(\frac{\eta}{1+\eta}\right) \tag{2.41}$$

where $\eta = \tanh(ka)\cdot\tanh(kb)$. Then, the normal strain in A-E ($-a < x \le b$) is determined:

$$\varepsilon_f(x) = \begin{cases} \varepsilon_0\left(\frac{\eta}{1+\eta}\right)[\cosh(kx) + \tanh(ka)\sinh(kx)] & -a \le x \le 0 \\ \varepsilon_0 - \varepsilon_0\left(\frac{1}{1+\eta}\right)[\cosh(kx) - \tanh(kb)\sinh(kx)] & 0 < x \le b \end{cases} \tag{2.42}$$

As shown in Figure 2.4, $\tanh(kx)$ approaches to 1.0 as *x* increases, and reaches 0.95 at $x = 33$ mm. When either *b* is close to *a*, or both of them are larger than 33 mm, η will be approximately 1.0, and thus, ε will be approximately $0.5\varepsilon_0$. By setting ε_0 at 1.0 (normalized), the normal strain in the fiber can be plotted, as shown in Figure 2.10, according to equation (2.42). There is a development length at each side of the loading section, and the development length is insensitive to the specimen length as long as the specimen length is sufficiently large for the strain development. The development lengths

are found to be the same as that in uniform strain field, which are 55 mm for 95% and 84 mm for 99% of strain at each side. The strain at the load point (C and D) is 50% of the fully-developed strain.

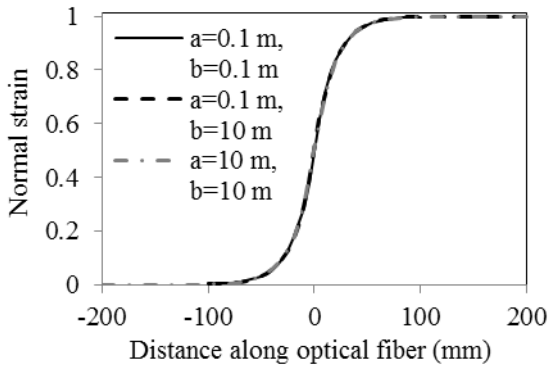

Figure 2.10. Strain transfer ratio in uniform strain fields

2.4.2.2 Continuous field with a non-differentiable point. Figure 2.11 depicts a beam that has a uniform cross section and is instrumented near the bottom with an optical fiber. The beam is simply supported at its two ends, which are respectively marked by A and B. The beam is subjected to a concentrated load, P, at C. The lengths of A-C and B-C are denoted by *a* and *b*, respectively. The span length is *L*. At the loading section, the strain field is continuous and non-differentiable.

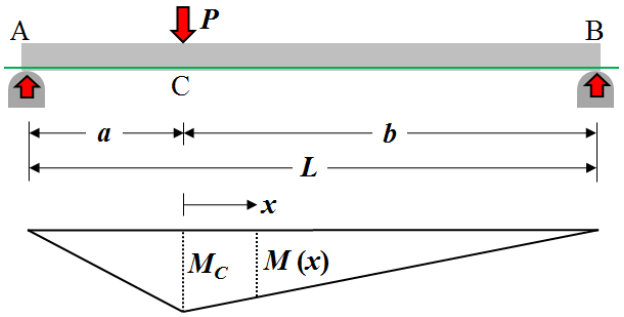

Figure 2.11. Simply-supported beam subjected to a concentrated load at an arbitrary section

The bending moment can be determined by:

$$M(x)=\begin{cases}\mathrm{P}b(a+x)/\mathrm{L} & -a\le x\le 0\\ \mathrm{P}a(b-x)/\mathrm{L} & 0<x\le b\end{cases}, \tag{2.43}$$

Then, the normal strain in the beam can be determined:

$$\varepsilon_{\mathrm{h}}(x)=\frac{M(\mathrm{x})\mathrm{y}}{\mathrm{EI}}=\begin{cases}\varepsilon_{\mathrm{c}}(1+x/a) & -a\le x\le 0\\ \varepsilon_{\mathrm{c}}(1-x/b) & 0<x\le b\end{cases}, \tag{2.44}$$

where the normal strain at the section C is denoted as ε_{c}, and ε_{c} = Paby/LEI.

Therefore, the normal strain and shear stress of the optical fiber are:

$$\varepsilon_{\mathrm{f}}(x)=\begin{cases}C_1\cosh(\mathrm{k}x)+C_2\sinh(\mathrm{k}x)+\varepsilon_{\mathrm{c}}(1+x/a) & -a\le x\le 0\\ C_3\cosh(\mathrm{k}x)+C_4\sinh(\mathrm{k}x)+\varepsilon_{\mathrm{c}}(1-x/b) & 0<x\le b\end{cases}, \tag{2.45}$$

$$\tau_{\mathrm{f}}(x)=\begin{cases}-0.5\mathrm{E}_{\mathrm{f}}\mathrm{r}_{\mathrm{f}}[\mathrm{k}C_1\sinh(\mathrm{k}x)+\mathrm{k}C_2\cosh(\mathrm{k}x)+\varepsilon_{\mathrm{c}}/a] & -a\le x\le 0\\ -0.5\mathrm{E}_{\mathrm{f}}\mathrm{r}_{\mathrm{f}}[\mathrm{k}C_3\sinh(\mathrm{k}x)+\mathrm{k}C_4\cosh(\mathrm{k}x)-\varepsilon_{\mathrm{c}}/b] & 0<x\le b\end{cases}, \tag{2.46}$$

where C_1, C_2, C_3, and C_4 represent the integration constants, which can be determined by the boundary conditions.

The boundary conditions are:

$$\varepsilon_{\mathrm{f}}(x=-a)=\varepsilon_{\mathrm{f}}(x=b)=0,\ \varepsilon_{\mathrm{f}}(x\to 0^{-})=\varepsilon_{\mathrm{f}}(x\to 0^{+}),\tau_{\mathrm{f}}(x\to 0^{-})=\tau_{\mathrm{f}}(x\to 0^{+})$$

where $\varepsilon_{\mathrm{f}}(x\to 0^{-})$ and $\varepsilon_{\mathrm{f}}(x\to 0^{+})$ represent the normal strains at section C in segments A-C and C-B, respectively. The shear stresses at section C in segments A-C and C-B are respectively represented by $\tau_{\mathrm{f}}(x\to 0^{-})$, and $\tau_{\mathrm{f}}(x\to 0^{+})$.

The integration constants can be determined:

$$C_1=-\frac{\eta}{\xi}\frac{\varepsilon_{\mathrm{c}}\mathrm{L}}{\mathrm{k}ab},\ C_2=-\frac{\tanh(kb)}{\xi}\frac{\varepsilon_{\mathrm{c}}\mathrm{L}}{\mathrm{k}ab},\ C_3=-\frac{\eta}{\xi}\frac{\varepsilon_{c}\mathrm{L}}{\mathrm{k}ab},\ C_4=\frac{\tanh(ka)}{\xi}\frac{\varepsilon_{\mathrm{c}}\mathrm{L}}{\mathrm{k}ab}$$

where ξ = tanh(ka)+tanh(kb).

The strain transfer ratio can be determined:

$$\alpha(x)=\begin{cases}1-\dfrac{\eta\mathrm{L}}{\xi\mathrm{k}ab(1+x/a)}[\cosh(\mathrm{k}x)+\dfrac{\sinh(\mathrm{k}x)}{\tanh(\mathrm{k}a)}] & -a<x\le 0\\ 1-\dfrac{\eta\mathrm{L}}{\xi\mathrm{k}ab(1-x/b)}[\cosh(\mathrm{k}x)-\dfrac{\sinh(\mathrm{k}x)}{\tanh(\mathrm{k}b)}] & 0<x<b\end{cases}, \tag{2.47}$$

At the loading section (x = 0), the strain transfer ratio is:

$$\alpha(x) = 1 - \frac{\eta \mathrm{L}}{\xi \mathrm{k} a b} \tag{2.48}$$

The strain transfer ratio at the loading section can be plotted against a, as shown in Figure 2.12(a). It increases as the loading section approaches to the mid-span and achieves the maximum value at the mid-span. It increases with the beam's span length. Figure 2.12(b) shows the loading position where 95% of the strain can be developed, denoted by a_{95}, which depends on the span length and approximates to 185 mm.

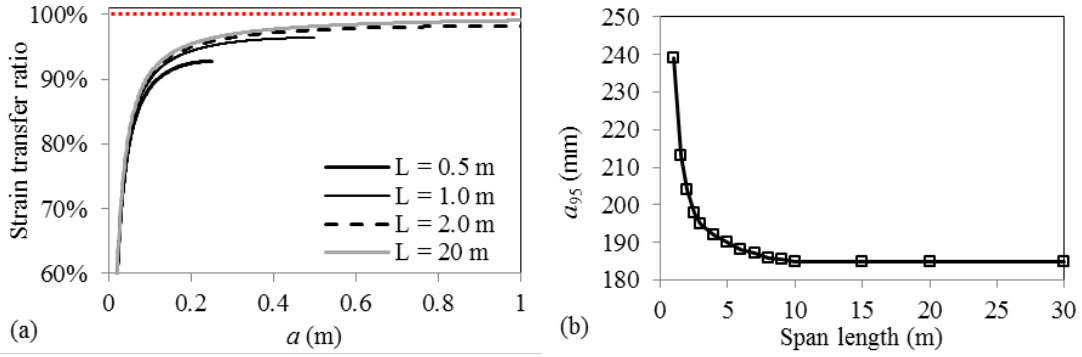

Figure 2.12. Strain transfer ratio in the simple beam loaded at an arbitrary location: (a) strain transfer ratio vs. loading location; (b) a_{95} vs. span length

Particularly, when the concentrated load is applied at the mid-span, $a = b = \mathrm{L}/2$. Equation (2.47) can be rewritten as:

$$\alpha(x) = 1 - \frac{\tanh(\mathrm{kL}/2)\cosh(\mathrm{kx}) - \sinh(\mathrm{k}|\mathrm{x}|)}{\mathrm{k}(\mathrm{L}/2 - |\mathrm{x}|)}, \quad -\mathrm{L}/2 < x < \mathrm{L}/2 \tag{2.49}$$

The strain transfer ratio can be plotted against x, where $0 < x \leq \mathrm{L}/2$ for the left half, as shown in Figures 2.13(a). The right half ($\mathrm{L}/2 < x < \mathrm{L}$) is symmetrical to the left half. At the two ends of the optical fiber, there is no development length and the strain transfer ratio is 1.0. However, the strain transfer is less than 1.0 at the loading section.

The normal strain is developed within a length in the vicinity of the loading section. The length is dependent on k, which is related to the material and geometry of the optical fiber, and independent of the applied strain ε_0. It is also dependent on the beam length. For a beam that has a 0.25-m clear span length, 95% of the strain can be

developed within 24 mm from the mid-span, and 99% of the strain can be developed within 61 mm. The mid-span strain transfer ratio for a 2-m beam is 98%, and 99% of the strain can be developed in 12 mm. Figure 2.13(b) shows the mid-span strain transfer ratio that increases with the span length. When the span length is 0.73 m, the strain transfer ratio achieves 95%. When the span length is 3.86 m, the strain transfer ratio reaches 99%.

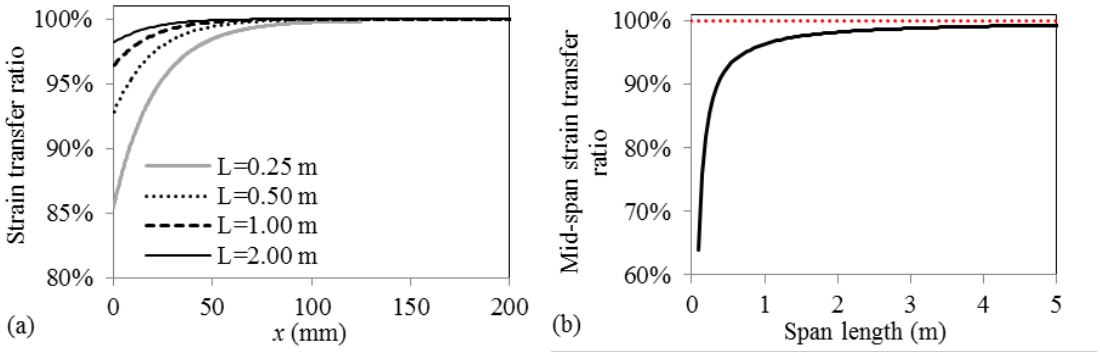

Figure 2.13. Strain transfer ratio in the simple beam loaded at the mid-span: (a) strain transfer ratio vs. location; (b) mid-span strain transfer ratio vs. span length

2.4.2.3 Continuous field without any non-differentiable point. Figure 2.14 illustrates a concrete beam instrumented with an optical fiber near the bottom. The beam has a uniform cross section, and is subjected to a uniform distributed load over the span.

The bending moment in the beam is $M(x) = 0.5\ w\ (Lx\text{-}x^2)$. The normal strain in the concrete at the height where the optical fiber is deployed is denoted as $\varepsilon_h(x)$, and can be determined using $\varepsilon_h(x) = M(x)\cdot y / EI = 0.5\ w\ y\ (Lx - x^2) / EI$.

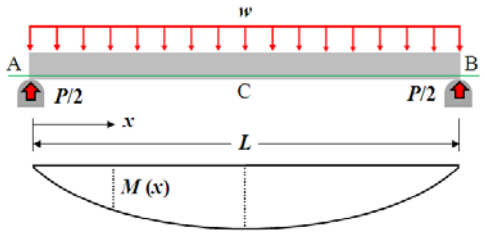

Figure 2.14. Simply-supported beam subjected to uniformly-distributed loads

Thus, equations (3.22) and (3.23) can be rewritten as:

$$\varepsilon_f(x) = C_1 \cosh(kx) + C_2 \sinh(kx) + 0.5wy(Lx - x^2) / EI \qquad (2.50)$$

$$\tau_f(x) = -0.5E_f r_f[kC_1 \sinh(kx) + kC_2 \cosh(kx) + 0.5wy(L - 2x)/EI] \quad (2.51)$$

The boundary conditions are:

$$\varepsilon_f(x = 0) = 0,\ \tau_f(x = L/2) = 0 \quad (2.52)$$

By substituting equations (3.50) and (3.51) into equation (2.52), the coefficients C_1 and C_2 can be determined:

$$C_1 = C_2 = 0$$

Therefore, the normal strain and shear stress distributions are:

$$\varepsilon_f(x) = 0.5wy(Lx - x^2)/EI \quad (2.53)$$

$$\tau_f(x) = -0.25E_f r_f wy(L - 2x)/EI \quad (2.54)$$

The strain transfer ratio is:

$$\alpha(x) = 1$$

The strain transfer ratio is constant at 1.0, meaning there is no strain transfer issue for a simply-supported beam under uniformly-distributed load.

2.5. VALIDATION OF THE MECHANICAL MODEL

A uniaxial compressive test was carried out to validate the uniform strain field model. An ultra-high performance concrete (UHPC) cylinder was instrumented with a distributed fiber optic sensor and tested using a load frame (capacity: 250 kN) under displacement control. The strain distributions along the optical fiber was measured with PPP-BOTDA using a Neubrescope (model: NBX-7020) at room temperature.

The UHPC cylinder, which was 50mm in diameter and 300 mm in height, was instrumented with a distributed fiber optic sensor at the center. The two ends of the fiber were connected to the Neubrescope to form a loop, as depicted in Figure 2.15. A 2-kN preload was applied to allow the load frame and cylinder to set. Then, the displacement was reset, and the cylinder started to be loaded. The compressive deformation was sequentially increased to 0.48 mm with a step size of 0.12 mm, which corresponded to 1,600 με with a step size of 400 με.

The UHPC has a water-to-cementitous materials ratio (w/cm) of 0.2. The volume fractions of ground granulated blast-furnace slag and silica fume were respectively 50% and 5% of the binder. A Type III portland cement with Blaine fineness of 560 m^2/kg was employed. The Blaine fineness of the GGBS was 590 m^2/kg. Masonry sand (0 mm to 2 mm) and river sand (0 mm to 4.75 mm) were used, and their specific gravities are 2.63 and 2.64, respectively. A high-ranged water reducing admixture was used, which made the mixture appear self-consolidated (Meng and Khayat 2016). Steel fibers that were 0.2 mm in diameter and 13 mm in length were used with a volume fraction of 2%. The fiber has a tensile strength and modulus of elasticity of 1.9 GPa and 203 GPa, respectively. All test samples were cured for 24 hours in mold covered with wet burlap and plastic sheet and kept at room temperature (23 °C). After demolding, the samples were cured in lime-saturated water at room temperature until testing. The 28-d compressive strength was measured to be 125 MPa using 50-mm cubes. The elastic modulus and Poisson's ratio were measured to be 50 GPa and 0.18, respectively, in accordance with ASTM C469.

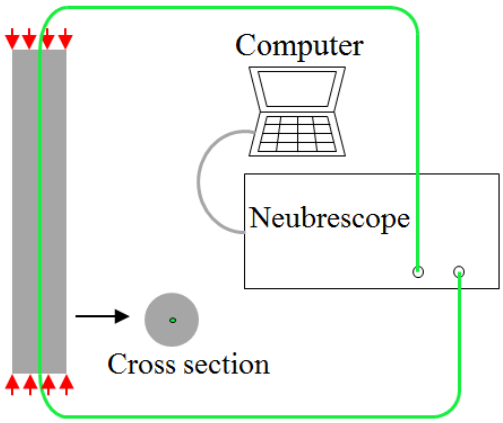

Figure 2.15. Experimental setup of the uniaxial compressive tests

The measured, analytical, and simulated strain distributions are respectively represented by "Exp", "Ana", and "Sim", and compared in Figure 2.16. Since a half-length cylinder was modeled, the simulation results only include the strain distribution over a half of the cylinder length. Overall, the experimental results were in good agreement with the analytical and the simulation results, and thus, validated the finite element model and the derived formulae of strain transfer for the uniform strain fields.

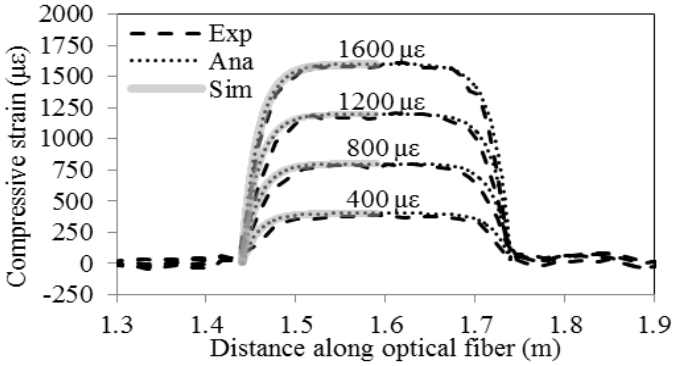

Figure 2.16. Strain distributions in the cylinder under uniaxial compression

2.6. SUMMARY

Based on the above investigations, the main findings are summarized below:

The analytical formulae of strain transfer can be used to interpret the strain distributions measured from the distributed fiber optic sensors packaged with polymer coating. The inaccurate strain measurements, due to the strain transfer effect, can be corrected using the derived formulae. In a uniform strain field, inaccurate strain measurements exist at the two ends of the host matrix. An 84-mm length is required to develop 95% of the normal strain for a distributed fiber optic sensor with a dual-layer coating. An abrupt strain change in a host matrix can lead to inaccurate strain measurements. Under uniaxial step loads, an 84-mm length at each side of the loading section is required to develop 95% of the normal strain. For beam members under three-point bending, the length of the inaccurate measurement decreases with the beam's span length. The strain transfer effect does not lead to inaccurate strain measurements in simply-supported beams under uniformly-distributed lateral loads.

The strain transfer effect is dependent on the elastic modulus of the host matrix. However, for the commonly-used adhesives, whose elastic moduli are typically within the range of 5 GPa to 50 GPa, the change of elastic modulus does not significantly influence the strain transfer behavior. Increasing the host's elastic modulus from 1 GPa to 80 GPa increases about 3% of the normal strain in the optical fiber.

3. EARLY-AGE BEHAVIORS OF ULTRA-HIGH-PERFORMANCE CONCRETE OVERLAY

3.1. BACKGROUND

Ultra-high-performance concrete (UHPC) is an advanced fiber-reinforced cementitious composite, typically prepared with a very low (< 0.25) water-to-binder ratio. Due to its superior mechanical properties and durability (Meng et al. 2017; Russell and Graybeal 2013; Meng and Khayat 2016a; Shen et al. 2008), UHPC has been used in construction of thin overlays (Meng et al. 2017), stay-in-place formworks (Meng and Khayat 2016a), and functionally-graded composites (Shen et al. 2008; Meng and Khayat 2016b). However, early-age shrinkage of UHPC may compromise the performance of UHPC structural elements (Bao et al. 2015). In a bonded concrete overlay system, when the overlay is placed on top of the substrate, the shrinkage of substrate is already stable. Therefore, the substrate may restrain the development of the shrinkage of overlay, resulting in internal stress and even discontinuity at the interface, which in turn accelerate deterioration and reduce service life of the structure (Bao et al. 2017).

The ability to identify discontinuity in structures can enable timely and cost-effective repair or retrofit, thus extending the service life of the structure. Linear variable differential transformers were used to detect localized delamination of a concrete overlay cast on top of a concrete slab (Shin and Lange 2012). On the other hand, a variety of nondestructive testing techniques were proposed and implemented to detect discontinuity in concrete structures, such as magnetic waves (Jammalamadaka et al. 2008), ultrasonic wave (Blackshire and Sathish 2002), acoustic wave (Semperlotti and Conlon 2010), and thermography (Wang et al. 2006). However, to detect cracks inside of concrete is still a challenge because of the highly-heterogeneous properties of concrete. The presence of steel fibers in UHPC makes the detection more challenging. More importantly, it is very hard to quantify the initiation and propagation of interfacial delamination by using the nondestructive testing approaches.

At the same time, various fiber optic sensors have been proposed and attracted increasing research interest due to their unique characteristics, such as immunity to electromagnetic interference, compactness, resistance to harsh environment, and multiplexing capability. In the literature, FBG sensors have been used to detect

discontinuity in composite structures (Lu et al. 2015; Farmand-Ashtiani et al. 2013; Takeda et al. 2012). When an embedded FBG strain sensor happens to cross any discontinuity in its host matrix, at the discontinuity location, the sensor will be subjected to a suddenly-increased deformation, thus detecting the discontinuity as an abrupt increase of strain. However, due to the difficulty in predicting the positions of discontinuity at the time of fiber installation, FBG sensors can unlikely capture discontinuity in practice. For this reason, FBG sensors were multiplexed to form a quasi-distributed sensor network to increase likelihood of detecting discontinuity at multiple locations (Farmand-Ashtiani et al. 2013). However, it would be costly to manufacture and deploy such multiplexed sensors, and the spatial resolution and operation distance of this technology could be limited to satisfy civil engineering applications.

In this sense, distributed sensors may be good alternatives. An electric coaxial cable sensor was used to detect cracks in full-scale reinforced concrete girders (Chen et al. 2012). However, the electric sensor was not immune to electromagnetic interference, so the measurement results may be affected and inaccurate. On the other hand, distributed fiber optic sensors based on light scatterings have been proposed to monitor multiple cracks in concrete structures. The measurement distance of Rayleigh scattering based technologies were found limited to tens of meters (Leung et al. 2005; Jiang et al. 2009; Bao and Chen 2012). For long distance applications, sensing technologies based on Brillouin scattering have been developed. However, the spatial resolutions of conventional BOTDA or BOTDR are limited to a half meter, which is too coarse to provide satisfactory results in detecting discontinuity. In the meanwhile, PPP-BOTDA technology has been developed to detect cracks in concrete pavement overlays and delamination in carbon fiber reinforced polymer composites with embedded capillary sensors and comparative vacuum monitoring techniques (Minakuchi et al. 2012; Sierra-Pérez et al. 2016).

This section reports the investigation on the feasibility of measuring early-age shrinkage of UHPC and detecting delamination in a bonded interface of thin UHPC overlay and thick concrete substrate using the PPP-BOTDA distributed fiber optic sensor. Three composite specimens instrumented with two types of single-mode optical fibers were prepared and tested. A three-dimensional finite element model of individual overlay

and substrate elements is developed with tested material properties and validated with distributed fiber optic sensor data, in order to understand the delamination process of the entire specimen. The overlay-substrate interface was modeled using cohesive elements.

3.2. MEASURING EARLY-AGE SHRINKAGE STRAIN

This section reports an experimental investigation on measurement of early-age shrinkage strain of UHPC using distributed fiber optic sensors embedded in a UHPC cylinder specimen.

3.2.1. Experimental Program. A mortar cylinder specimen was prepared and tested at a controlled room temperature (22 °C ± 1 °C) in accordance with ASTM C1698. The specimen was cast in a polyethylene (transparent) corrugated tube measuring 380 mm in length. The groove and ridge diameters of the tube were 20 mm and 25 mm, respectively, as shown in Figure 3.1. Since the plastic tube was not removed, the mortar was considered sealed and used to evaluate the autogenous shrinkage. The specimen was cured in air with a relative humidity of about 60 % ± 3 % at room temperature. The initial and final setting times were measured to be 75 min and 300 min, respectively, in accordance with ASTM C191. The mortar tested in this study corresponds to an UHPC mixture, which typically has high autogenous shrinkage. The water-to-binder ratio of the mortar was set at 0.2, by mass, and the binder-to-sand ratio was set at 1.0, by mass. The binder was composed of 40% Type III Portland cement and 60% Class C fly ash, by volume. A high-range water reducer was used to improve the workability of the mortar at a dosage of 1.2% of binder, by mass.

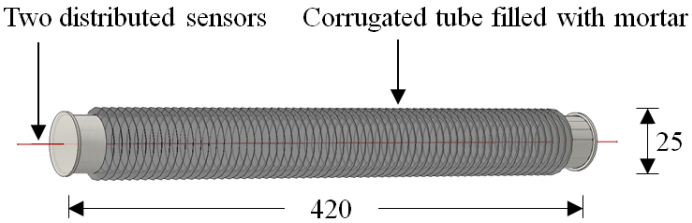

Figure 3.1. Illustration of the sealed specimen (unit: mm)

The cylinder was instrumented with two closely-deployed optical fibers, which served as distributed sensors. The two fibers were about1 mm inside of the specimen’s

surface at grooves. One of the sensors was directly in contact with the mortar to measure the combined effect of temperature and strain. The other sensor was placed inside a thin steel tube measuring 450 mm in length for temperature compensation. The inner and outer diameters of the steel tube were 0.5 mm and 1.0 mm, respectively. The two sensors in each specimen were connected to form a loop, so that they were measured in one measurement and both temperature and strain along the distributed sensors could be evaluated. Note the minimum diameter of the end loop of the distributed sensor was no less than 40 mm so that the light loss due to macro-bending effect was negligible.

The two optical fiber sensors were placed inside a protective aluminum tube measuring 450 mm in length, 3 mm in inner diameter, and 4 mm in outer diameter, as illustrated in Figure 3.2(a). Prior to mortar casting, the aluminum tube was passed through a 5-mm-diameter hole drilled on each end of the corrugated mold, and removed after mortar placement for approximately 5 minutes, leaving the distributed fiber optic sensor in direct contact with fresh mortar that was still flowable to encapsulate the sensor. Figure 3.2(b) shows the distributed fiber optic sensor embedded in mortar. No air pocket was observed near the sensor's surface.

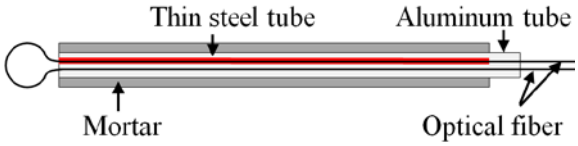

(a) Instrumentation with two distributed fiber optic sensors

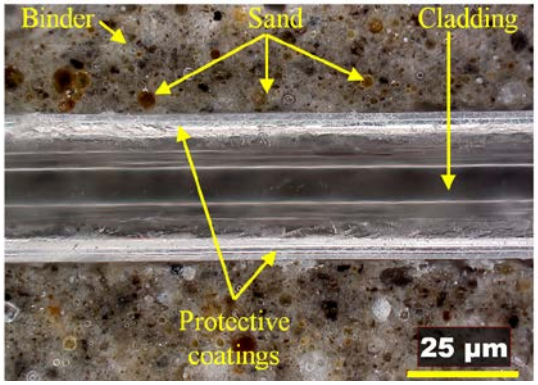

(b) Longitudinal section after testing with adequate encapsulation of sensor

Figure 3.2. Preparation of the specimen

3.2.2. Experimental Results and Discussion. The Brillouin scattering frequency along the length of each fiber optic sensor was measured using the Neubrescope at various curing times, up to 14 days. The Brillouin frequency shift due to temperature effect was measured for temperature compensation, and then the Brillouin frequency shift due to strain change was evaluated by subtracting the frequency shift due to strain change from the combined effect of strain and temperature. The ASTM standard test for shrinkage measurement was conducted for comparison with the distributed sensor data.

The strain distribution along the embedded fiber optic sensor at 1 day, 3 days, 7 days, and 14 days of curing are plotted in Figure 3.3(a). The horizontal axis represents the distance along the distributed fiber optic sensor measured from its connection to the Neubrescope. The portion of optical fiber in direct contact with mortar is specified in Figure 3.3(a). The strain measured along the specimen length was negative and not uniform, indicating non-uniform compressive strain due to shrinkage. Shrinkage strain (positive) is referred to the absolute value of measured strain (negative). Shrinkage strain at 2.87 m to 2.99 m along fiber length are consistently larger than those at 3.03 m to 3.23 m; the minimum value occurred at 2.99 m to 3.03 m, as marked between the two vertical lines in Figure 3.3(a), where a shrinkage induced crack was observed at the surface of the specimen. Each strain peak corresponds to crack location. The release of shrinkage strain near the crack was small and slightly increased over time.

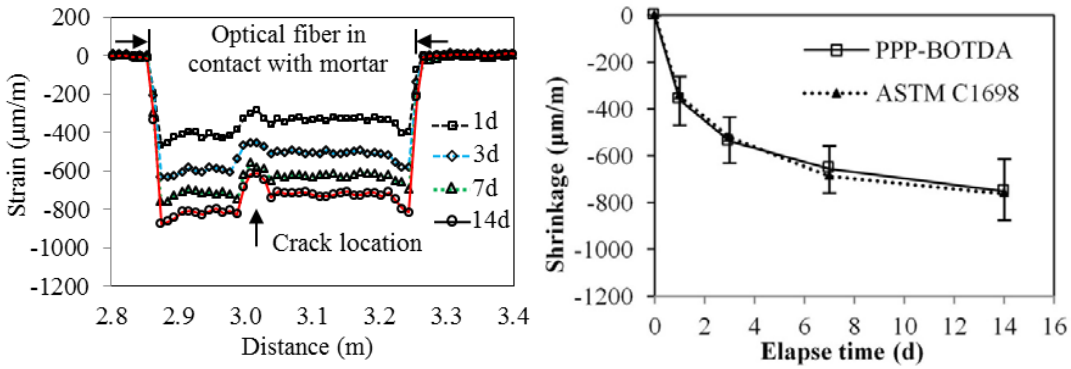

(a) Strain distributions (b) Comparison with ASTM method

Figure 3.3. Shrinkage strain results

Figure 3.3(b) shows that the average value of each strain distribution is in reasonable agreement with the strain results measured by ASTM C1698. Each of the

error bars in Figure 3.3(b) represents the maximum and the minimum strain values at different curing ages. The strain due to early age shrinkage increased rapidly at the beginning of curing and then became stabilized after about 7 days.

3.3. EARLY-AGE DELAMINATION IN BONDED OVERLAY

This section reports an experimental investigation on detection of delamination in a bonded interface of thin UHPC overlay and thick concrete substrate due to early-age shrinkage strain of UHPC using embedded distributed fiber optic sensors.

3.3.1. Materials. In this study, the substrate was fabricated with conventional concrete (CC), and the overlay was cast with UHPC. Table 3.1 lists the mixture compositions. The CC was prepared with a water-to-cement ratio of 0.4, and its coarse limestone aggregates had a maximum size of 21 mm. The UHPC had a water-to-binder ratio of 0.2. The binder was composed of cement and granulated blast slag. A high-range water reducer was added during the mixing of UHPC to enhance its flowability. The dosage of the high-range water reducer was adjusted to reach a slump flow of 280 mm ± 10 mm in accordance with ASTM C230/C230M. Micro steel fibers measuring 13 mm in length and 0.2 mm in diameter were used to increase the tensile properties of the UHPC.

Table 3.1. Mixture compositions

Materials	UHPC	CC
Cement (kg/m^3)	593	243
Ground granulated blast slag (kg/m^3)	546	–
River sand (0–5 mm) (kg/m^3)	704	792
Masonry sand (0–2 mm) (kg/m^3)	298	–
Coarse aggregate (kg/m^3)	–	1046
High-range water reducer (l/m^3)	54	0.8
Water (kg/m^3)	174	218
Steel fibers (kg/m^3)	156	–

3.3.2. Material Properties. The compressive properties and tensile properties of the CC were respectively evaluated in accordance with ASTM C39 and ASTM C496. In each test, five cylinders were prepared and tested. At 56 days, the average compressive and splitting tensile strengths were 50.5 MPa and 3.6 MPa, respectively. The average elastic modulus and Poisson's ratio were 40.5 GPa and 0.20, respectively.

Three UHPC prisms were prepared for evaluation of shrinkage in accordance with ASTM C596. The final setting moment was determined as 17 hours in accordance with ASTM C403/C403M, and taken as the time zero for shrinkage measurement. The shrinkage strain is plotted as a function of the elapsed time after the final setting, as shown in Figure 3.4(a). The average strain increased from 325 με at 1 day to 810 με at 21 days, and then became stabilized afterwards. The compressive strength and splitting tensile strength were respectively evaluated in accordance with ASTM C109/C109M and ASTM C307. The average compressive strength increased from 64 MPa at 1 day to 124 MPa at 28 days, as shown in Figure 3.4(b). The average tensile strength increased from 3.1 MPa at 1 day to 11.0 MPa at 28 days. The elastic modulus and Poisson's ratio were determined to be 51 GPa and 0.18, respectively, in accordance with ACI 318-14. The density of the UHPC was 2,650 kg/m^3 at 28 days.

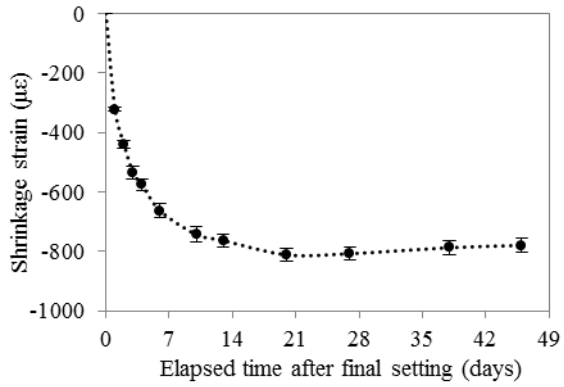

(a) Total shrinkage

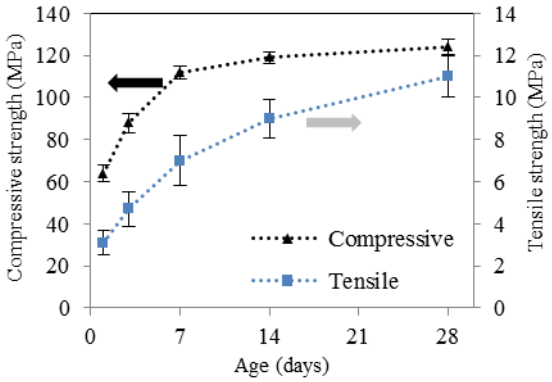

(b) Compressive and tensile strengths

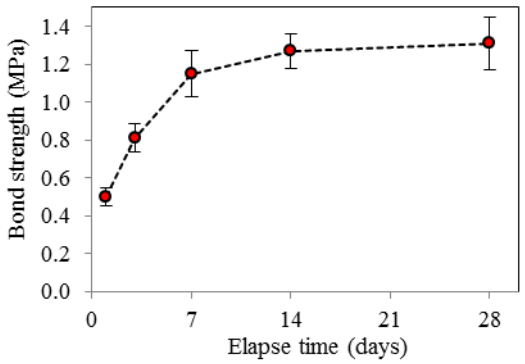

(c) Bond strength

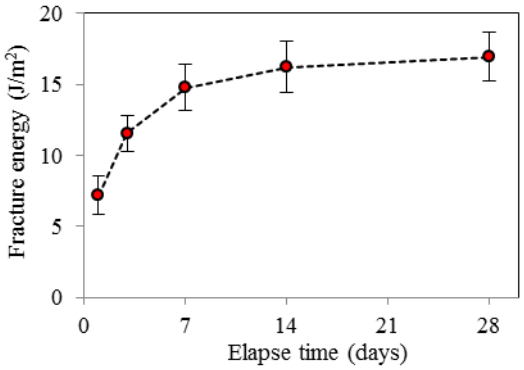

(d) Fracture energy

Figure 3.4. Material properties of UHPC (provided by Weina Meng and Mahdi Valipour)

Three CC prisms were prepared as the substrate and cured for 60 days. A thin UHPC layer measuring 25 mm in thickness was then cast on top of the CC substrates. During the curing process, hydrates such as calcium hydroxide (CH) and calcium silicate hydrate (C-S-H) formed and bonded the substrate and overlay. Pull-off tests were performed by Mr. Mahdi Valipour to evaluate the bond strength and fracture energy of the UHPC-CC interface at 1 day, 3 days, 7 days, 14 days, and 28 days (Al-Attar 2013; Seoa and Choi 2014; Chan and Li 1997). The fracture energy was defined as the work done by the pull-off force until fracture. The average bond strength increased from 0.5 MPa at 1 day to 1.3 MPa at 28 days. The average fracture energy increased from 7.2 MPa at 1 day to 17 MPa at 28 days.

The microstructures of the UHPC, CC, and their interface were examined using scanning electron microscopy (SEM). Figure 3.5(a)–(d) show the SEM images of an overall structure, the zoom-in interface, the UHPC overlay, and the CC substrate, respectively. An interfacial transition zone measuring about 10 μm to 30 μm in thickness formed with less hydration products (Li et al. 1995; Bentz 2000), higher porosity, and lower mechanical strength and elastic modulus than the UHPC overlay and the CC substrate (Akçaoğlu et al. 2005; Wang et al. 2009). Compared with the UHPC, the CC contains more voids due to the higher water content, as can be seen in Table 3.1.

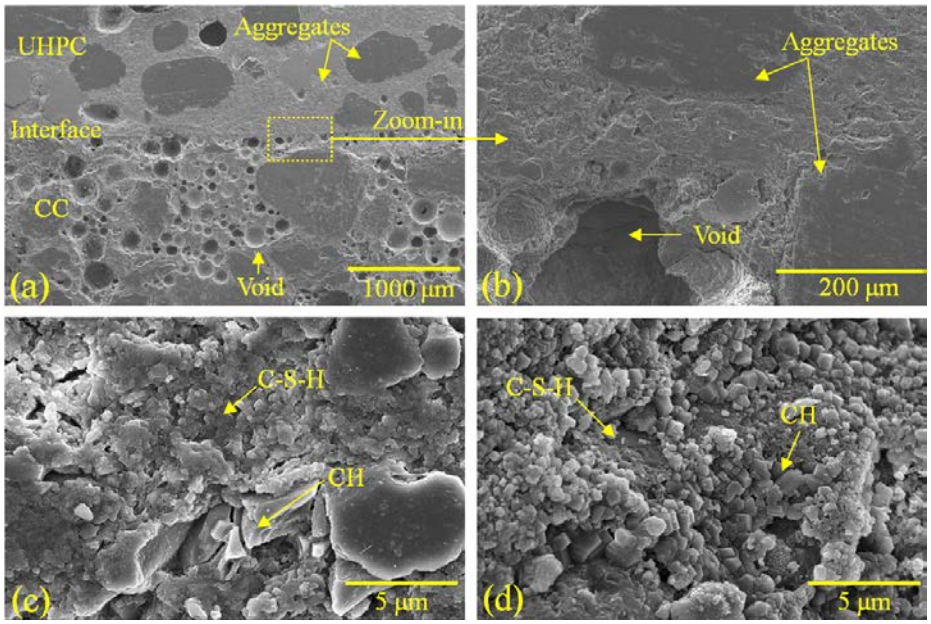

Figure 3.5. SEM images: (a) overall structure; (b) zoom-in interface; (c) UHPC; (d) CC

3.3.3. Preparation and Instrumentation of Specimens. Three concrete overlay specimens were prepared. As illustrated in Figure 3.6, each specimen was composed of a 200-mm-thick substrate and a 25-mm-thick overlay. After casting, the CC substrate concrete was covered with a wet burlap and plastic sheet for 7 days and then cured in air at room temperature and a relative humidity of 50 % ± 2 % until 60 days when the shrinkage deformation became stabilized. The UHPC overlay was then cast on top of the CC substrate, cured under a wet burlap and plastic sheet for 24 hours, and then air-cured under the same condition as the substrate. Immediately after the formwork was removed, three 1-mm-thick layers of low-viscosity epoxy were applied on the two side faces along the longer side of the specimen to prevent exchange of water with the ambient environment, since there is little moisture transport between adjacent concrete in practice.

Each specimen was instrumented with three distributed fiber optic sensors: one 2C sensor and one 3C sensor, both in direct contact with the concrete for strain and temperature measurements, and one 2C sensor isolated by a thin polymer hose measuring 0.5 mm in inner diameter and 0.7 mm in outer diameter for temperature compensation. The three distributed fiber optic sensors were closely installed in a pattern as illustrated in Figure 3.6. The fibers were continuously passed back and forth through the overlay-substrate interface for 16 times, forming 16 intersection points at the interface zone: P1 to P16. The two ends of each sensor were connected to the Neubrescope, and the Brillouin frequency shifts were measured along the length of the distributed fiber optic sensors at 1 day, 3 days, 7 days, 14 days, 21 days, and 28 days after final setting of the UHPC.

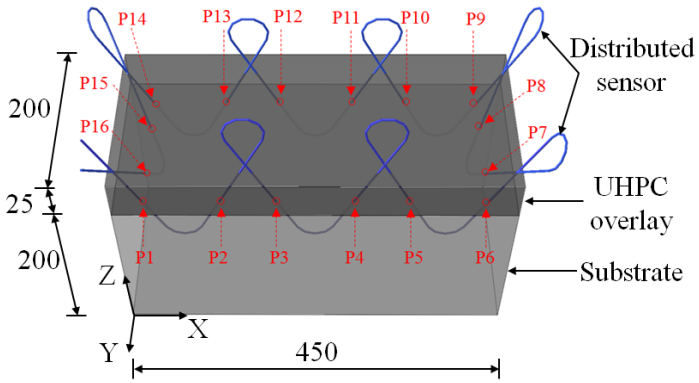

Figure 3.6. Illustration of test specimen (unit: mm)

3.3.4. Strain Distribution and Delamination Detection. With the calibrated strain sensitivity coefficients, the Brillouin frequency distributions measured from the distributed sensors were converted into strain distributions. The strain distributions respectively measured from the 2C and 3C sensors in one of the specimens are shown in Figures 3.7(a) and (b). The horizontal and vertical axes respectively represent the distance along the fibers and the measured strain values. Each of the two figures contains four curves respectively measured at 1 day, 3 days, 7 days, 14 days, 21 days, and 28 days after final setting of the UHPC. In each of the curves, multiple peaks are observed, which indicate delamination at the overlay-substrate interface.

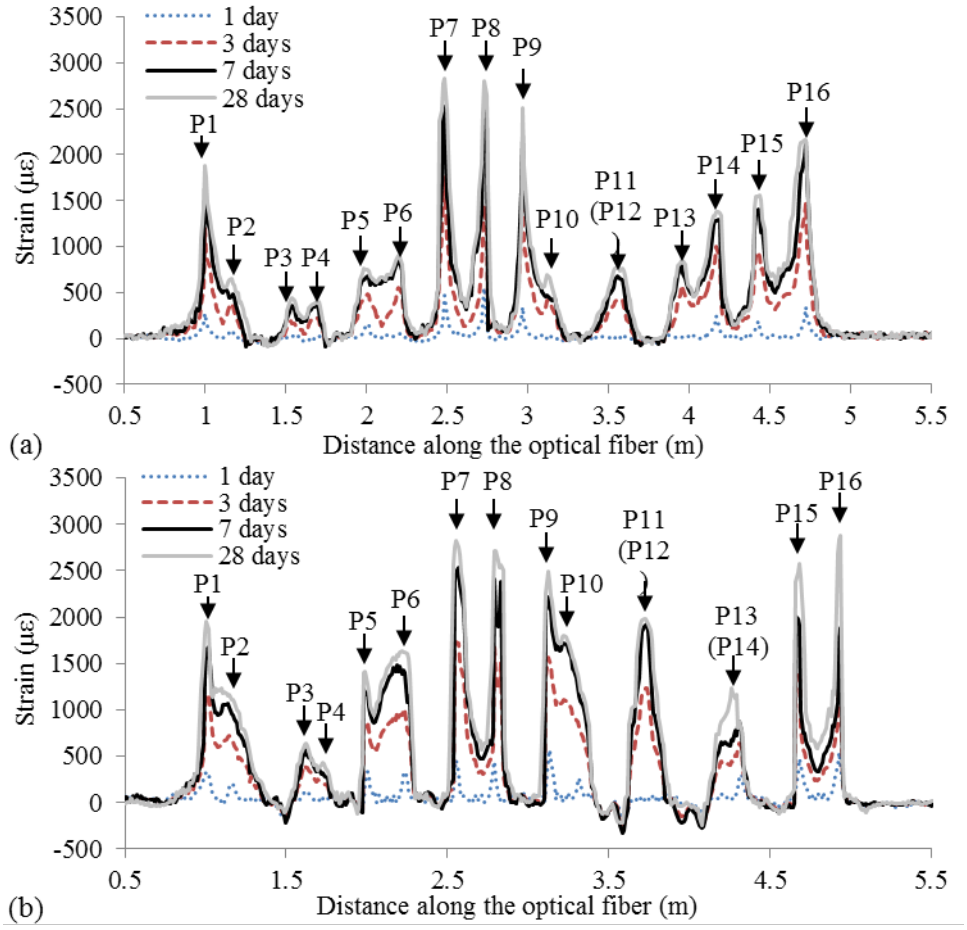

Figure 3.7. Strain distributions: (a) 2C sensor; (b) 3C sensor

As illustrated in Figure 3.8, the delamination at the overlay-substrate interface involves both separation and dislocation between the overlay and the substrate, which can

be schematically represented by a combined opening-sliding movement. Points “A” and “B”, initially located at the same point, are displaced after delamination. The embedded optical fibers, which were perfectly bonded to the substrate and the overlay, were locally elongated in the vicinity of the overlay-substrate interface, resulting in sudden increases of strain as identified as sharp peaks in the strain distributions in Figure 3.7 (Feng et al. 2013). The peak strains increased with the opening width and sliding distance at the delamination surface, and their relationships could be represented by a bilinear equation (Bao et al. 2016). Therefore, once the peak strains were determined, the corresponding delamination could be quantified.

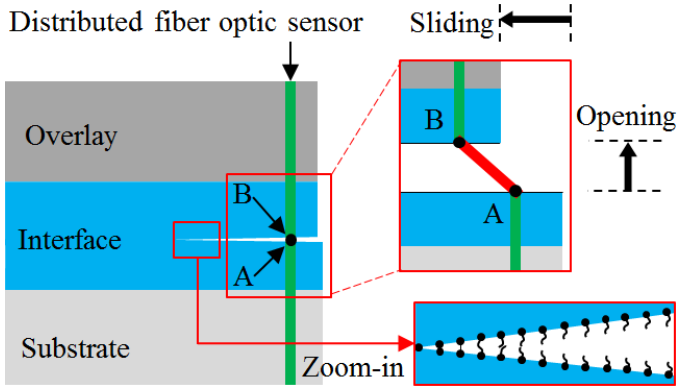

Figure 3.8. Combined opening-sliding movement

The peaks of strain distributions as shown in Figure 3.7 represent the locations of delamination in the specimen, specifically at the intersection points (P1 to P16). Both visible and hidden cracks can be detected when they are intersected by the optical fibers. However, when two intersection points are close to each other, their corresponding peaks in the strain distribution can be too close to distinguish particularly at increasing strains/delamination. For example, the peaks corresponding to P11 and P12 in Figure 3.7(a) cannot be separated due to large delamination while the peaks corresponding to P4 and P3 can due to relatively small delamination. The contrast between the two areas symmetric to the centerline of the specimen along the long side indicates that the delamination pattern is asymmetric for the symmetric specimen. The onset and propagation of delamination can also be monitored from the strain distribution. As indicated in Figure 3.7(a), no delamination at P6 is detected within the 1st day but

delamination is detected within the 3rd day. Therefore, the actual delamination at P6 happened between the 1st and 3rd days. Furthermore, the increase of each peak's magnitude depicts the growth of delamination. Overall, the measurements from two sensors are in good agreement. The small discrepancy is likely due to slightly different installation locations.

The (average ± one standard deviation) peak strains of the three specimens are plotted at various intersection points in Figure 3.9. The peak strains and variations at all points increased over time from 1 day to 28 days. The peak strains near the short-side edges of the specimens were larger than those near the center since the short-side edges were subject to larger delamination due to symmetry of the specimens. The peak strains can be converted into delamination sliding distances based on the relation between the peak strain and sliding distance established previously (Bao et al. 2016). The 28-day average results from the three specimens are plotted at various locations of the intersection points along the overlay-substrate interface in Figure 3.10. The color bar represents the delamination distance in micron.

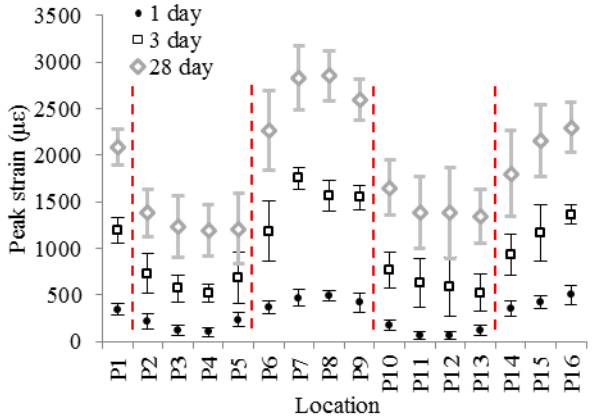

Figure 3.9. Peak strain vs. location

After the completion of all measurements, the tested specimen corresponding to Figure 3.10 was submerged into a standard liquid dye diluted with water at a 1:1 volume ratio. The overlay was then removed for visual inspection as shown in Figure 3.11. The dark areas indicate the ingress of dye and thus represent the delaminated areas at the overlay-substrate interface. The light areas represent intact interface without

delamination. Therefore, delamination at the interface occurs towards the two ends of the specimen and it is not symmetric about the centerline of the specimen along the long side, as indicated by the strain measurements in Figure 3.7. The distribution of delamination is in general agreement with the strain measurements (Figure 3.10).

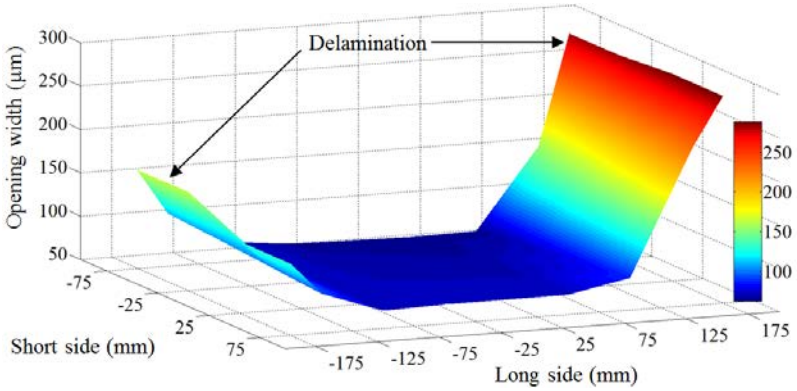

Figure 3.10. Visualization of interfacial delamination

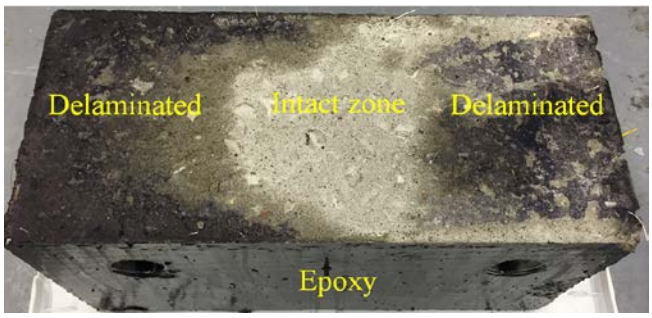

Figure 3.11. Photo of the overlay-substrate interface after the dye test (photo provided by Mahdi Valipour)

3.4. SIMULATIONS OF DELAMINATION IN BONDED OVERLAY

Finite element analysis is conducted in this section to understand the delamination behaviors of the structure.

3.4.1. Finite Element Model. A three-dimensional (3D) nonlinear finite element model was developed in ABAQUS to understand the complete delamination process of the overlay-substrate composite system. Due to symmetry, a quarter of the system was modeled as illustrated in Figure 3.12. In the cut planes “X” and “Z”, the movements along X and Z axes were restrained, respectively. A surface-to-surface hard contact between the substrate and the fixed floor was considered using a penalty friction model.

The overlay and the substrate of the composite system were modeled in a continuum mechanics approach using linear 3D brick reduced integration elements (C3D8R). Each C3D8R element has eight nodes, each having three degrees of freedom. The overlay-substrate interface was modelled in a traction-separation approach using a 25-μm-thick layer of eight-node 3D cohesive elements (COH3D8). A convergence study of mesh sizes was performed to set 5 mm and 50 μm mesh sizes for C3D8R and COH3D8 elements, respectively. The measured material properties, such as strengths, fracture parameters, and shrinkage parameters, were used in the finite element model.

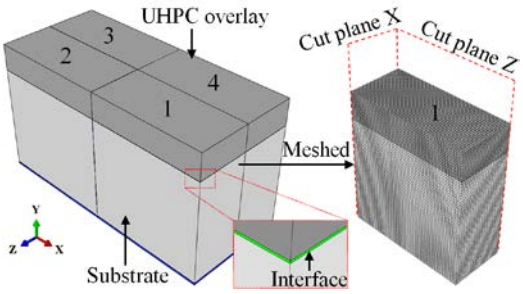

Figure 3.12. Finite element model

3.4.2. Material Models. A cohesive zone model can be defined by the critical limiting stress, the critical energy release rate (G_c), and the shape of a traction-separation law as depicted in Figure 3.13. The traction linearly increases with the induced separation till its maximum and linearly decreases after damage is initiated. The slope of the ascending line represents the stiffness associated with the elastic modulus and thickness of the interfacial transition zone. When the actual physical thickness of the interfacial transition zone is unknown, a penalty-based approach can be applied (Diehl 2008). A small separation value can be selected to make the traction-separation law become an impulse-like shape. The descending curve can be defined by a linear softening law. The entire area underneath the curve represents the critical energy release rate, which determines the damage evolution. In this study, the damage evolution was defined by fracture energy as shown in Figure 3.4(d), and the mode mix was defined using the Benzeggagh-Kenane fracture criterion with a power of 1.5. Damage in cohesive elements is assumed to initiate when a quadratic interaction function involving the nominal stress ratios reaches 1.0, as described in equation (3.1).

$$\left(\frac{f_n}{f_n^0}\right)^2+\left(\frac{f_s}{f_s^0}\right)^2+\left(\frac{f_t}{f_t^0}\right)^2=1 \tag{3.1}$$

where f_n, f_s, and f_t denote the nominal stresses in the normal, first shear, and second shear directions, respectively; f_n^0, f_s^0, and f_t^0 are their corresponding elastic limits. The normal stress limit is taken from the measured bond strength in Figure 3.4(c). Other parameters f_s^0 and f_t^0 are determined from f_n^0 using existing relations (Shin and Lange 2012).

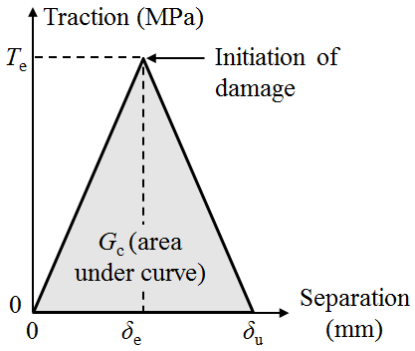

Figure 3.13. Traction-separation law of cohesive elements

As illustrated in Figure 3.14, concrete damaged plasticity models (Meng and Khayat 2016a) independent of mesh sizes were employed to account for potential damage in the overlay and the substrate, respectively. Due to limited compressive stress induced by shrinkage as indicated in Figure 3.15, both CC and UHPC were assumed to behave elastically in compression. For the CC, the model parameters were determined from the material properties at 56 days. For the UHPC, different material properties are utilized at different ages, as shown in Figure 3.4.

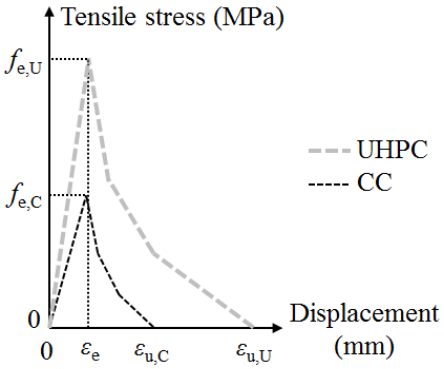

Figure 3.14. Concrete damaged plasticity models of the CC and UHPC

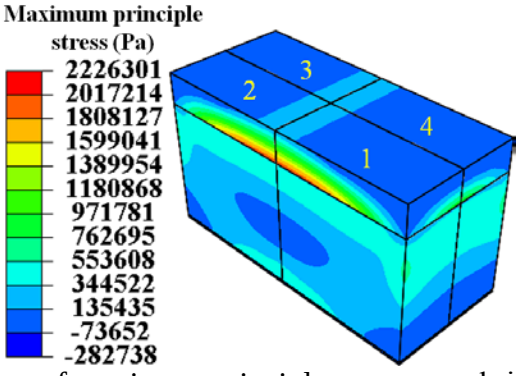

Figure 3.15. Distribution of maximum principle stress at a shrinkage strain of 160 με

3.4.3. Shrinkage. The shrinkage in the UHPC overlay was simulated in the finite element model by a change of equivalent temperature. The coefficient of thermal expansion for the UHPC was set to 10^{-5}/°C and the corresponding temperature change was determined to make the thermal strain in an unrestrained overlay equivalent to the measured shrinkage strain as presented in Figure 3.4(a).

3.4.4. Simulation Results and Discussions. The finite element model of the overlay-substrate system was analyzed under incrementally increasing shrinkage strains of the unrestrained overlay. Figure 3.15 shows a contour of the maximum principle stress (MPS, unit: Pa) at a shrinkage strain of 160 με and 320 με. Note the stress distribution of the entire specimen was presented by mirror imaging that of the analyzed quarter structure. The maximum positive stress (approximately 2.23 MPa) as shown in Figure 3.15 indicates tensile behavior near the bottom center of the overlay due to constraint by the substrate. The maximum negative stress (approximately 0.28 MPa) as shown in Figure 3.15 indicates compressive behavior towards two short-side edges of the overlay as a result of bowing action.

As the shrinkage strain in the unrestrained overlay increases from 0 με to 320 με, the maximum positive stress near the bottom center of the overlay first increases and then decreases. This is because the constraining effect by the substrate is weakening as the delamination propagates from the two short-side edges to the center of the overlay. Overall, the maximum positive stress in the overlay is significantly less than the tensile strength of the UHPC (11.0 MPa). The maximum positive stress in the substrate is less than 0.35 MPa, which is 10 times smaller than the tensile strengths of the CC (3.6 MPa). It can also be observed from Figure 3.15 that the maximum negative stress in the entire

overlay-substrate system is small. Therefore, both the overlay and the substrate remain in the elastic state with no damage. However, their interface is subjected to significant delamination due to the less-developed bond strength (1.31 MPa).

Figures 3.16(a)–(d) show the initiation and propagation of delamination at the overlay-substrate interface under various applied strains in the unrestrained overlay. Stiffness degradation index (SDEG) is introduced to describe the degradation level of cohesive elements. When the SDEG of a cohesive element reaches 1.0, the element is on the path of delamination and thus removed from the contour for better visualization as presented in Figures 3.16(c) and (d). When the overlay shrinkage is less than 160 με as shown in Figures 3.16(a) and (b), the interaction function on the left side of equation (3.1) is less than 1.0, indicating no delamination. At a shrinkage strain of 320 με, the interaction function has already reached 1.0 at the four corners of the overlay, as indicated in Figure 3.16(c). Delamination then propagates towards the center as indicated in Figures 3.16(c) and 3.16(d).

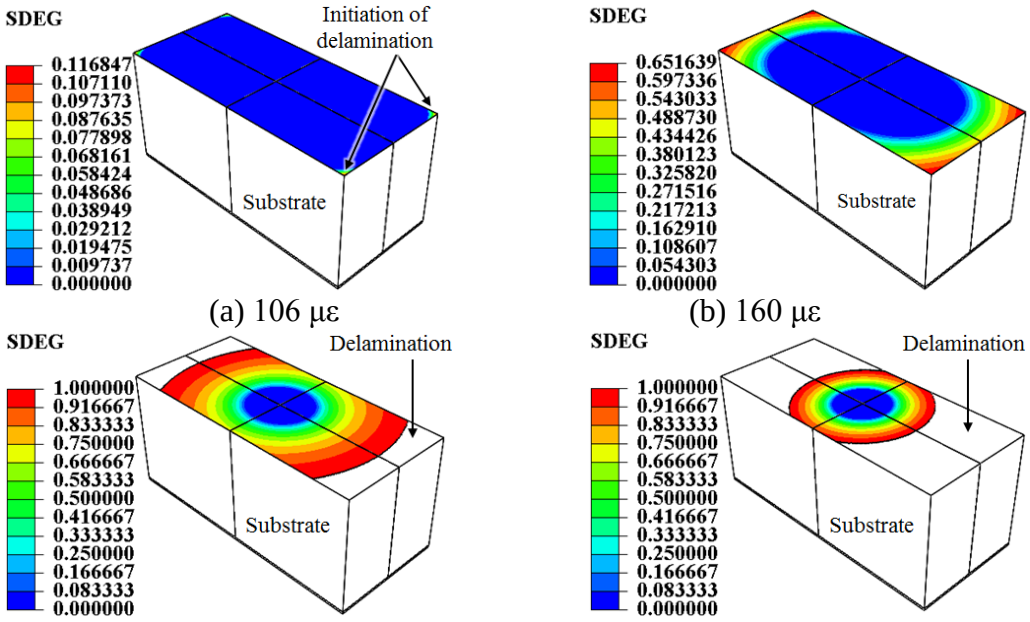

Figure 3.16. Damage initiation and propagation in the ITZ

Delamination initiates at four corners when the shrinkage strain in the overlay is between 160 με and 320 με, and then propagates as the shrinkage strain increases. Such a

trend and the delamination location are in general agreement with the measurement data as shown in Figure 3.10(a). During the first day of tests, delamination was detected at P1, P5, P7, P8, P9, P14, P15, and P16. Except for P5, these locations are near two short-side edges of the specimen. No delamination was detected near the center of the interface layer in the test strain range.

Figures 3.17(a)–(d) show the displacement contours at a shrinkage strain of 160 με, in which U1, U2 and U3 represent the displacement components along X, Y, and Z axes, respectively, and U represents the total displacement equal to the square root of the sum of squared (SRSS) displacement components. At the overlay-substrate interface, the differences in displacement components between the overlay and the substrate, ΔU1, ΔU2 and ΔU3, represent the slippage in X direction, the opening in Y direction, and the slippage in Z direction. SRSS represents the degree of delamination in space, ΔU.

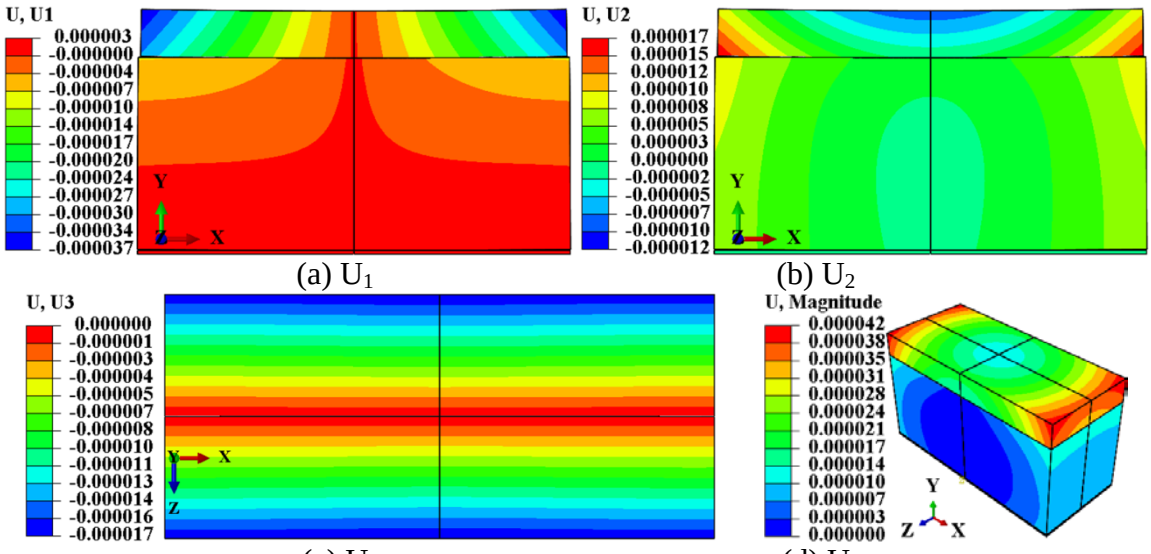

(a) U_1 (b) U_2

(c) U_3 (d) U

Figure 3.17. Displacement distributions (×100) at 160 με

The components (ΔU1, ΔU2, ΔU3) and the delamination (ΔU) are plotted in Figures 3.18(a)–(d) as a function of distance away from the transverse centerline (cut plane A in Figure 3.12) but along the z = 0 line as defined in Figure 3.17. The arrows in Figure 3.18 delineate the evolution trends of ΔU1, ΔU2 and ΔU3 components as well as the delamination ΔU. As shown in Figure 3.18(a), the longitudinal slippage increases

with the shrinkage strain till 240 με, and decreases after 320 με. These results indicate a reduced bending effect of the overlay at large shrinkage strains. This is because the extension of delamination weakens the substrate's restraint to the overlay. It can also be observed from Figures 3.18(b)–(d) that the opening and the transverse slippage as well as the delamination all increase monotonically with the shrinkage strain.

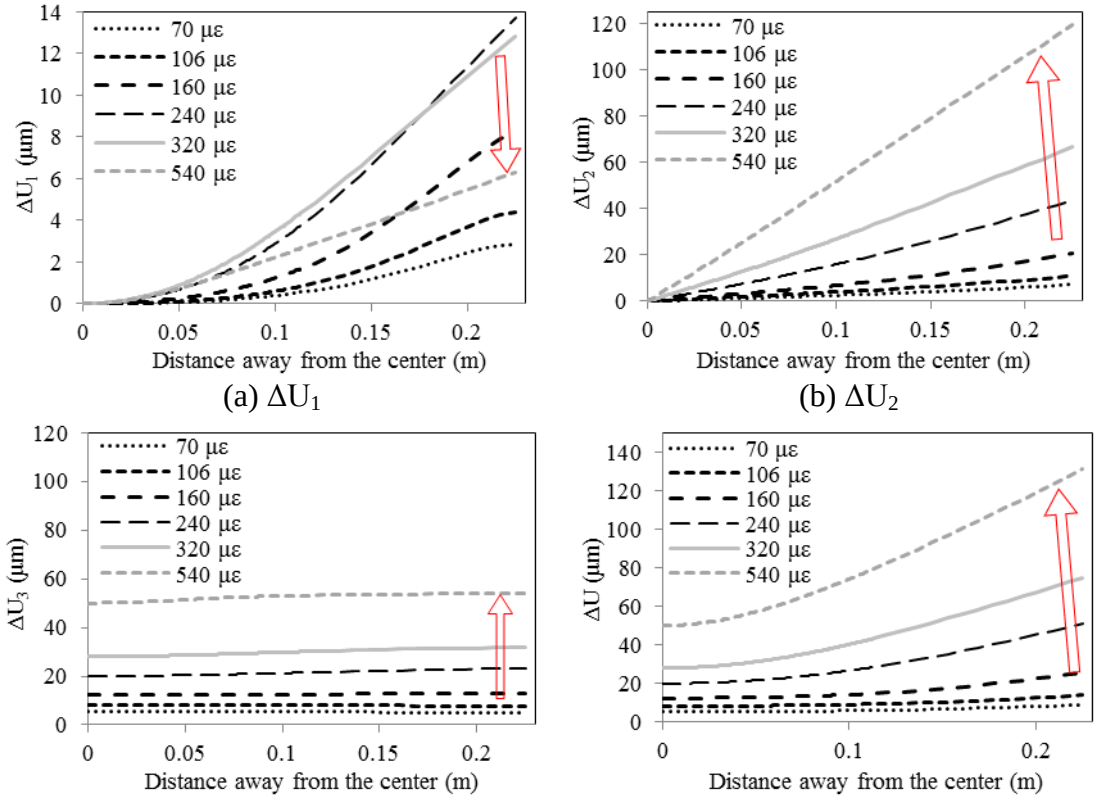

Figure 3.18. Deformation distributions

The most severe delamination occurs at the short-side edge of the specimen, specifically at Point P7 in Figure 3.6. It is plotted as a function of the shrinkage strain and compared with the experimental data in Figure 3.19. The simulated and measured results are in general agreement with a maximum relative difference of 26%. The discrepancies are caused by several reasons. First, the roughness of the delamination faces, which was not taken into account in modeling, can result in an underestimation of the opening displacement (U_2). Second, the fracture initiation and evolution behavior of the cohesive zone model may be inaccurate. Third, average values of the measured material properties

are used in modeling. Finally, the delamination determined from the strain measurements from the distributed fiber optic sensor is approximate.

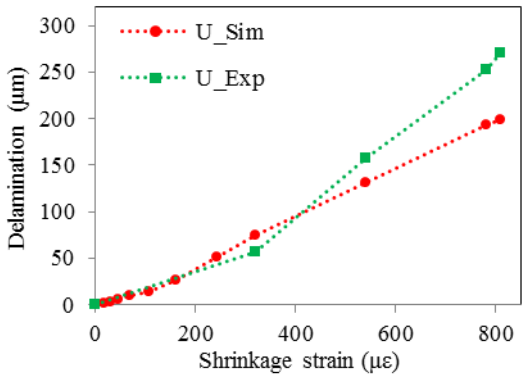

Figure 3.19. Delamination as a function of shrinkage strain in the unrestrained overlay

3.5. SUMMARY

Based on the above investigations, the following findings can be summarized:

Standard test measurements of early-age autogenous shrinkage in cement-based materials are in excellent agreement with shrinkage measurements using the proposed optical fiber sensor. A shrinkage-induced crack can be identified from the strain distribution so long as it intercepts the optical fiber. It can be located at the center of strain peak and can be sized based on the magnitude of the strain peak.

The distributed fiber optic sensor can be applied to monitor the initiation and propagation of delamination at the overlay-substrate interface. Delamination occurs at the location of each sharp peak that appears on the strain distribution directly measured from the sensor. The degree of delamination is proportional to the peak strain. When the distributed sensor passes through the overlay-substrate interface at spatially distributed locations, delamination at the multiple locations enables the construction of a 3D delamination profile in space and its progression over time with continuous monitoring. Although both the 2C and 3C sensors perform satisfactorily, the 3C sensor is recommended for delamination detection due to its higher mechanical strength.

The initiation and propagation of delamination at the overlay-substrate interface can be predicted using the finite element model with material properties obtained from standard tests and with cohesive elements used to represent delamination behavior. Prior

to delamination, the overlay and substrate are slightly bent upwards and the substrate separates from its supporting floor. Delamination takes place when the interfacial traction caused by shrinkage in the overlay exceeds the bond strength of the interface. Thus, delamination can be mitigated by controlling the shrinkage effect of the overlay material and enhancing the bond strength between the overlay and substrate. The predicted and experimental delamination values are in general agreement with 26% difference. Once initiated, delamination propagates along the interface and the bending curvature of the overlay and substrate is reduced. With an increase of shrinkage, the opening at the delaminated areas is reduced and the sliding distance is increased.

4. STRAINS AND CRACKS IN CONCRETE UNBONDED OVERLAY

4.1. BACKGROUND

As a time-saving and cost-effective alternative to reconstruction, deteriorated existing pavements can be rehabilitated for improved driving condition and extended service life using bonded or unbonded concrete overlays (Chen et al. 2014; Bao and Chen 2016). A bonded overlay is cast in direct contact with the existing pavement (substrate). Near the substrate surface, an interfacial transition zone can be formed to provide cohesive bond, which makes the overlay work as an integral part of the substrate.

Unbonded Portland cement concrete overlays have received increasing attention in new highway constructions and existing pavement rehabilitations (Liao 2011; Burnham 2013). Thin Portland cement concrete overlays have been cast on top of an existing pavement with a separation fabric layer to prevent the propagation of reflection cracking that has been observed in bonded concrete overlays. However, thin Portland cement concrete overlays can be more vulnerable to cracking than thick overlays due to reduced thickness. Cracks can potentially accelerate the deterioration and reduce the service life of concrete (Raoufi 2010; Tang et al. 2016). Therefore, strain measurement and crack detection are critically important in the maintenance and management of paved highway roads (Zhang *et al.* 2014).

In this study, fused silica SMFs are used as distributed fiber optic sensors with PPP-BOTDA for strain measurement and crack detection. Their sensing performance (sensitivity, resolution, and measurement distance) and practical limitations (susceptibility, strength, and deformability) are investigated for highway pavement applications. To this endeavor, a field-applicable sensor installation method is developed to protect optical fibers from damage during concrete casting. Six full-scale concrete panels were cast on a thin fabric sheet that represents a field application case in existing pavement rehabilitation. To quantify the ability of fiber optic sensors in operation and safety monitoring, each panel was tested under a dump truck first and then loaded to failure under three-point loading. The peaks of a directly measured stain distribution can be used to evaluate the width and location of cracks and thus the performance of concrete panels.

4.2. SENSOR INSTALLATION AND SPECIMEN FABRICATION

To protect optical fibers from damage in construction, an optical fiber installation method was developed and implemented in the casting process of concrete panel. As illustrated in Figure 4.1(a), an optical fiber was first attached on a 3 mm thick fabric sheet with adhesive, then covered by a thin layer of mortar in half cylinder (6–12 mm in radius), and finally embedded into concrete during the panel casting. The mortar sunk into the porous fabric by approximately 1.5 mm as indicated in the SEM image in Figure 4.1(b). The sample was cut from the tested pavement panels, polished, and then dried at 80 °C for 24 hours. Immediately before taking SEM imaging, the sample was coated with a very thin layer of gold for conduction. The magnification factor of the SEM image is 20X. The optical fiber is observed to be well embedded in the mortar, forming a good bonding interface.

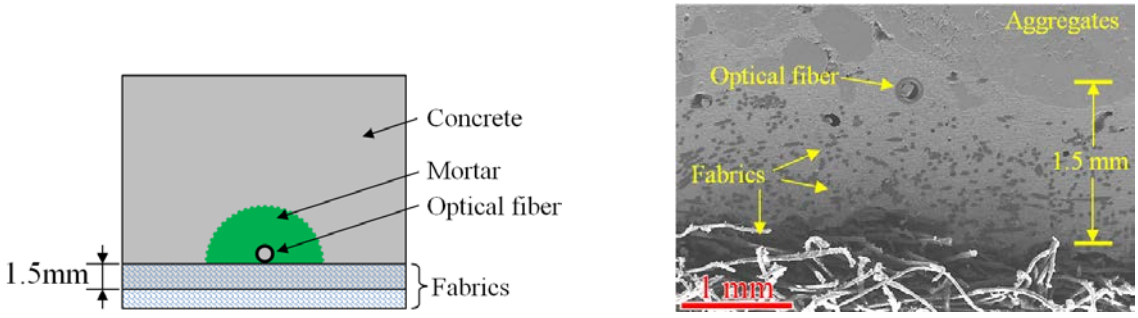

(a) Illustration (b) SEM image

Figure 4.1. Optical fiber embedded in specimen

In this study, six 183 cm × 183 cm × 7.5 cm concrete panel specimens were reinforced with alloy polymer macro-synthetic fibers. The mix designs of the concrete and the mortar are listed in Table 4.1. The average diameters of fine and coarse aggregates in concrete are 3.5 and 11.1 mm determined by sieve analysis (ASTM C136 2006). The initial setting time of the mortar was determined to be 90 min by ASTM standard test (ASTM C403/C403M 2008). A 3-mm thick fabric sheet was first laid on a 183 cm × 183 cm formwork. A bare optical fiber in loop was then attached on the fabric sheet in a specified pattern so that its ability for strain field measurement can be demonstrated. After the optical fiber was covered by mortar, concrete panels were cast

and cured for testing. The panels were covered using wet burlap and plastic sheet for 1 day, and then air-cured for 28 days.

The six panels were designated as P1 to P6 in Table 4.2. They were cast in two pours: first Panels P1, P4, and P5 and then Panels P2, P3, and P6. Two bare fibers in 25 mm spacing were embedded in each of the six concrete panels as designated by BF01, BF03-BF09, BF13, BF15, BF16, and BF18 in Table 4.2. For comparison, FBG sensors were also deployed at the center of four panels.

Table 4.1. Mix designs of the concrete and mortar (unit: kg/m^3)

Material	Water	Type II cement	Class C fly ash	River sand	Class C aggregate	Synthetic fiber	HRWR
Concrete	136	250	107	734	1064	3.57	1.78
Mortar	136	250	107	734	N.A.	N.A.	1.78

Table 4.2. Installed fiber optic sensors in each concrete panel

Concrete casting	Panel	Sensors in each panel		
		SMF-28e$^+$ fiber	1D FBG sensor	3D FBG sensor
First	P1	BF01*, BF13	–	–
	P4	BF03, BF15	FBG-1	–
	P5	BF04, BF16	–	–
Second	P2	BF07, BF08	FBG-2	–
	P3	BF06, BF09	–	FBG-3
	P6	BF05, BF18	–	FBG-4

*Italics font represents the fiber optic sensor fails to work properly, possibly due to damage during concrete casting or significant movement that causes acute angles of optical fiber, resulting in significant signal loss.

The first concrete pour began 30 min after mortar casting. Immediately after concrete pouring, measurements were taken from the optical fibers. As indicated in italics font in Table 4.2, *BF01* in Panel P1, *BF15* in Panel P4, and *BF04* and *BF16* in Panel P5 lost the optical fiber loops during the first concrete pour. This was mainly because the mortar was not hard enough to protect the optical fibers from local damage or prevent the fibers from significant macro-bending during concrete casting. Therefore, the second concrete pour started 2 hours after mortar casting. In this case, all the installed optical

fibers survived the concrete casting process. Overall, the optical fiber protection method with mortar proved effective after initial setting of the mortar (90 min).

To further quantify the protection level of mortar, free-fall impact tests were conducted on half mortar cylinders of various diameters and curing times. In each case, five fibers in U-shape were attached on a fabric sheet with adhesive as shown in Figure 4.2, which was placed at the bottom of a 310 mm × 260 mm formwork in plan. Each optical fiber consists of two straight portions (220 mm each) and half a circle of 15 mm in radius. The 5 samples were placed side by side with even spacing of 30 mm. During each test, 0.005 m^3 fresh concrete was poured into the center of the formwork out of a bucket at a height of 0.5 m so that the middle U-shaped fiber sample was subjected to most severe impact. The percentage of optical fibers that survived each impact test or survival rate (%) is presented in Table 4.3. The five optical fibers in loop all survived the impact test when their protective mortar cylinder was at least 6 mm in radius and was air-cured for at least initial setting time, which is 90 minutes.

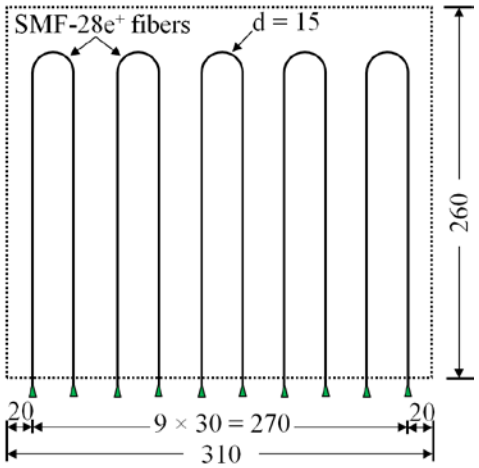

Figure 4.2. Schematic view of optical fiber layout in free-fall impact tests (unit: mm)

Table 4.3. Optical fiber survival percent with mortar diameters and curing times

Cylinder radius (mm)	Curing time (min)				
	30	60	90	120	150
3–5	20%	40%	40%	60%	80%
6–10	40%	80%	80%	100%	100%
11–15	40%	60%	80%	100%	100%

Since the results from six panels are in general agreement, only those from Panel P3 are presented, analyzed, and discussed in the following sections. Panel P3 was instrumented with two independent distributed fiber optic sensors named BF06 and BF09, respectively, and a FBG sensor.

4.3. TRUCK LOADING TESTS

The truck load tests of the concrete panels are reported in this section.

4.3.1. Experimental Program. After 28-day curing, the concrete panels were laid on the strong floor and tested under truck loads as shown in Figure 4.3(a). The truck's dimensions are shown in Figure 4.3(b). Two load levels were considered: empty and fully loaded. The weights of the front and back axes were respectively 4,400 and 5,200 kg for the empty truck and 6,250 and 14,200 kg for the loaded truck.

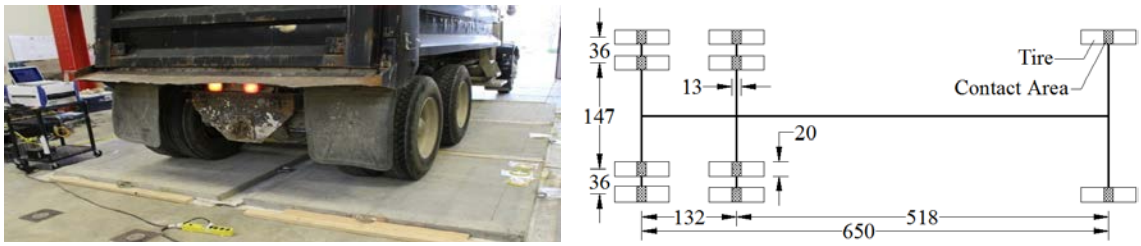

(a) Truck on panels (b) Dimensions of the truck (unit: cm)

Figure 4.3. Truck load test

Figure 4.4 shows the layout of distributed and FBG sensors as well as the positions of truck's tires on Panel P3. In this study, a U-shape distribution of distributed sensors is utilized to provide relatively detailed information of the strain and potential crack field of the pavement panel with one measurement.

For easy reference, the curve portions of a looped optical fiber sensor were marked by A, B, …, L, M, and A. The multiple intersections between the distributed sensor and any crack were designated as "Ca-b", where "C", "a", and "b" represent a crack, the crack number, and the intersection number of the crack with the sensor, respectively. All tests were conducted in the laboratory at constant 22 °C.

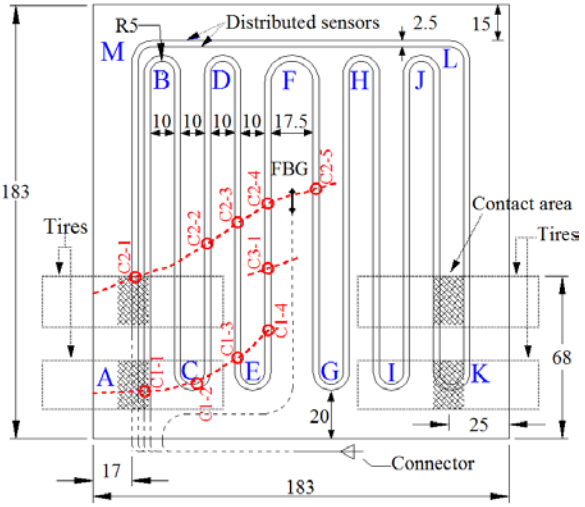

Figure 4.4. Sensor layout and three cracks in P3 under the fully loaded truck (unit: cm)

4.3.2. Experimental Results and Discussions. The Brillouin frequency shift of each panel was directly measured with the Neubrescope and converted into strain change according to equation (2). Figure 4.5(a) and (b) show the strain distributions in BF06 and BF09, respectively, under the first pass and first stop (P1S1) of the dump truck. The horizontal axis represents the distance measured from the pulse end of an optical fiber, including both communication (dashed line in Figure 4.4) and sensor (solid line in Figure 4.4) portions. The strain distributions measured from BF06 and BF09 were in excellent agreement. The slight difference between them was due to the 25 mm separation distance between BF06 and BF09. At the distance of 24.5 m, two peaks (C2-2 and C1-1) were detected from the BF06 while only one peak (C2-1) was detected from the BF09. This was because the sensor portion of the BF09 was 0.3 m shorter than that of the BF06, and the first crack (C1) was not intercepted by the BF09 sensor.

Due to uneven surface of the strong floor on which the test panel was placed, three cracks appeared in P3 under the fully loaded truck as indicated in Figure 4.5. Through comparison of the strain distributions under the empty and fully loaded trucks in Figure 4.5(a), it can be observed that cracks due to the fully loaded truck can be detected from the sharp peaks such as C1-1 and C2-1 at the distance between 24 and 25 m. The sensor portion of an optical fiber in direct contact with concrete senses the strain change in the panel. When the concrete panel cracked, the sensor passing through the crack would locally be elongated as reflected by a sharp peak in the measured strain

distribution as illustrated in Figure 4.5 (Bao *et al.* 2015). The crack can thus be detected at the location of the peak in a strain distribution as verified by measuring the physical position of the crack on the concrete panel. The crack width is likely correlated with the strain peak value. Spatial resolution is usually a critical issue for the detection of nearby cracks. In this study, two cracks with 0.1 m spacing were successfully distinguished as illustrated in Figure 4.5(b). Therefore, a 0.1 m spatial resolution has been verified for crack detection although PPP-BOTDA can in theory provide 20 mm spatial resolution (Kishida *et al*. 2005, Neubrex Co. Ltd. 2013).

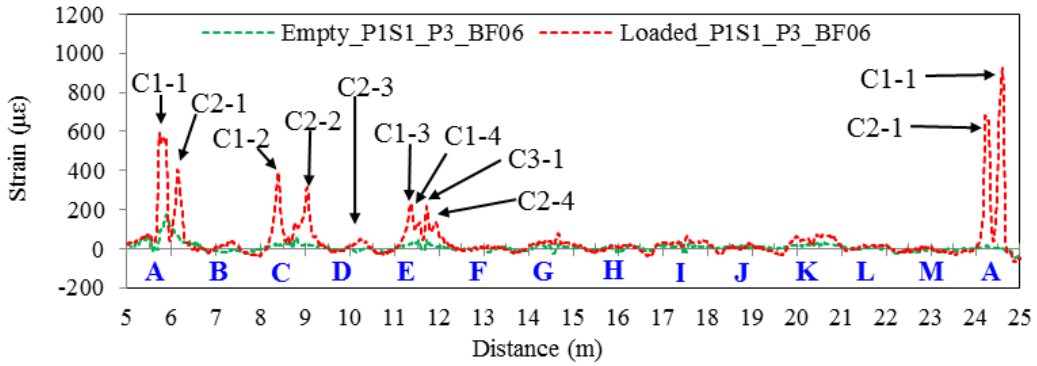

(a) BF06

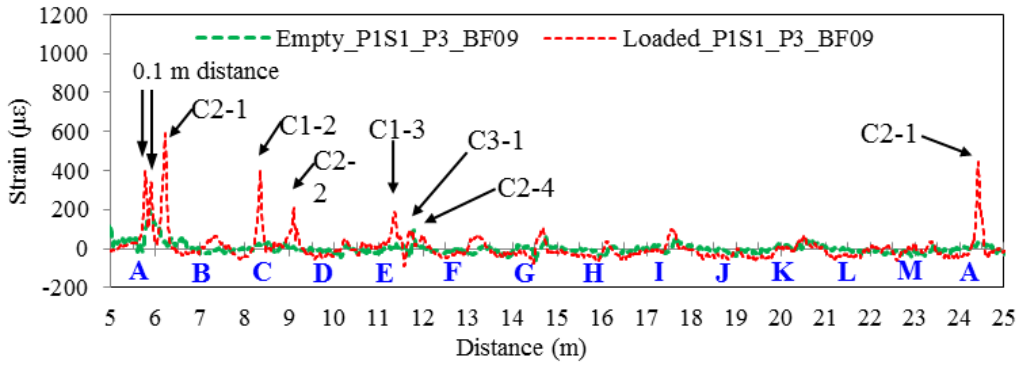

(b) BF09

Figure 4.5. Strain distributions in Panel P3 under truck loads

4.4. THREE-POINT BENDING TESTS

After the truck load tests, the panels were loaded to failure using a load frame under a "three-point" bending setup under a displacement control mode.

4.4.1. Experimental Setup. Figure 4.6 shows the flexural test set-up. The two reaction forces were transferred through two orthogonal rigid beams into a line load

applied on each panel at its mid span. Each panel was simply supported on two steel rollers and beams, and loaded in displacement control with a rate of 2 mm/min. Mid-span deflections and support settlements were measured by LVDTs. The clear span length was 1.5 m. The induced strains in the concrete panel were measured by the two distributed fiber optic sensors with the Neubrescope and by the FBG sensor with an optical spectrum interrogator (OSI, model: SM125). The measurement accuracy and repeatability are 1 pm (10^{-3} nm) and 0.5 pm, respectively.

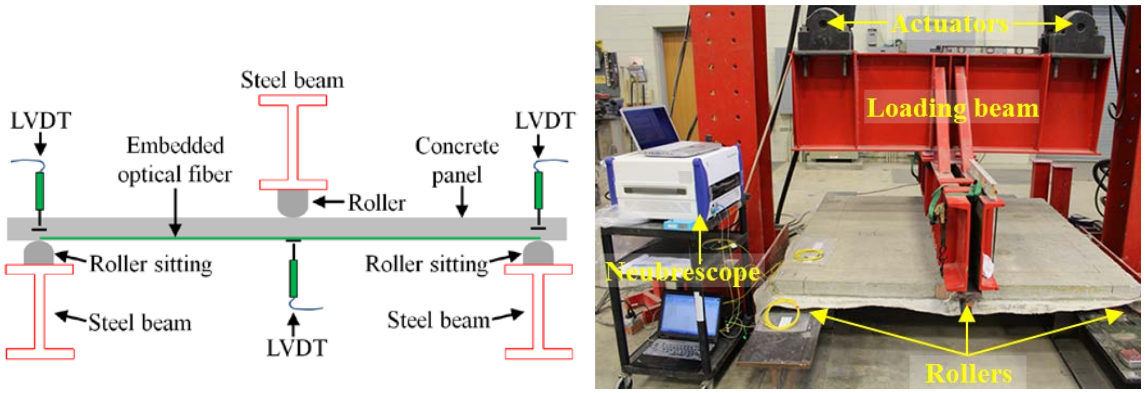

Figure 4.6. Load frame test setup

4.4.2. Results and Discussions. Figure 4.7 shows the load-deflection curves of Panel P3. The panel was loaded linearly with the applied deflection until a major crack appeared at 3.8 mm mid-span deflection.

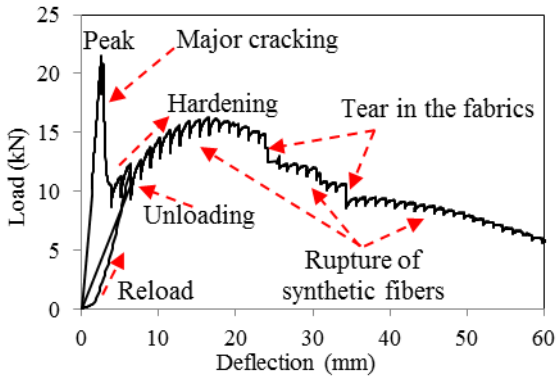

Figure 4.7. Load-deflection curve of Panel P3

As a result of the concrete cracking, the load suddenly dropped from 21 kN to 8.8 kN and was then increased again with the deflection since the microfibers within the concrete matrix and the fabric sheet underneath the panel restrained the crack from widening. However, the overall slope of the load-deflection curve is smaller than that prior to the major crack, indicating a softening effect of the cracked panel. As the panel was further deflected, the microfibers gradually broke or were pulled out of the concrete matrix as observed during tests, resulting in a sudden load reduction approximately every 1 mm to 2 mm deflection increment. In this case, the load envelope except for local drops was relatively smooth. However, when part of the fabric was torn apart at mid-span deflections of 25 and 34 mm, the load drops were more significant than those of microfiber effect. The load remained to be approximately 8.9 kN at a mid-span deflection of 25 mm, and then gradually decreased to zero as the actuators extended 76 mm.

After the panel failed in flexure, the bottom fabric sheet was removed. A major crack and several micro-cracks were located by tape measurements. As shown in Figure 4.8, the major crack was approximately in the middle of span and intersected the two distributed sensors at the labeled locations (thick dash line) corresponding to strain peaks in Figure 4.5. The micro-cracks in blue color in Figure 4.8 were caused by truck loads.

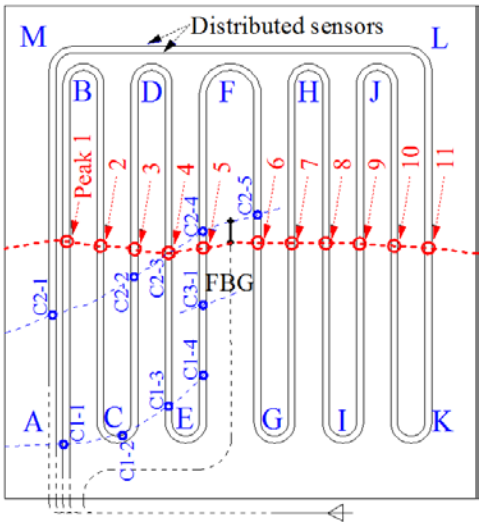

Figure 4.8. Cracks in Panel P3 after load frame tests

At six different levels of the mid-span deflection, the measured strains along a portion of the two distributed sensors from 5 m to 16 m distance are presented in Figures

4.9(a) and (b) from the Sensors BF06 and BF09, respectively. At each loading level, the measurements from BF06 and BF09 agree well. Similar to the strain distributions under truck load tests as shown in Figures 4.5(a) and (b), cracks crossing a distributed sensor can be identified as sharp peaks in corresponding strain distribution (Feng *et al.* 2013).

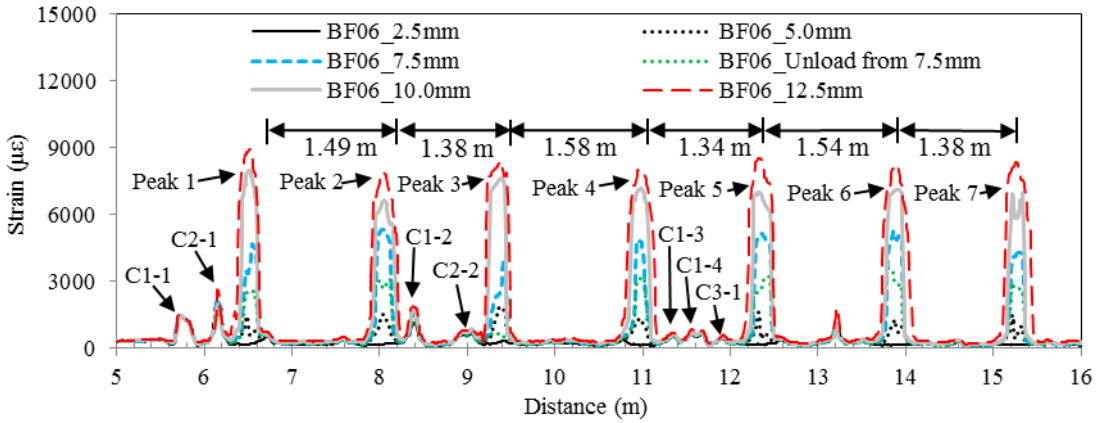

(a) BF06

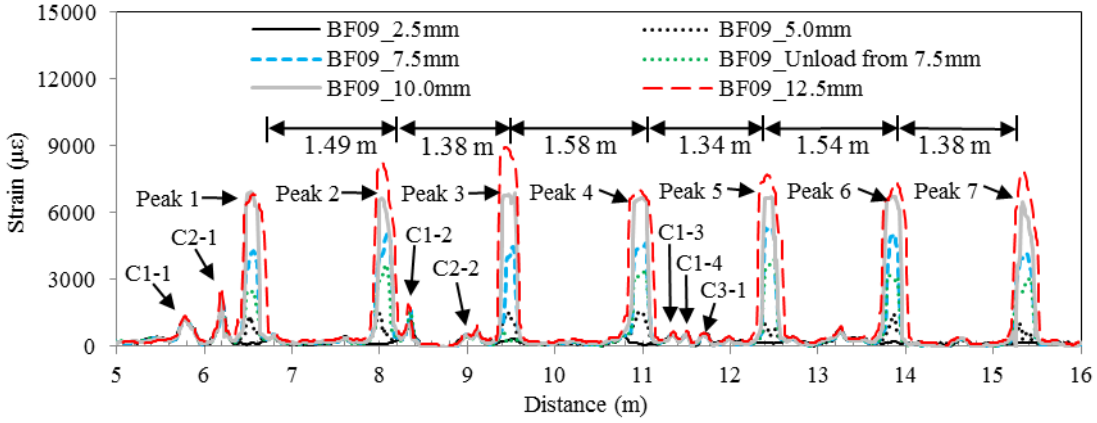

(b) BF09

Figure 4.9. Strain distributions in Panel P3 in bending test

The crack locations in Figure 4.8 were in excellent agreement with the locations of their corresponding peaks in Figure 4.9(a) and (b). For example, the distance from the starting point of the BF06 to Peak 1 in Figure 4.9 was approximately 6.56 m, including 5.64 m outside and 0.92 m inside Panel P3. Since it was 1.44 m away from Peak 1 along the BF06, Peak 2 could be identified at the distance of 8.00 m as verified in Figure 4.9. The magnitude of multiple strain peaks corresponding to the same major crack varied to certain degree since the strains were measured at different parts of the crack with

potentially varying crack widths. It can be observed from Figure 4.9 that the magnitude of each strain peak increased with the mid-span deflection as a result of crack widening. Due to bonding between the concrete and the optical fiber, the fiber passing through the crack was subjected to increased strain as the crack becomes widened.

4.5. CRACK DETECTABILITY

The strain distributions measured using the distributed sensors are replotted to visualize the cracks in the concrete panel.

4.5.1. Visualization of Crack Distribution. Based on the original serpentine optical fiber deployment scheme, the measured strain distribution along an optical fiber shown in Figures 4.9(a) and (b) can be re-produced into a two-dimensional (2D) strain field in the plane of the concrete panel, as shown in Figure 4.10.

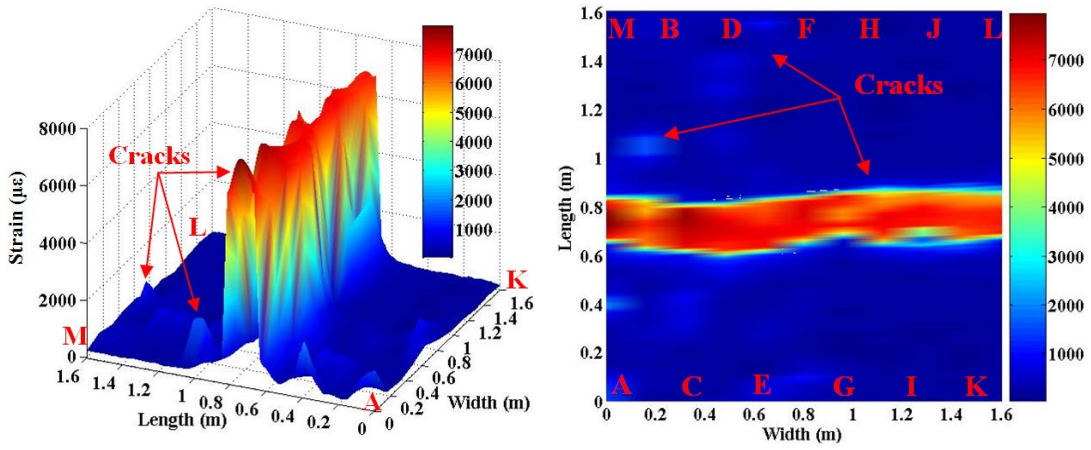

(a) Perspective view (b) Top view

Figure 4.10. Two-dimensional strain field in P3 at the mid-span deflection of 10 mm

Since the two optical fibers are used to measure axial strains only, the 2D field is for one component of strain along many optical fiber segments that were deployed in parallel. The perspective view and the top view of the 2D strain field are plotted in Figures 4.10(a) and (b), respectively. Specifically, the parallel portion of the distributed BF06 sensor can be divided into 11 segments, each 1.6 m long, represented by A-B, B-C, C-D, …, and K-L, as shown in Figure 4.8. Each part is denoted by the “Length” axis in Figure 4.10. The strain distributions in the eleven segments can be plotted in one figure

with a separation distance in between according to the installation scheme of the optical fiber. The strain distributions in between every two of the eleven distributions are determined by linear interpolation. In this way, the strain field over the A-K-L-M area shown in Figure 4.9 is determined as presented in Figure 4.10. One advantage of the strain field in Figure 4.10 over the 1D strain distribution in Figures 4.9(a) and (b) is to enable an automatic identification of both orientation and length of cracks. For example, multiple cracks can be detected from the color-coded strain field. As shown in Figure 4.10, the major crack corresponds to the largest strain represented by a red band and is located at the center of the red band. The microcracks can also be identified.

4.5.2. Considerations on Crack Width. The red bands in Figure 4.10(a) and (b) reflect the position of the major crack. However, the bandwidth is not equal to the crack width. As shown in Figure 4.10(b), the bandwidth is approximately 190–200 mm while the crack width was measured to be 1.5 mm to 2.0 mm using a Crackscope (model: CS-100, minimum scale: 50 μm). The broadening of bandwidth likely resulted from debonding between the glass cladding and the inner coating of optical fiber.

The inner coating is made of soft material that is weak in shear strength. This ensures the coatings can be easily stripped off the optical fiber for fiber splicing operation (Kouzmina *et al*. 2010). However, under a large strain gradient near crack faces, there is a significant shear strain between coating layers of the optical fiber in order to transfer the normal strain in the optical fiber, which can cause debonding in optical fiber (Li *et al*. 2003, Feng et al. 2013). The debonding length changes with the loading scenario and level. When the crack width is small, the debonding is insignificant. For example, C2-1 in Figure 4.9(a) is sharper than Peak 1 since C2-1 corresponds to a micro-crack whose opening width is smaller than that of the major crack. Debonding only happens when crack width is substantially enlarged when the widths of peaks can be observed to be broadened, as shown in Figures 4.8(a) and (b). Either before or after debonding occurs the peak strain is associated with the crack width. This provides a way to estimate the crack width, based on the measured strain distribution, no matter whether the crack is visible or hidden inside.

Figure 4.11 relates the width (w) of the major crack to the peak strain ($\Delta\varepsilon_{max}$). Two linear equations were employed to fit the data before and after substantial

debonding, respectively. For crack widths less than 100 μm when debonding in optical fiber was insignificant, the linear coefficient was determined to be 53.3 μm/με with R^2 = 0.670. For crack widths exceeding 100 μm, significant debonding occurred and the crack-induced deformation in optical fiber would be averaged over the debonding length. Therefore, the same increase in crack width led to smaller changes in the peak strain. The linear coefficient was increased to 225 μm/με with R^2 = 0.690. The two equations provided quantitative approximations for the crack width. Factors affecting the accuracy and repeatability of the prediction using the two equations included: (i) the crack widths were measured using the crackscope that had limited accuracy, since tiny cracks were difficult to read, and the crack faces were rough and uneven; and (ii) the strain measurements from the Neubrescope contained error. A better way to control and measure the crack width is needed to obtain a relationship between the crack width and the measured strain with higher accuracy and less variation.

Figure 4.11 reveals that the distributed sensor is sensitive to micro-scale cracks. In the quasi-static loading scenario, it demonstrated an operating range up to 3 mm before the fiber ruptured, which implied its feasibility in pavement applications. As to the concerns about the sensor's damage in engineering practice, after significant cracking occurs in a portion of pavement, the sensor can be repaired at the time when the pavement is rehabilitated. The sensor's break points can be detected using optical time domain reflectometry (OTDR) technology (Leung *et al*. 2000), and the break points can be fixed using fusion splice technique.

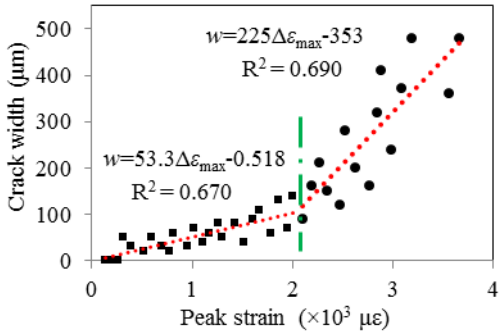

Figure 4.11. Correlation of crack width and peak strain

4.5.3. Comparison with FBG Sensor. The onset and widening of the major crack in P3 are illustrated in Figure 4.12 on a cross section of the panel through the FBG sensor. The point FBG sensor is parallel to the distributed sensors BF06 and BF09. The major crack passed around the distributed sensors and the transmission cable of the FBG sensor. The transmission cable consisted of a single-mode optical fiber and a 1-mm thick steel cylindrical spiral that was coated with a 1-mm thick polyethylene.

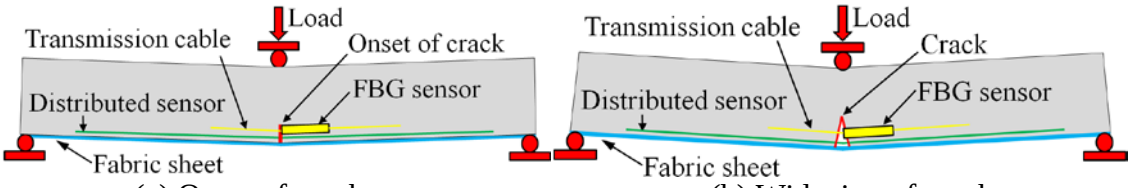

(a) Onset of crack (b) Widening of crack

Figure 4.12. Widening of the major crack in P3

The strains measured from the FBG sensor are compared in Figure 4.13 with those from the BF06 after small temperature variation has been compensated. For this comparison, a point on the BF06 at 11.69 m distance is selected due to its proximity to the FBG sensor. The solid line and the dash line in Figure 4.13 represent the measurements from the FBG sensor and from a point of the distributed BF06 sensor, respectively. The induced strains in both sensors linearly increased till an applied mid-span deflection of 3.8 mm when the major crack occurred. When the panel was unloaded from approximately 6.35-mm to zero mid-span deflection, the measured strain differed from the original value because of the permanent damage. To quantify the relative difference between the distributed sensor and point sensor results, a robust index (τ) is defined in equation (4.1) based on the normalized difference of two sets of strain data:

$$\tau = \sqrt{\frac{1}{N}\sum_{1}^{N}\frac{[S_{BF}(i) - S_{FBG}(i)]^2}{\sqrt{S_{BF}^2(i)}\sqrt{S_{FBG}^2(i)}}} \tag{4.1}$$

where i (=1, 2, 3,…, 16) denotes the measurement data point; N is the total number of measurements during one test; $S_{BF}(i)$ and $S_{FBG}(i)$ represent the i^{th} strains measured by BF06 and FBG sensors, respectively. For Panel P3, τ is calculated to be 2.12% when the

mid-span deflection ranges from 0 mm to 18 mm, demonstrating that the measurements from the two sensors are in reasonable agreement.

Figure 4.13 indicates that the point FBG sensor works until the mid-span deflection exceeds 57 mm with a maximum strain of 275 με, and the distributed BF06 sensor functions till 18 mm mid-span deflection with a maximum strain of 238 με. At a first glimpse, it seems that the FBG sensor can provide a larger measurement range than the BF06 sensor. This is not the case since the same BF06 sensor provides strain measurements elsewhere up to 9000 με as shown in Figure 4.9(a), which substantially exceeds 275 με sensed by the FBG sensor. The optical fiber BF06 actually ruptured far away from the point near the FBG sensor. Since the PPP-BOTDA used the optical fiber loop for strain measurement, once broken elsewhere, the optical fiber loop was open and no further measurement was available with PPP-BOTDA measurement.

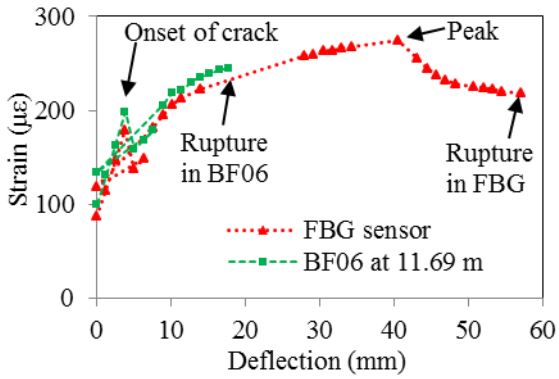

Figure 4.13. Comparison of strain measurements by BF06 and FBG sensors

In fact, the distributed fiber optic sensors are advantageous over the point FBG sensor in terms of their ability to locate cracks. In this study, the FBG sensor was installed at the mid-span of the concrete panel where cracks most likely occurred. During the tests, it was confirmed that the major crack did happen around the mid-span but passed around the transmission cable of the FBG sensor. If the FBG sensor would be right in the middle of the major crack, the FBG sensor would have ceased to function earlier. When the crack was formed, the strain at the crack faces was partially released as reflected in a sudden drop of the FBG measured strain in Figure 4.13. With further widening of the major crack, the FBG sensor next to the crack was pulled at one end and

hence measured increasing tensile strain till its peak value. The peak represents the onset of break in the steel spiral and polyethylene coating of the transmission cable for the FBG sensor. When the fiber in the transmission cable ruptured, the FBG stopped working.

4.6. SUMMARY

Based on the above investigations, the following summaries can be drawn:

On the average, the distributed fiber optic sensors can withstand 22.6 N in axial force and 2.33% in axial strain so that the fiber stiffness in tension is approximately 9.7×10^{-4} N/με. The sensitivity coefficient of Brillouin frequency shift for strain measurement is determined to be 5.43×10^{-5} GHz/με.

The field-applicable installation method for fiber optic sensors was demonstrated to be effective with full-scale panel tests. Optical fibers can be protected from brutal actions during concrete casting by half mortar cylinders of 12 mm in diameter after the mortar has been cured for at least initial setting time, which is approximately 90 min.

The peaks in strain distribution represent multiple cracks in concrete panels that can be detected by distributed sensors. The location and magnitude of each strain peak correspond to the location and width of its corresponding crack, respectively. Two cracks with a 0.1 m separation distance were demonstrated to be discernable.

The distributed fiber optic sensors embedded in concrete are feasible for structural health monitoring. The reduced size of optical fiber and detailed measurement results make them promising for wider applications in flexible pavements, thin bridge decks, and other structures. However, due to the fragility of optical fiber, appropriate procedure should be followed in the installation of optical fiber and construction of the structures.

5. DISTRIBUTED FIBER OPTIC SENSORS FOR MEASUREMENTS OF TEMPERATURE AND STRAIN AT HIGH TEMPERATURES

5.1. BACKGROUND

Fire is one of the most dangerous events that can cause structural failure and catastrophic consequences to the public. The load-carrying capacity and stability of structures can significantly degrade due to adverse temperature-induced deformations and material properties reduced at elevated temperatures (Kodur et al. 2009, 2010). To assess the thermo-mechanical conditions of a structure, temperatures and strains are critical information of the structure (Li et al. 2012; Jeffers and Sotelino 2012). Traditional measurement tools for structural fire engineering primarily include thermocouples for temperature measurement, strain gauges for local deformation measurement, and displacement sensors for displacement measurement (Tan et al. 2007; Dwaikat et al. 2011). However, traditional electrical resistance sensors are generally susceptible to electromagnetic interference, and only allow for the measurements at discrete points where the sensors are deployed. A great number of sensors need to be employed to obtain measurements at multiple locations of the specimen, which involves massive wires of the sensors in the case of large-scale specimens.

When a thermocouple is used to measure gas temperature, radiation of thermocouple could significantly affect the measurement results. Besides, the operation temperature is limited by the coating of wire at high temperature, because the sensor fails quickly with the temperature-induced deterioration of the coating for isolation. Under such circumstances, fiber optic sensors have drawn intense research interest in recent years, due to their unique advantages such as immunity to electromagnetic interference, lightweight, compact size, and excellent durability in harsh environments (Bao and Chen 2015). A variety of fiber optic sensors have been developed to provide effective tools for high temperature applications. Multiple physical parameters were measured, which included temperature, strain, pressure, refractive index, current/voltage, etc. (Bao and Chen 2011).

In this study, a PPP-BOTDA distributed temperature and strain sensor was investigated with a fused silica SMF. The strain and temperature sensitivity coefficients were calibrated and their coupling at high temperatures was investigated in detail. The

sensing performance was evaluated in terms of accuracy, repeatability, and operating range. The mechanical properties of the fiber before and after heat treatment were compared. Finally, it was validated in an application setting.

5.2. EXPERIMENTAL PROGRAM

As shown in Figure 5.1, the experimental setup consisted of an electric furnace for temperature application, a translation stage for loading, a distributed optic fiber sensor, and a Neubrescope (model: Neubrex NBX-7020) and a laptop computer for data acquisition. The furnace was composed of a steel housing, heat insulation fabrics, a center 200-mm heating coil wrapped ceramic tube, and a thermocouple deployed at the middle of the ceramic tube to monitor and control the heating temperature up to 1000 °C with an accuracy of ± 0.5 °C. The micrometer had an operating range of 20 mm with ±0.5 μm accuracy; the load transducer had a capacity of 50 N with ±0.2% accuracy at room temperature. The SMF was uncoated and made of fused silica. Its effective refractive index and mode field diameter were 1.4679 and 10.4 μm, respectively. Its dispersion and attenuation were less than 18.0 ps/nm/km and 0.02 dB/km, respectively, at 1550-nm wavelength. The fiber passed through the furnace back and forth and formed a loop with the Neubrescope for PPP-BOTDA measurement. The two portions of the fiber passing through the furnace were parallel and closely spaced. One portion was free of strain, referred to as temperature sensor, while the other was fixed on the translation stage and subjected to strain, referred to as strain/temperature sensor. The temperature sensor provided temperature compensation to the measurement by the strain/temperature sensor.

Critical points along the two sensors were marked with capital letters A-H. For the strain/temperature sensor, A and F represented the end supports for the optic fiber, B and E were located at the two exits of the furnace, and C and D were at the two entrances of the center ceramic tube. Point G was in between B and C; Point H was in between D and E. Both G and H represented temperature drop locations due to heat transfer in the furnace. The portions A-B and E-F were mainly subjected to strain changes; C-D was subjected to both strain and temperature changes; B-C and D-E were subjected to strain change and partially subjected to temperature change due to the heat transfer effect. The heated portion was represented by G-H and H-G for the two sensors, respectively.

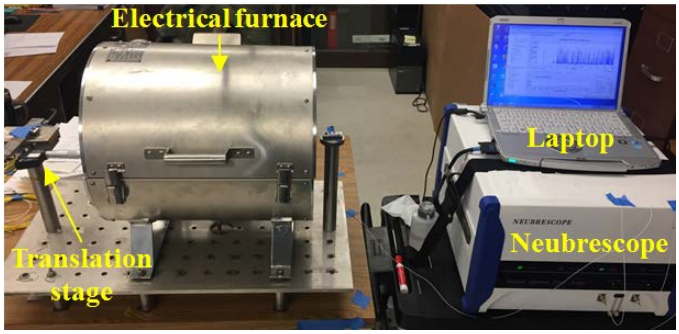

(a) Photograph

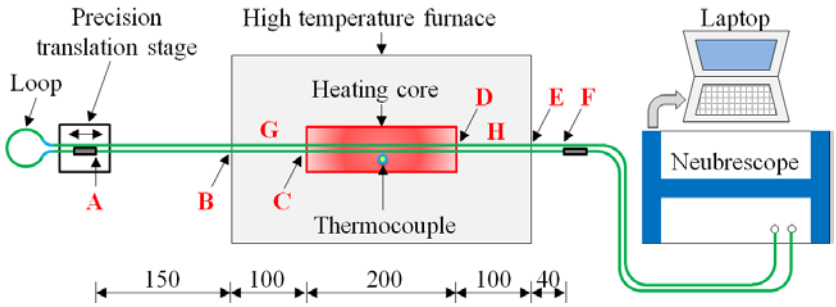

(b) Schematic illustration

Figure 5.1. Experimental setup

Ten sensors were tested to calibrate the sensitivity coefficients of Brillouin frequency to the changed of strain and temperature. Each sensor was heated incrementally from room temperature to 100–800 °C with a step size of 100 °C and 850 °C, and cooled down to room temperature in a reversal order. At each temperature, the test fiber was incrementally loaded to various strain levels, and then released in a reversal order. These steps formed a complete heating-cooling cycle. Three cycles were conducted for each sensor to evaluate the variability.

5.3. THERMO-MECHANICAL ANALYSIS

At high temperature, the Young's modulus of fused silica fiber significantly changes with temperature. The load-induced strain in fiber changes with temperature. A thermo-mechanical analysis is required to evaluate the load-induced strain.

5.3.1. Temperature-Dependent Young's Modulus. The Young's modulus of fused silica fiber can be assessed from the measured non-uniform strain distribution.

Figure 5.2 shows a thermo-mechanical model of fiber portion A-F of the strain/temperature sensor, under an axial load *P*. The center portion G-H is subjected to

the maximum temperature (T) in the middle of ceramic tube, while the remaining portions A-G and H-F are exposed to room temperature. Their corresponding Young's moduli are represented by $\phi(T)E_0$ and E_0, respectively. Here, $\phi(T)$ is a correction factor to the Young's modulus due to the effect of high temperature. The lengths of A-G, G-H, and H-F are denoted by l_1, l_2, and l_3, respectively, and in total, $L= l_1+l_2+l_3$. The total elongation of the fiber A-F is represented by ΔL.

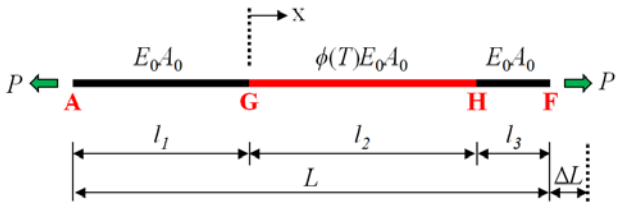

Figure 5.2. A thermo-mechanical model of fiber optic sensor under tension

The change in cross sectional area (A_0) of the optic fiber due to thermal expansion was negligible since the coefficient of thermal expansion (CTE) of fused silica was about 0.5–0.6 ppm/°C. Therefore, the force equilibrium equations of the three fiber portions in series are:

$$E_0A_0\varepsilon_1 = \phi(T)E_0A_0\varepsilon_2(T) = E_0A_0\varepsilon_3 \tag{5.1}$$

The correction factor, $\phi(T)$, can be derived from equation (1) and expressed into:

$$\phi(T) = \varepsilon_1 / \varepsilon_2(T) = \varepsilon_3 / \varepsilon_2(T) \tag{5.2}$$

where ε_1, ε_2(T), and ε_3 represent the strains of portions A-G, middle of G-H portion, and H-F, respectively. They can be measured from the strain/temperature sensor with compensation from the temperature sensor.

5.3.2. Load-Induced Strain Redistribution at High Temperatures. The temperature distribution within G-H and H-G under heating can be considered to be linear and symmetrical about the middle of the furnace where the sensor was subjected to the maximum temperature.

The ratio of the temperatures at G and H to the maximum temperature is represented by β (< 1). In this case, the correction factor over the left half of G-H can be approximated by linear interpolation:

$$\phi(T,x)=\phi(\beta T)+2x[\phi(T)-\phi(\beta T)]/l_2,\ 0\le x\le l_2/2 \tag{5.3}$$

The corresponding strain over the left half of G-H portion is then given by:

$$\varepsilon_2(T,x)=\frac{P}{\phi(T,x)E_0A_0}=\frac{P}{E_0A_0\{\phi(\beta T)+2x[\phi(T)-\phi(\beta T)]/l_2\}} \tag{5.4}$$

The elongations of A-G, G-H, and H-F portions are denoted by Δl_1, Δl_2, and Δl_3, respectively. They can be calculated by:

$$\Delta l_1=\frac{Pl_1}{E_0A_0},\ \Delta l_2=2\int_0^{l_2/2}\varepsilon_2(T,x)dx=\frac{Pl_2}{E_0A_0}\frac{\ln[\phi(T)/\phi(\beta T)]}{\phi(T)-\phi(\beta T)},\ \Delta l_3=\frac{Pl_3}{E_0A_0} \tag{5.5}$$

The total length change of A-G, G-H, and H-F can be written as:

$$\Delta L=\Delta l_1+\Delta l_2+\Delta l_3=\frac{P(l_1+l_3)}{E_0A_0}+\frac{Pl_2}{E_0A_0}\frac{\ln[\phi(T)/\phi(\beta T)]}{\phi(T)-\phi(\beta T)} \tag{5.6}$$

By solving P/E_0A_0 from equation (5.6) and substituting it into equation (5.4), the strain at any point of the fiber along the ceramic tube can be expressed into:

$$\varepsilon_2(T,x)=\frac{\Delta L}{\left\{\phi(\beta T)+2x[\phi(T)-\phi(\beta T)]/l_2\right\}[l_1+l_3+\frac{\ln[\phi(T)/\phi(\beta T)]}{\phi(T)-\phi(\beta T)}l_2]},\ 0\le x\le l_2/2 \tag{5.7}$$

5.4. RESULTS AND DISCUSSIONS

The experimental results from the distributed fiber optic sensors are presented and discussed below.

5.4.1. Representative Measurements from PPP-BOTDA. The Brillouin gain spectrum (BGS) of every sampling point of a distributed sensor was obtained. Figure 5.3 shows the evolution of a BGS at the center point, where the thermocouple was deployed, as the temperature is increased from 22 °C to 800 °C. Each BGS has a dominant peak corresponding to the Brillouin frequency, which can be located using a Lorentz curve fitting (Bao and Chen 2011). As temperature increases, the Brillouin gain bandwidth is slightly reduced, making it easier to identify the Brillouin frequency. The peak intensity of Brillouin gain spectrum increased and the Brillouin frequency is shifted from 10.83 GHz to 11.48 GHz over a temperature range of 22 °C to 800 °C.

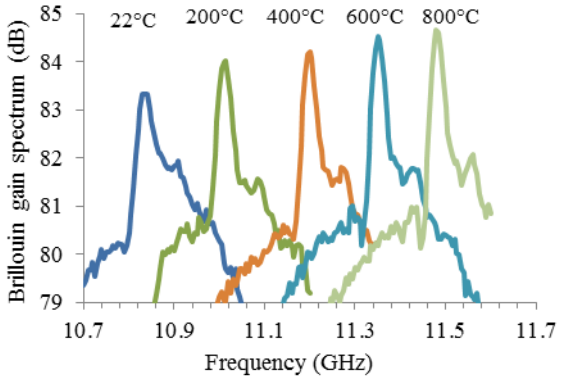

Figure 5.3. Brillouin spectrum shift due to temperature change

Figure 5.4 shows the measured Brillouin frequency along the length of a representative sensor for eight cases: two temperatures (22 °C and 300 °C) and four strains (0 με, 968 με, 1935 με, and 2903 με). The distance along the distributed sensor was measured from the pumping connector of the Neubrescope. It can be correlated well with the locations of the test setup. For example, H-G (5.96 m to 6.26 m), A-G (6.80 m to 7.02 m) and H-F (7.32 m to 7.42 m), and G-H (7.02 m to 7.32 m) correspond to the fiber lengths under heating only, tension only, and heating and tension combined, respectively.

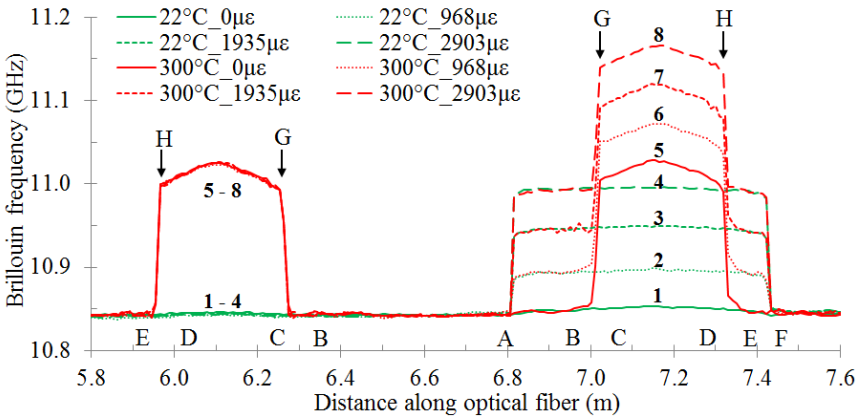

Figure 5.4. Brillouin frequency distributions

The eight curves designated by 1 to 8 in Figure 5.4 can be divided into two groups. At 22 °C, Curves 1 to 4 represent the Brillouin frequency distributions corresponding to 0 με, 968 με, 1935 με, and 2903 με, respectively. At 300 °C, Curves 5 to 8 represent the Brillouin frequency distributions corresponding to 0 με, 968 με, 1935

με, and 2903 με, respectively. The difference in Brillouin frequency between Curves 1 and 5 is the same as that between Curves 2 and 6, Curves 3 and 7, or Curves 4 and 8, since thermal effect remains the same. Another observation from Curves 5 to 8 is that the Brillouin frequencies are not constant over H-G or G-H, due to the non-uniform temperature distribution within the furnace. The temperature was the highest at the center of the heating tube, and it approximately decreased linearly outward due to the heat transfer effect. The temperature at G or H was approximately 85% to 95% of the highest temperature at the center.

5.4.2. Influence of Temperature on Strain Distribution. Figure 5.5 shows some representative results of the Brillouin frequency shift due to various elongations provided by the translation stage (or applied strains) after temperature compensation at 700 ºC. Non-uniform strain distributions were observed, and the fiber length G-H, which was under high temperatures, was subjected to lower strains than other portions under room temperature. This was mainly because the elastic modulus of the fused silica fiber was dependent on temperature. In the literature, Young's modulus of fused silica was found to increase from 72.5 GPa to 80.0 GPa as temperature was changed from 22 °C to 800 °C.

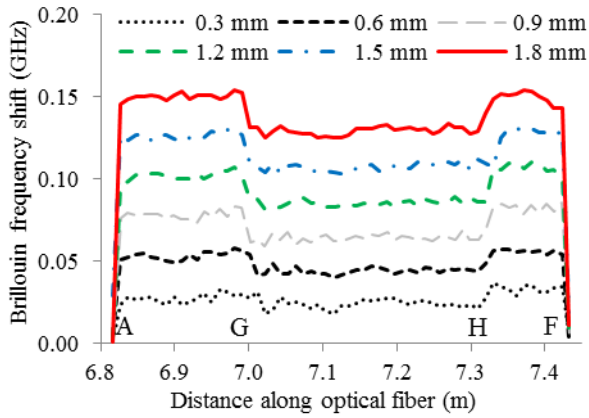

Figure 5.5. Brillouin frequency shifts for different elongations at 700 ºC

5.4.3. Temperature-Dependent Young's Modulus. Figure 5.6 shows the Young's modulus as a function of temperature up to 700 °C, which was determined from equation (5) and Young's modulus (E_0 = 72.5 GPa) at room temperature, based on the non-uniform strain distributions such as those in Figure 5.5.

At each temperature, the error bar represents plus and minus one standard deviation of 10 sensor measurements. Overall, the determined Young's moduli were in agreement with the reported results. The discrepancy was likely due to: (i) different strain distributions used, and (ii) temperature variation over time. The Young's modulus approximately increased linearly with temperature in the range of 22–700 °C, and the slope was determined to be 0.0133 GPa/°C. So, the correction factor can be written as:

$$\phi(T) = E(T) / E_0 = 1 + 0.0133(T - 22) / 72.5 \tag{5.8}$$

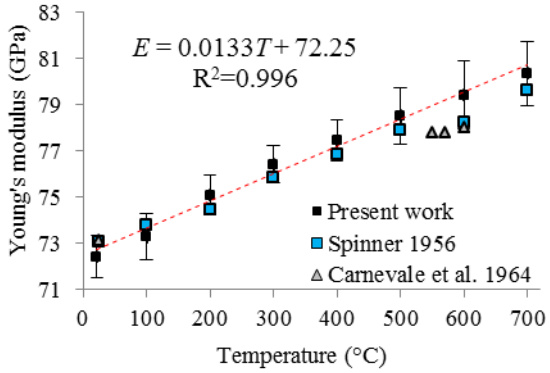

Figure 5.6. Temperature-dependent Young's modulus of fused silica fiber

5.4.4. Sensitivity of Load-Induced Strain to Temperature Distribution.

Equation (10) was used to determine the strain at the middle of ceramic tube ($x=l_2/2$), as presented in Figure 5.7, when ΔL=1.260 mm, l_1=206 mm, l_2=308 mm, and l_3=102 mm.

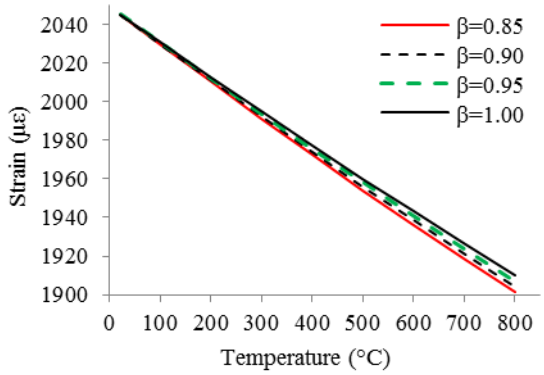

Figure 5.7. Effect of temperature distribution on the applied strain of optical fiber

The temperature ranged from 22 °C to 800 °C, and β changed from 0.85 to 1.00. Within the considered ranges of temperature and β, the influence of β was found to be less than 1%, while the influence of the temperature was approximately 7%. Therefore, the temperature along the furnace can be considered uniform for the calculation of strains, and the maximum temperature can be used to calculate the Young's modulus and the applied strains. In addition, as the temperature increased, the mechanical strain was reduced due to increased Young's modulus as indicated in Figure 5.6.

5.4.5. Strain Sensitivity Coefficient. The elongation of an optical fiber was divided by its original length to evaluate the tensile strain applied on the fiber optic sensor. The Brillouin frequency associated with the strain was measured for each temperature at the furnace center.

Figure 5.8 shows the frequency-strain curves at various temperatures after non-uniform strain distribution has been taken into account. It can be observed from Figure 5.8 that the Brillouin frequency linearly increases with strain at temperatures up to 800 °C. The slope of each frequency-strain curve or strain sensitivity coefficient at each temperature can be determined by linear regression. However, when the temperature exceeds 800 °C, the linear relationship is no longer retained, especially at large strains. This is likely because creep becomes significant at temperatures above 800 °C. When the total deformation remains unchanged, the elongation due to creep can reduce the load-induced strain applied to the fiber, and thus, compromise the sensing performance of the sensor. The creep effect is time-dependent and associated with temperature and strain.

The strain sensitivity coefficient is plotted in Figure 5.9 as a function of temperature for 10 sensors. It approximately decreased linearly with temperature over the range of 22°C to 700 °C and can be well fitted into a linear equation with a coefficient of determination (R^2) of 0.957. However, the coefficient at 800 °C was suddenly increased, and the results from different samples became quite deviated. Therefore, the operation temperature of optical fiber as strain sensors should be below 800 °C. As shown in Figure 5.9, the relationship between strain coefficient and temperature can be expressed into:

$$C_{\varepsilon}(T) = -1.228\times10^{-5}T + 4.97\times10^{-2} \tag{5.9}$$

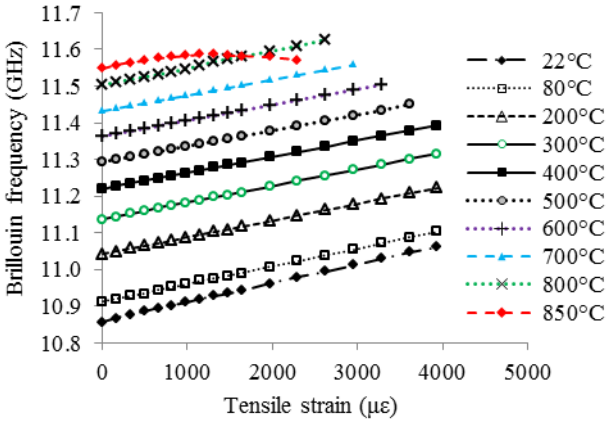

Figure 5.8. Brillouin frequency versus strain at different temperatures

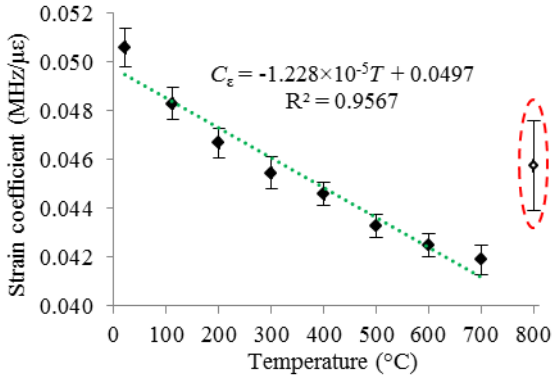

Figure 5.9. Temperature dependence of strain sensitivity coefficient

In this study, the confidence interval of strain measurements from 10 sensors was evaluated at 95% confidence level. The maximum value of the confidence intervals in the temperature range (22°C to 700 °C) of interest is defined as the precision of strain measurements. Similarly, the average of strain measurements from the 10 sensors was determined and compared with its true value obtained from the elongation via the translation stage. The maximum error between the average and true strains in the temperature range of interest is defined as the accuracy of strain measurements. The accuracy and precision of strain measurement were determined to be ±45 με and ±76 με, respectively, up to 700 °C. Its precision became approximately ±168 με at 800 °C.

5.4.6. Temperature Sensitivity Coefficient. The Brillouin frequency, which is associated with temperature change, was measured from a representative sensor and presented in Figure 5.10(a) at six strain levels. At each strain level, the Brillouin frequency increased with temperature up to 800 °C at a decreasing rate (slope).

At various strains, the frequency-temperature curves were approximately parallel, indicating little influence of strains on the temperature sensitivity. Since most calibration tests for temperature measurement were conducted under strain-free condition, the particular frequency-temperature relationship at zero strain in Figure 5.10(a) was fitted using a parabolic equation as represented by dash line in Figure 5.10(b), giving a temperature sensitivity of 1.113 MHz/°C at 22 °C and 0.830 MHz/°C at 800 °C. The parabolic regression equation accurately fitted into the test data as indicated by the efficient of correlation. In the form of Brillouin frequency shift from the room temperature (22 °C), the regression equation in Figure 5.10(b) can be rewritten as $\Delta\nu_B = (-3.464\times10^{-7}T + 1.110\times10^{-3})(T-22)$. In other words, the temperature sensitivity coefficient can be expressed into:

$$C_T(T) = -3.464\times10^{-7}T + 1.110\times10^{-3} \tag{5.10}$$

Figure 5.10(b) also shows a straight line to fit into the calibration data from room temperature to 200 °C. If a linear equation were to be used to extrapolate the higher temperature, the error in temperature prediction would be unacceptable. For example, the predicted temperature is underestimated by approximately 32 °C at 400 °C and 171 °C at 800 °C. As such, the parabolic equation must be used in calibration tests.

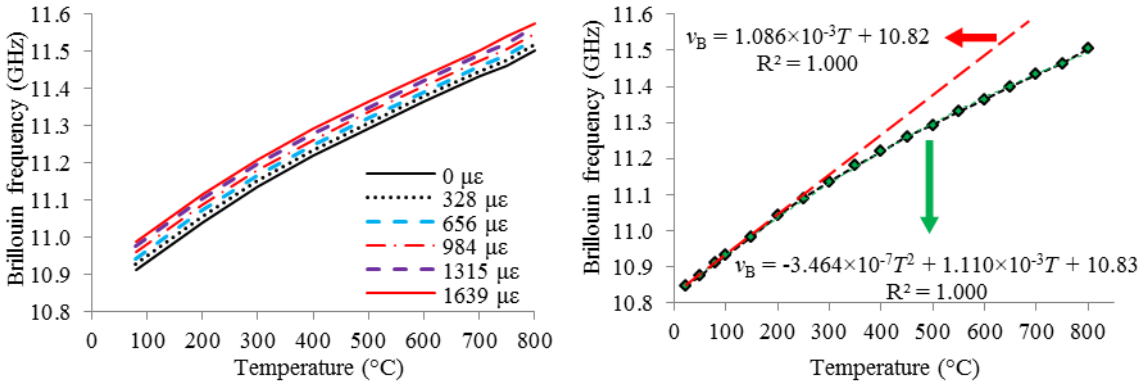

(a) Frequency-temperature curves (b) Regression analysis at zero strain

Figure 5.10. Brillouin frequency vs. temperature

The confidence interval of temperature measurements from 10 sensors was evaluated at 95% confidence level. The maximum value of the confidence intervals in the temperature range (22°C to 800 °C) of interest is defined as the precision of temperature

measurements. Similarly, the average of temperature measurements from the 10 sensors was determined and compared with its true value obtained from the thermocouple. The maximum error between the average and true temperatures in the temperature range of interest is defined as the accuracy of temperature measurements. The accuracy and precision were determined to be ±2.6 and ±5.5 °C, respectively.

Figure 5.11 shows the change of Brillouin frequency associated with temperature in three heating/cooling cycles under a strain-free condition. No significant discrepancy is observed among various cycles, indicating that no irreversible change occurs in heating or cooling. Thus, the distributed sensor can be used in cyclic heating-cooling conditions.

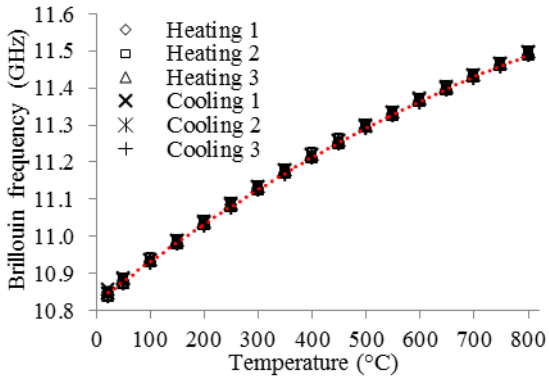

Figure 5.11. Brillouin frequency shift vs. temperature in three heating/cooling cycles

5.4.7. Temperature Dependence of Ultimate Strain. The tensile strength of fused silica fiber was reported to degrade at elevated temperatures. Considering that the Young's modulus increases with temperature, the ultimate strain, defined as the rupture strain, should decrease with temperature. The ultimate strain limits the strain measurement range of a distributed sensor. In this study, 10 fiber samples were heated at various sustained temperatures for 30 min, five of them were tensioned to rupture at the indicated temperature, and the other five were left in the furnace to cool down to room temperature naturally and were then tested to rupture. The tensile tests were conducted using the translation stage under displacement control at a rate of 0.5 mm/min.

Figure 5.12 shows the ultimate strains of optical fiber at various temperatures. The ultimate strain was reduced from 19,100 με to 6,000 με as the heating temperature was increased from 22 °C to 800 °C. The reduction is related to the chemo-mechanical

effects. At elevated temperatures, moisture at the fiber surface can react with the fused silica, which reduces the strength of Si-O covalent bond of the fiber. Such degradation can possibly be alleviated by using appropriate heat resistant coating that can isolate the surface moisture. In addition, the cooling process was found to further reduce the ultimate strain. This is likely because crystallization occurs in the slow cooling process, which makes the fiber more brittle and susceptible to small defects. Furthermore, the degradation is time-dependent as shown in Figure 5.13. Fibers were heated at 800 °C for different durations. Approximately 85% of degradation occurred within the first 20 min.

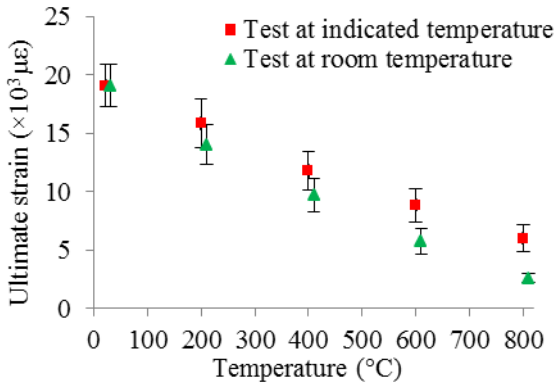

Figure 5.12. Temperature dependence of the ultimate strain

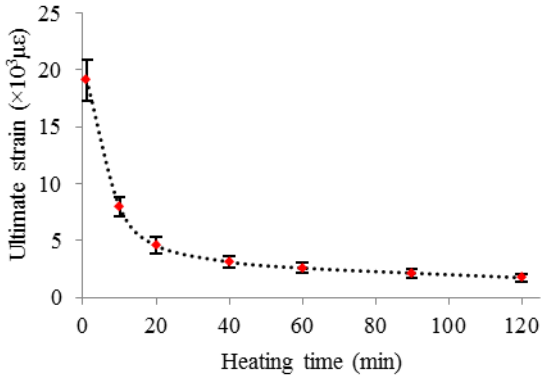

Figure 5.13. Influence of heating time on the ultimate strain at 800 °C

Figure 5.14 shows the SEM of a fiber that was heated at 800 °C for 3 hours. Local flakes were clearly present at a depth of approximately 1 μm to 3 μm, but no cracks were observed on the surface of the fiber. Therefore, the fiber sensor remained functional with degraded performance.

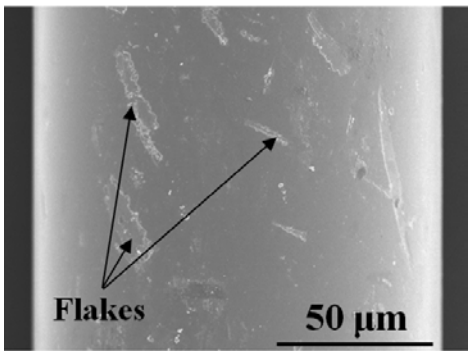

Figure 5.14. Influence of heating on surface microstructure of the fiber

5.5. SENSOR PACKAGING AND VALIDATION

In this section, the distributed sensor characterized in Section 5 is packaged for practical application. The calibration results are validated in an application setting.

5.5.1. Sensor Packaging. To protect it from environmental impact, a fiber optic sensor can be packaged and installed on a steel host. As illustrated in Figure 5.15(a), an optical fiber was passed through two aligned glass tubes with a small gap, and fixed at two far ends of the tubes with high temperature adhesives. Near the gap, each glass tube was fixed on the steel host using a clip that, once in place, could be clamped and tightened as appropriate. Away from the gap, the glass tube was restrained from lateral movement with a ring but allowed to slide longitudinally with negligible friction. The clip or ring was attached to the steel host by tightly inserting its square leg (1 mm × 1 mm) into a Φ1.4 mm circular hole pre-drilled on the steel host, as illustrated in Figure 5.15(a). The prototype of the sensor package is shown in Figure 5.15(b).

As indicated in Figure 5.15(a), each steel host was instrumented with two distributed fiber optic sensors, denoted as Sensor 1 and Sensor 2. They were closely spaced and connected at their ends to form one loop for each PPP-BOTDA measurement. Sensor 1 measured the Brillouin frequency shift due to the combined temperature and strain effects. Sensor 2 measured the Brillouin frequency shift due to temperature changes for compensation. Thus, the Brillouin frequency shift due to strain changes could be determined in Sensor 1. The thermal strain could then be determined from the calibrated sensitivity coefficients. The installation of a packaged Sensor 1 for strain measurement had a stand-off distance of 2.5 mm ± 0.5 mm from the surface of the steel.

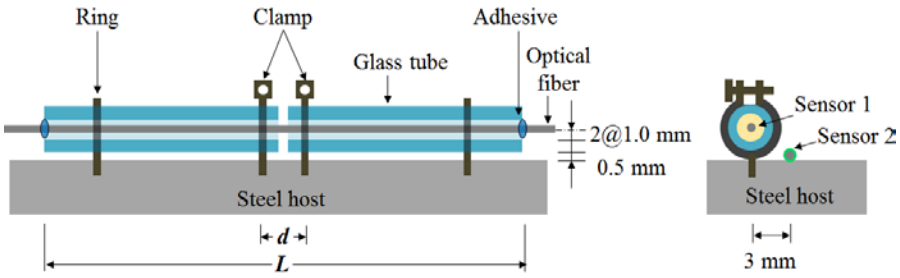

(a) Schematic view

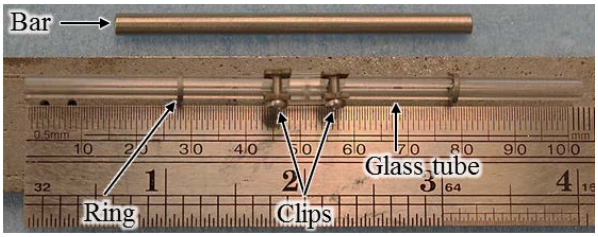

(b) Prototype

Figure 5.15. A designed distributed sensor

5.5.2. Strain Gauge Length Amplification. The center-to-center spacing between two clips, denoted by *d*, was referred to as gage length of the host structure. To enable large strain measurement, the change in spacing was averaged over an amplified gage length, denoted by *L* (>> *d*), of the fiber optic sensor, giving a gage length factor of $\alpha = L/d$. The use of amplified gage length can potentially lift the strain measurement limitation of a fiber optic sensor associated with its limited rupture strain. However, large α may result in reduced sensor sensitivity to C_ε/α. Thus, an appropriate factor must be determined for a specific application.

Figure 5.16 shows a four-dimensional plot of strain measurement range, sensitivity, temperature, and α value. The two horizontal axes represent the temperature and α value, respectively. The vertical axis represents the strain measurement range, and the color bar indicates the strain sensitivity. The theoretical relationship in Figure 5.16 can potentially aid in sensor package design in applications.

However, the nominal factor of $\alpha=L/d$ may not be achieved in application due to the elasticity of adhesives and the mechanical connections between various parts of each strain sensor. To validate the gage length amplification mechanism, a 600 mm × 25.4 mm × 5 mm (length × width × thickness) steel plate was tested in tension as indicated in Figure 5.17. The steel plate was instrumented with a strain sensor, as depicted in Figure

5.15, on one side and a crack gage on the other side for comparison. The crack gage was clipped on two 1.6-mm-thick steel sheets, each fixed on the steel plate with a screw of 1.5 mm in diameter. The center-to-center distance between the two screws was 150 mm. The crack gage measured the change in distance between its two tips and, due to negligible deformation in steel sheets, thus the deformation in steel plate between the two screws. The strain in steel plate can then be determined by dividing the crack gage reading by the distance between the two screws. The experimental α value was then calculated by dividing the strain in steel plate by the strain measured from the strain sensor.

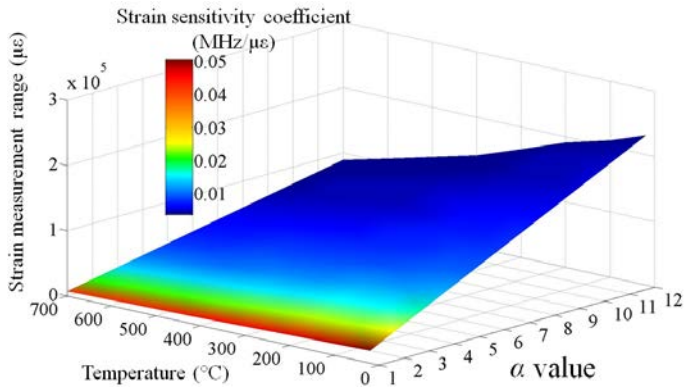

Figure 5.16. Strain measurement range and sensitivity versus temperature and α

In this study, L was set to 100 mm, and d was approximately 10 mm, 16 mm, 25 mm, and 50 mm, which corresponded to nominal α = 10, 6.25, 4, and 2, respectively. In each test case, exact L and d values were measured using a micrometer. In determination of L, adhesive within the glass tubes as shown in Figure 5.15 was considered to be 1 mm. Figure 5.18 shows a plot of nominal (α_{nom}) versus experimental (α_{exp}) gage length factor and its regression line. For each nominal α value, three samples were tested but their actual values slightly varied due to different measured L and d values. As shown in Figure 5.18, the regression line fitted into the test data very well with the coefficient of determination of 0.998. In the test range of α_{nom} = 2 to 10, the ratio of experimental and nominal α values is 0.90. It is observed from Figure 5.18 that the larger the nominal α value, the more significant the data variation becomes. This is likely because the relative error increases when a smaller d corresponding to the larger α value is measured.

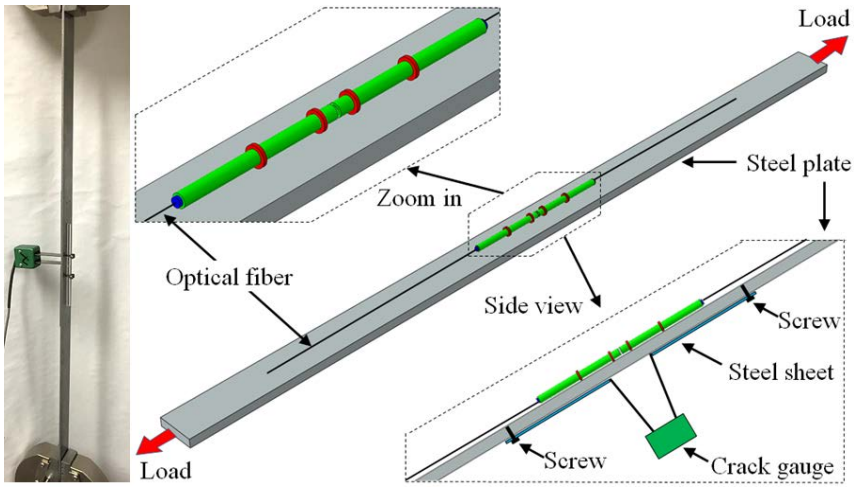

Figure 5.17. Tensile test specimen and instrumentation

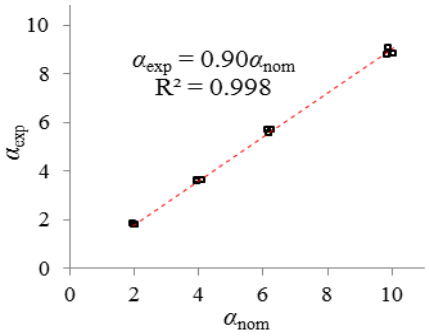

Figure 5.18. Comparison of experimental and nominal α values

5.5.3. Sensor Validation. To validate the strain sensitivity coefficient, two steel plates measuring 76 mm in length, 30 mm in width, and 6.3 mm in thickness were tested in the furnace from 22 °C to 700 °C. Each steel plate was instrumented with the packaged fiber optic strain sensors with a nominal α value of 11, as depicted in Figure 5.15, potentially providing a strain measurement range of up to 60,000 με (6%) at 800 °C. The sensors were applied to measure the steel's thermal strain at elevated temperatures. Each temperature level was sustained for about 5 min to ensure a stable temperature before five sequential measurements of Brillouin frequency distribution from the sensor. On the other hand, the same steel's thermal strain was measured using a dilatometer in a nitrogen atmosphere to prevent the steel from oxidation.

Figure 5.19 shows the mean values and standard deviations of 10 strain measurements from five measurements per plate specimen for two specimens. The thermal strain was found to increase approximately linearly with temperature up to 700

°C. Overall, the measurements from the fiber optic sensors agree well with the results from the dilatometer, with a discrepancy less than 5% at 95% confidence level.

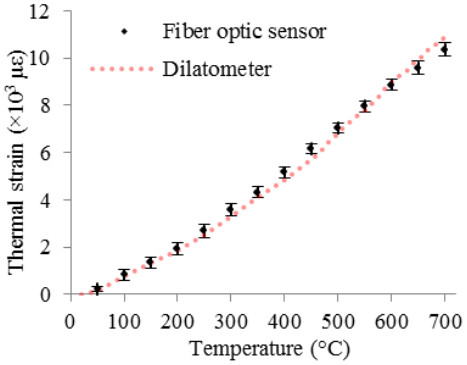

Figure 5.19. Comparison of measured thermal strains from fiber optic sensors and dilatometer in three steel plates

5.6. THERMAL ANNEALING TREATMENT

Annealing is a heat treatment that leads to changes in density and refractive index, and relieves in residual stresses and defects induced during manufacturing of a material. Fused silica consists of irregular tetrahedral network of Si-O covalent bonds with various strengths. When heated at high temperature, relatively weak bonds in fused silica are broken due to absorbed energy and stronger bonds are formed.

In previous studies, annealing was used to repair defects in fused silica at temperatures exceeding the softening point (1032 ºC), and treat fused silica sensors with inscribed gratings or cavity, for instance, FBG and interferometer sensors for enhanced thermal stability and operation range, by releasing the frozen-in, residual stresses in fused silica optical fiber. However, annealing can adversely affect the FBG sensors. In the conventional FBG sensors, the gratings inscribed on an SMF by ultraviolet irradiation may become less sensitive to the applied strain and temperature when the frozen-in stresses induced during the fabrication are partially released at a temperature of 200 ºC to 300 ºC. The gratings can be completely erased at a temperature of 600 ºC to 700 ºC. Unlike the grating and interferometer sensors, fused silica SMFs can be directly used as fully-distributed fiber optic sensors based on Brillouin scattering, with no dependence on inscribed gratings or cavity, and therefore, the distributed sensors can potentially be operated at higher temperatures. Temperature distributions measured from fully-

distributed fiber optic sensors allow condition monitoring of structures such as buildings, tunnels, and oil pipelines subjected to fire hazards and explosions due to natural or man-made events. A fused silica SMF with side-holes was characterized with BOTDA at temperatures up to 1000 ºC, and a linear relationship between the Brillouin frequency and temperature was reported. Nonlinear relationships were demonstrated by other investigators using fused silica SMFs without side-holes. Annealing was performed to allow measurements of temperature up to 850 ºC. However, operations at higher temperatures have not been fully explored. This study aims to characterize a fused silica SMF for high-temperature measurement based on PPP-BOTDA. The SMF had an 8.2-μm-diameter core and a 125-μm-diameter cladding. The temperature-dependent sensitivity coefficients of the sensor were experimentally calibrated. Emphasis was placed on the effect of annealing on the operating temperature, measurement discrepancy, and sensitivity of the sensor.

As illustrated in Figure 5.20 the distributed sensor, free of mechanical strain, was passed through a temperature controlled furnace and connected to a Neubrescope data acquisition system (Model NBX-7020). The furnace consisted of a steel case (A-D), heat insulation fabrics (A-B, C-D), a 200-mm heating coil wrapped ceramic tube (B-C) in the middle, and an electric thermocouple deployed at the center of the ceramic tube. The temperature was monitored with an accuracy of ±0.5 °C up to 1000 ºC. Throughout the experiment, the sensor portion B-C inside the ceramic tube was heated in a controlled fashion; another two portions E-B and C-F were affected by heat transfer.

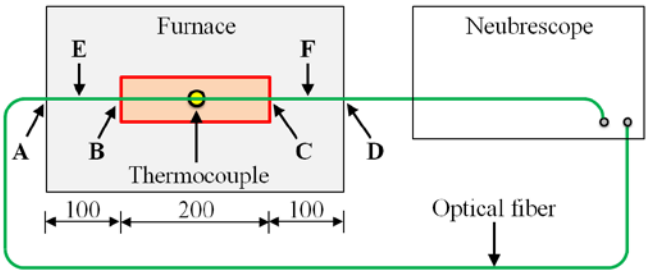

Figure 5.20. Experimental setup (unit: mm)

Spatially-distributed BGS was measured along the length of a tested SMF, from which the Brillouin frequency was determined using a Lorentz curve fitting algorithm.

Figure 5.21 shows the Brillouin frequency distributions along the optical fiber, corresponding to six heating temperatures. The Brillouin frequency increased with the heating temperature and was the highest in the middle portion B-C and gradually decreases outward until points E and F at the ends of heat transfer.

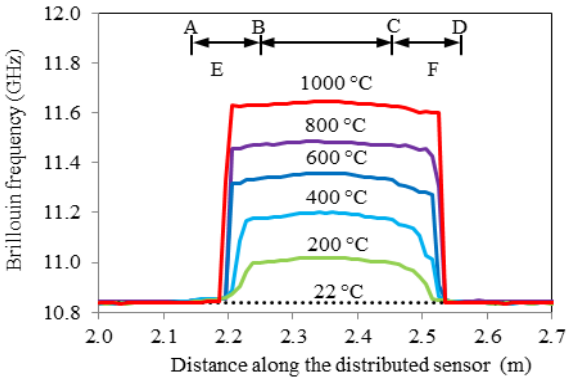

Figure 5.21. Representative spatial distributions of Brillouin frequency

Figure 5.22 shows a representative annealing protocol of temperature measured over time by the thermocouple (continuous line), where R^2 represents the coefficient of determination. The test was completed in three stages: linearly heating a fiber from 22 ºC to 1000 ºC in 229 min ± 2 min (heating stage), maintaining a temperature at 1000 ºC for 240 min ± 2 min (sustained stage), and naturally cooling it to 22 ºC (cooling stage). The naturally cooling process can be well represented by an exponentially decayed curve as indicated. In the heating stage, the Brillouin frequency was measured by the fiber optic sensor while the applied temperature was held at 22 ºC, 50 ºC to 800 ºC at 50 ºC interval, and 825 ºC to 1000 ºC at 25 ºC interval. In the cooling stage, the Brillouin frequency was measured at the same temperatures indicated by the thermocouple as the temperature continued to drop naturally. Each PPP-BOTDA measurement was completed in 1 min to 2 min, which was taken into account in the temperature protocol. The measured frequency (line with triangles) is also plotted as a function of time.

As summarized in Table 5.1, three protocols were considered with a heating rate and sustained duration of (1): 30.6 ºC/min and 120 min, (2): 4.3 ºC/min and 120 min, and (3): 4.3 ºC/min and 240 min, respectively. The two heating rates represent ‘fast’ and ‘slow’ heating processes, respectively. The effect of sustained duration at different

temperatures is discussed afterwards in this study. For each protocol, a new fiber optic sensor was tested. However, all the test fibers were from the same SMF as specified before. Figure 5.22 indicates the Brillouin frequency increases with a slightly decreasing rate as the temperature was linearly increased at a constant rate.

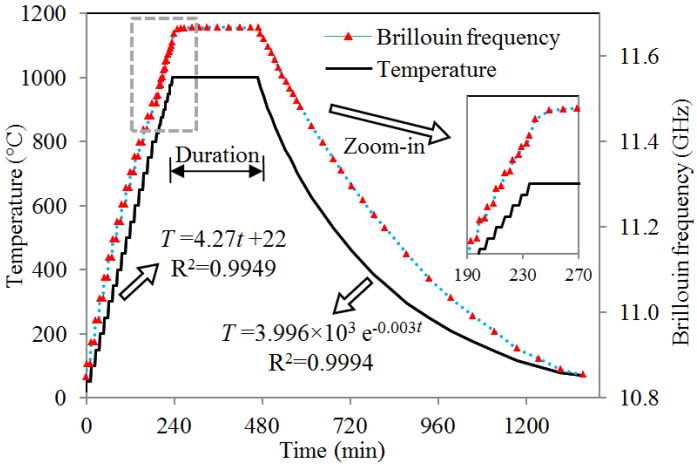

Figure 5.22. Temperature protocol (3) and its corresponding frequency time function. The temperature and time are respectively denoted by T and t

Table 5.1. Annealing test protocols

Test number	Heating rate (°C/min)	Duration (min)	Cooling method
1	30.6	120	Natural cooling
2	4.3	120	Natural cooling
3	4.3	240	Natural cooling

To establish their nonlinear relationship, the Brillouin frequency and its corresponding temperature are plotted in Figure 5.23(a). ‘Unannealed 1’, ‘Unannealed 2’, and ‘Unannealed 3’ represent the heating processes of protocols (1), (2), and (3), respectively. ‘Annealed 1’ and ‘Annealed 2’ represent the cooling processes corresponding to ‘Unannealed 1’ and ‘Unannealed 2’, respectively, after 120 min tests at 1000 ºC. ‘Annealed 3’ corresponds to ‘Unannealed 3’ after 240 min tests at 1000 ºC. When the temperature was increased from 22 ºC to 800 ºC, the Brillouin frequencies corresponding to the three temperature protocols increased from 10.85 GHz to 11.49 GHz

with the temperature sensitivity reduced from 1.086×10^{-3} GHz/ºC to 0.432×10^{-3} GHz/ºC. The three frequencies were in good agreement with a maximum discrepancy of less than 1%. Starting at approximately 850 ºC, the three Brillouin frequencies substantially deviated from their previous trend to higher values that were significantly different between the first two protocols and similar between the last two protocols as demonstrated from a zoom-in plot in Figure 5.23(b). This is mainly because the viscosity of the optical fiber was significantly reduced as the temperature went above 850 ºC, resulting in the relief of residual stresses. The higher the heating rate ('Unannealed 1') was, the slower the stress relief became. The change of stress status in the fiber further induced changes of physical properties such as refractive index that directly influenced the measured Brillouin frequency. Note that the insignificant difference in two frequencies at 1000 °C after the sustained stage of tests represented random error from the different sensors.

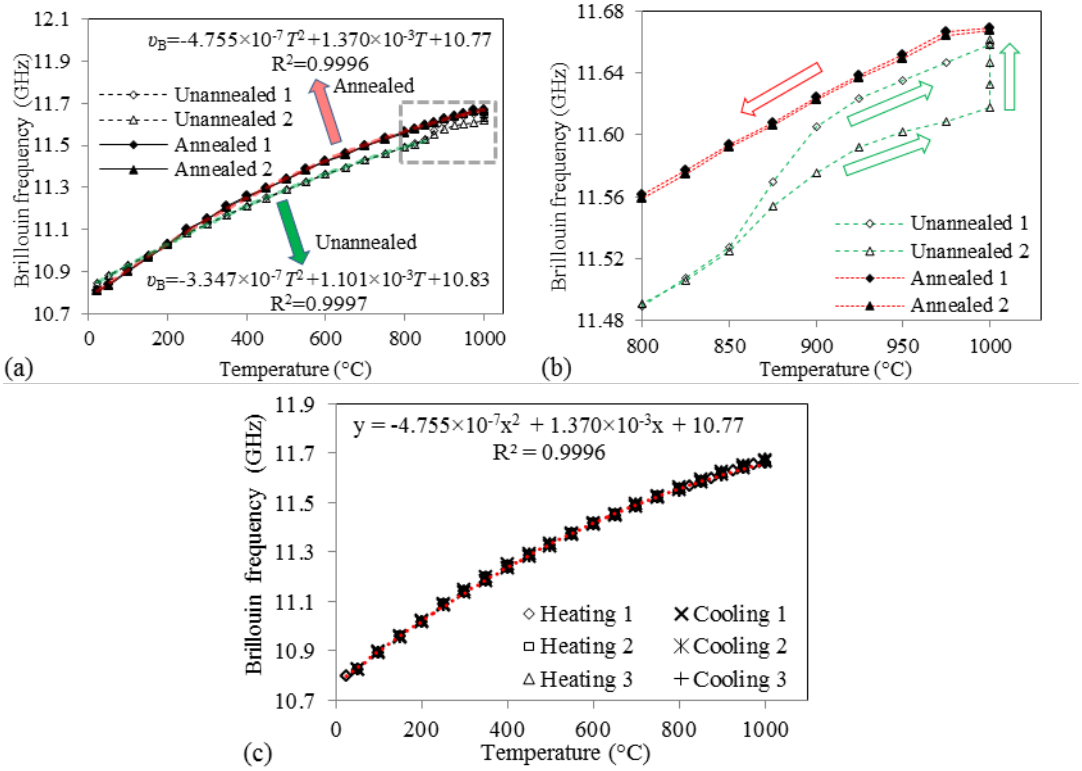

Figure 5.23. Brillouin frequency changes: (a) one cycle of 22–1000 °C before and after annealing; (b) one cycle of zoom-in 800–1000 °C before and after annealing; (c) three cycles of 22–1000 °C after annealing. The Brillouin frequency is denoted by υ_B

After the heat treatment up to 1000 ºC, the optical fiber was kept in the furnace to naturally cool down to 22 ºC. The slow cooling operation prevented new residual stress being created. After annealing, the stable temperature measurement range was extended from 800 ºC to 1000 ºC, as shown in Figure 5.23(a) and (b). The measured Brillouin frequency and temperature can be fitted by a parabolic equation with $R^2 = 0.9996$. Due to annealing, the temperature sensitivity of the sensor was changed from $(1.086–0.432)\times10^{-3}$ GHz/ºC to $(1.349–0.419)\times10^{-3}$ GHz/ºC within a temperature range from 22 ºC to 1000 ºC. The test results corresponding to the first two protocols with different heating rates were in excellent agreement. The difference in Brillouin frequency at each temperature was nearly constant with no more than 1%. This deviation can be further minimized by increasing the duration time at the sustained temperature such as the third protocol. To verify the annealing effect, the annealed sensor following the third temperature protocol was tested again in three heating-cooling cycles at 22 ºC and 50 ºC to 1000 ºC at 50 ºC interval. As shown in Figure 5.23(c), no notable difference can be observed among the six calibration curves between the measured Brillouin frequency and the applied temperature. The maximum difference in Brillouin frequency is ±0.009 GHz in the range of temperature tested.

In the sustained stage at 1000 ºC, as shown in Figure 5.24(a), the Brillouin frequency slightly increased in the first hour with a decreasing rate and then became stabilized. The frequency increase over time mainly resulted from the alleviation of the frozen-in stresses as the viscosity of the fiber was reduced. Diffusion of germanium (Ge) dopant from core to cladding likely occurred as well at high temperature. However, since the Ge diffusion from core leads to reduction in the core's effective refractive index, which in turn leads to reduction in Brillouin frequency, dopant diffusion was considered a minor effect.

The time-dependent behavior demonstrated the transient nature of annealing process. To characterize the transient behavior of annealing, Figure 5.24(a) shows six stabilization curves corresponding to constant temperatures of 750 ºC, 800 ºC, 850 ºC, 900 ºC, 950 ºC, and 1000 ºC, respectively. Figure 5.24(b) shows the time required to make the optical fiber stabilized. The optical fiber was considered stabilized when the Brillouin frequency's increasing rate (slope of the Brillouin frequency vs. time curve)

became less than 2% of the initial increasing rate. The stabilization time exponentially decreases with annealing temperature, because of the temperature-dependence of viscosity. This is in agreement with the study on annealing defects in fused silica using CO_2 laser. As the temperature increases, the annealing can be completed more quickly.

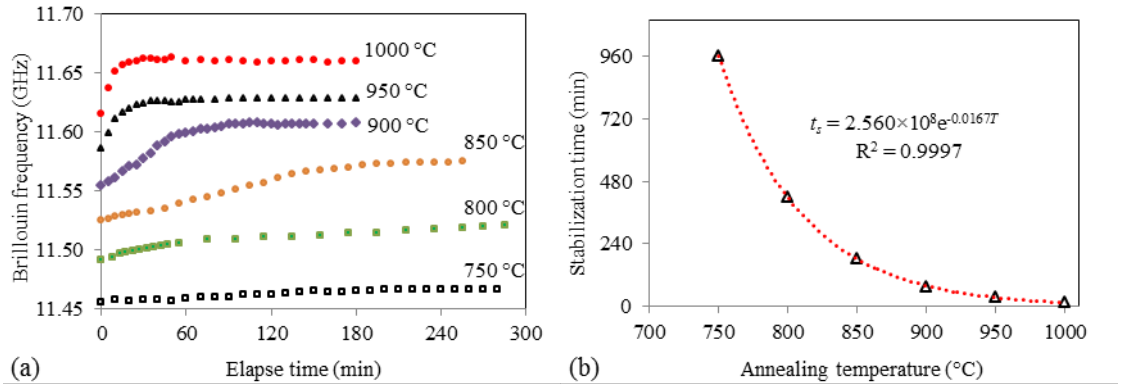

Figure 5.24. Time-dependent stabilization curves at sustained temperatures: (a) change of Brillouin frequency over time; (b) relationship between annealing temperature and the required time (t_s) for stabilization

Influence on mechanical properties and potential side effects associated with high-temperature treatment were reported in the literature. When Ge-doped fibers were heated above 1000 ºC, dopant diffusion and crystallization could be promoted, increasing scattering loss of light signal. In our experiments, no significant signal loss due to the annealing was observed after the treatment at or below 1000 ºC. However, the heat treatment reduced the fiber's mechanical strength, possibly due to the reaction between moisture and fused silica at the fiber's surface. Appropriate protective coating could be applied to enhance the mechanical performance. For instance, a dual-layer coating of a copper inner layer and a low phosphorous nickel outer layer was proposed to extend the thermal durability of silica optical fibers.

5.7. SUMMARY

Based on the above investigations, the following summaries can be drawn:

The Brillouin frequency of distributed fiber optic sensors increased quadratically with temperature. The frequency-temperature sensitivity coefficient linearly decreased from 1.113 MHz/°C to 0.830 MHz/°C in the range of 22 °C to 800 °C. The measurement

accuracy and precision were ±2.6 °C and ±5.5 °C, respectively. The Brillouin frequency of the sensors increased linearly with strain. The frequency-strain sensitivity coefficient linearly decreased from 0.054 MHz/με to 0.042 MHz/με in the range of 22 °C to 700 °C. The measurement accuracy and precision were ±45 and ±76 με, respectively. At 800 °C, creep became significant, thus reducing the strain sensing precision. The sensors were stable up to 800 °C in heating-cooling cycles or continuous heating processes.

The Young's modulus of optical fiber increased linearly from 73 GPa to 80 GPa in the range of 22 °C to 700 °C. The ultimate strain decreased from 19,100 με to 6,000 με in the range of 22°C to 800 °C due to chemo-mechanical effect. Approximately 85% of the strain reduction occurred within the first 20 min of heating. Load tests indicated 90% efficiency of the gage length amplification mechanism in application setting. Therefore, a packaged strain sensor with a nominal amplification factor of 11 can potentially increase the measurement range by approximately 10 times of a corresponding bare fiber or from 6,000 με to 60,000 με at 800 °C. Indeed, the packaged sensor was successfully applied to measure the thermal strain of steel up to 10,500 με at 700 °C, which was validated by a commercial dilatometer.

6. TEMPERATURE MEASUREMENT AND DAMAGE DETECTION IN CONCRETE BEAMS EXPOSED TO FIRE

6.1. BACKGROUND

The load bearing capacity and integrity of concrete structures can degrade significantly during a fire due to degraded material properties and spalling associated with high temperatures. The remaining capacity of a structure can be more reliably evaluated through thermo-mechanical analysis when temperature distributions within structural members are known *in situ*. The current state of practice in experimental structural fire analysis is to measure local temperatures on the surface or inside of concrete members using thermocouples (or calculate surface temperatures from measured heat fluxes), and then estimate the temperature distributions within the concrete structures. While thermocouples can be deployed to measure temperatures at numerous locations, the required wiring is costly and time consuming – particularly in large-scale structures. More importantly, measurements from thermocouples can be adversely affected by electromagnetic interference, moisture, and unanticipated junctions.

In this study, four small-scale reinforced concrete beams were tested in a natural gas fueled compartment fire in the National Fire Research Laboratory at National Institute of Standards and Technology (NIST). Each beam was instrumented with a distributed fiber optic sensor and four thermocouples and exposed to fires of increasing intensity until extensive spalling of the concrete occurred. The thermocouples were used to validate the distributed sensor at the locations of the thermocouples.

6.2. EXPERIMENTAL PROGRAM

The details of the experimental program is introduced as below.

6.2.1. Test Setup. Each concrete beam was tested in the compartment fire setup shown in Figure 6.1. The setup, which was located under a 6 m × 6 m exhaust hood, consisted of a burner rack, an enclosure, and water-cooled supports for the beam specimen. The rack supported four independent natural gas diffusion burners made of sheet metal, each with dimensions of 300 mm × 300 mm × 140 mm (length × width × height). The two middle burners were fueled with natural gas from their bottom through the burner cavity and a 20 mm thick ceramic fiber blanket for gas distribution.

The burners were manually regulated using a needle valve on the gas line, and the energy content of the supplied gas was measured with an uncertainty of less than 2.4 %. An enclosure constructed of steel square tubes, cold-formed steel C-channels, and gypsum boards lined with refractory fiber board formed the fire test space above the burner rack. The enclosure was open at the bottom and the two end faces in the longitudinal direction of the beam, creating the compartment flame dynamics. The heated area created by the enclosure had dimensions of 380 mm × 400 mm × 1830 mm (height × width × length), in which the entire beam was engulfed in flame.

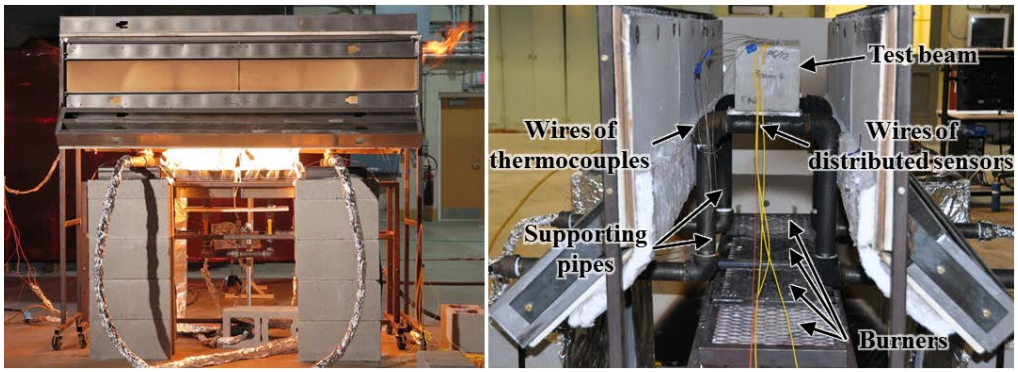

Figure 6.1. Test setup of concrete beams in fire

The test beams were simply supported at a clear span of 0.5 m on two supports constructed from 1-1/2” Schedule 40 pipe (outer diameter: 48 mm), which were, in turn, supported on concrete blocks. The only mechanical load on the beam was its self-weight. The supporting pipes were water-cooled so that the exiting water temperature did not exceed 50 °C, which limited undesired thermally-induced movement of the supports.

6.2.2. Test Specimens and Instrumentation. Four concrete beams were tested, designated as Beam 1, Beam 2, Beam 3, and Beam 4 in Figure 6.2. Each beam was 152 mm deep, 152 mm wide, and 610 mm long. Normal weight concrete with nominal 28-day compressive strength of 42 MPa was used (concrete casting and curing are detailed in Section 3.3). A deformed steel reinforcing bar with 25.4 mm diameter was placed approximately in the center of each beam. The geometry of the beams was not intended to be representative of construction practice, but rather to provide simple specimen geometry to test the optical fibers.

Each test beam was instrumented with four, glass sheathed, K-type, bare-bead thermocouples, and one distributed fiber optic sensor. The four thermocouples (TC1, TC2, TC3, and TC4) were embedded within the beam at the quarter span and the mid-span as depicted in Figure 6.2. TC1 was at the quarter span at the 1/2 depth of the beam and near the rebar; TC2, TC3, and TC4 were at mid-span at the 1/4, 1/2, and 3/4 depth of the beam, respectively. Additional thermocouples were deployed on the inner wall of the compartment and throughout the test setup to characterize the test environment and monitor safety-relevant temperatures.

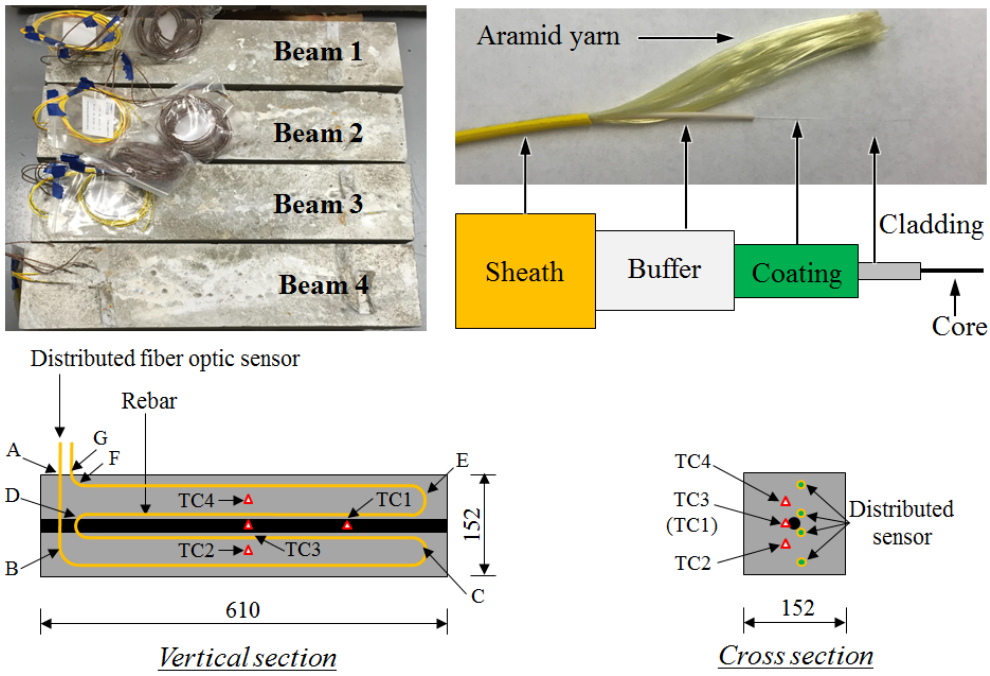

Figure 6.2. Test concrete beam specimens (unit: mm)

The optical fiber was loosely passed through a protective polymer sheath (diameter: 1 mm) and could freely slide within the sheath. The sheath had a thermal conductivity of 3.0 W/(m·K), which was slightly higher than the thermal conductivity of the concrete, which is typically less than 2.0 W/(m·K). The sheath was in direct contact with concrete and isolated the optical fiber from the effect of strain in concrete. Thus, the distributed sensor was subjected to temperature change only. It was deployed within the concrete following the path illustrated in Figure 6.2. Capital letters A to G designate key locations on the optical fiber. For example, A and G corresponded to the entrance and

exit points of the optical fiber with respect to concrete. The optical fiber was firmly attached on a fishing wire every 150 mm using superglue; and the fishing wire was tightly fixed at both ends to the walls of casting mold to keep the fiber straight during casting of the concrete.

Data from the fuel delivery system and thermocouples were measured continuously using a National Instruments data acquisition system (NI PXIe-1082). Thermocouple data were recorded using 24-Bit Thermocouple Input Modules (NI PXIe-4353). Data were sampled at 90 Hz with average values and standard deviations recorded in the output file at 1 Hz. The manufacturer-specified standard limit of error for the thermocouples is 2.2 °C or 0.75 % (whichever value is greater). This error represents a standard uncertainty of the thermocouple itself and does not account for possible additional sources of uncertainty, such as the data acquisition systems and calibration drifts during use. The Neubrescope data acquisition system was used to take Brillouin gain spectra from the distributed fiber optic sensors. Using a pulse length of 0.2 ns, 2 cm spatial resolution measurements are obtainable, and the accuracies for strain and temperature measurements were reported to be 15 με and 0.75 °C, respectively, at an average count of 2^{14}. In this study, the measurement distance and the spatial resolution were set at 50 m and 2 cm, respectively, meaning the Brillouin frequency shifts of two points spaced at no less than 2 cm could be distinguished over a 50 m fiber length. The scanning frequency ranged from 10.82 GHz to 11.50 GHz, which approximately corresponded to a target temperature range of 20 °C to 800 °C. The acquisition time varied from 15 seconds to 25 seconds, depending on the scanning frequency range.

6.2.3. Mix Design and Curing of Concrete. Type III Portland cement, Missouri river sands, and small aggregates (maximum grain size of 5 mm) at 640 kg/m^3, 800 kg/m^3, and 400 kg/m^3, respectively, were used. The water-to-cement ratio was 0.45 by mass. To improve the flowability of self-consolidated concrete, a polycarboxylic acid high-range water reducer was used at a dosage of 1% by volume of the water content. The initial slump flow was measured to be between 280 mm and 290 mm, ensuring that no vibration was required and optical fibers in the specimens would not be disturbed during casting. After concrete casting, the beams were trowel-finished and covered with wet burlap pieces and a plastic sheet for 1 day. The beams were then demolded and air-

cured for 36 days prior to testing. In the first 32 days, the beams were cured at a temperature of 25±3 °C and a relative humidity of 40±4 %. In the last four days before testing, the beams were exposed to a less controllable environment (transport and indoor space) where temperature was about 30±5 °C and humidity was about 30±10 %.

6.2.4. Fire Test Protocols. The four concrete beams were exposed to fire at increasing intensities under the control of burner heat release rate (HRR). Figure 6.3 shows the test protocols of the four beams. The HRR was held constant at each target level. The durations corresponding to each sustained HRR value for the four beams are listed in Table 6.1.

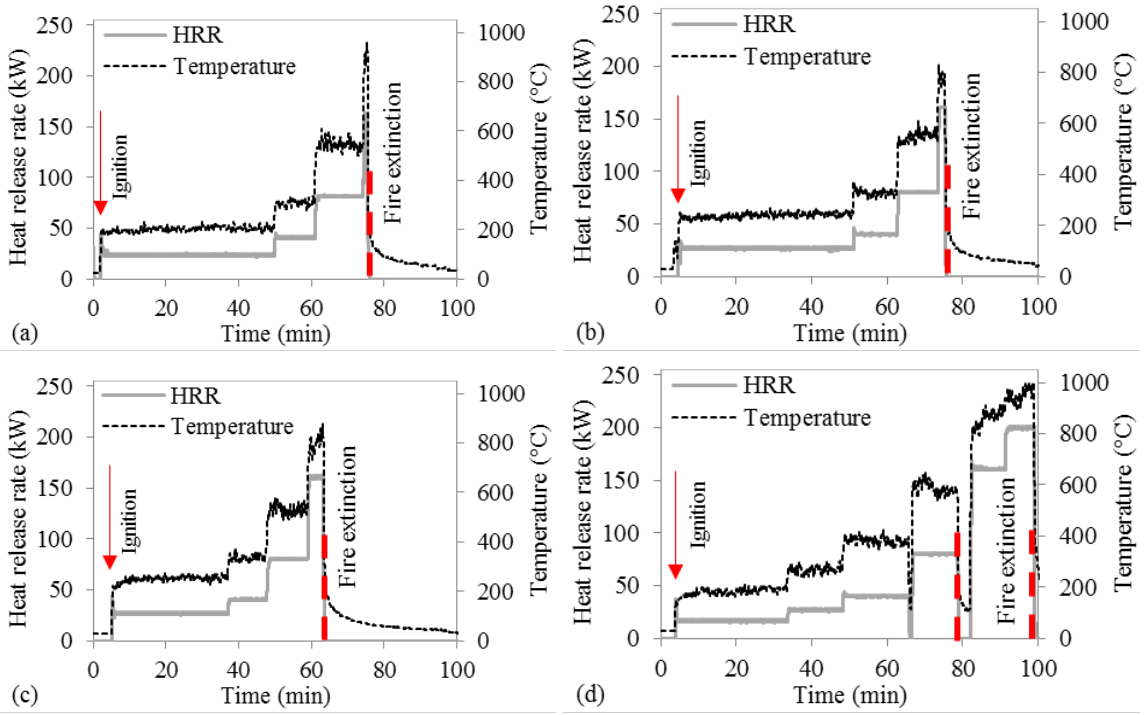

Figure 6.3. HRR and average compartment air temperature protocols for: (a) Beam 1; (b) Beam 2; (c) Beam 3; (d) Beam 4

A relatively longer duration was adopted at the first target level to more slowly heat the test beams, reduce the temperature gradient, and drive off some of the residual moisture near the surface. The intent was to delay spalling of the concrete, which tends to occur with a relatively high (> 10 % by weight) moisture content. Beam 1 and Beam 2 were tested with the same protocol. They were pre-heated at a HRR of 25 kW for 45

minutes, and, then, heated at each elevated HRR for 10 minutes. Beam 3 was heated at 25 kW for 30 minutes, which was 15 minutes less than that of Beam 1 and Beam 2, in order to shorten the test duration. For Beam 1 to Beam 3, fire was extinguished when excessive spalling occurred at a HRR of 160 kW for various time durations. Beam 4 was first heated for 30 minutes at 15 kW, which was 10 kW less than that of the other three beams. The fire was extinguished for 3 minutes between 40 kW and 80 kW to allow visual observation of Beam 4. Then, fire was re-ignited, and the HRR was increased from 160 kW to 200 kW until excessive spalling occurred.

Table 6.1. Durations corresponding to each sustained HRR value for four beams

HRR (kW)	Duration (minutes)			
	Beam 1	Beam 2	Beam 3	Beam 4
15	N/A	N/A	N/A	30
25	45	45	30	15
40	10	10	10	10
80	10	10	10	10
160	1	2	4	10
200	N/A	N/A	N/A	8

6.3. RESULTS AND DISCUSSION

The experimental results are presented as follows.

6.3.1. Physical Observations of Concrete Cracking and Spalling. As the temperature in Beam 4 increased, the concrete cracked and spalled as shown in Figure 6.4. Surface cracks were observed when the air temperature within the compartment reached about 300 °C. Cracking continued as the temperature increased and at 450 °C spalling occurred at the corners and edges of beam. Sudden fracture through the entire specimen happened shortly after the air temperature reached 800 °C to 1000 °C. Similar damage progressions were observed for each of the other beams. The mechanisms causing cracking and spalling of concrete at elevated temperatures are complicated and involve a series of physicochemical reactions and stresses induced by thermal gradients. It is noted that fracture behavior is governed by the temperature of the beam, not the surrounding air. The observed damage sequence was specific to the member geometry, material properties, conditions at the time of testing, and thermal loading protocols.

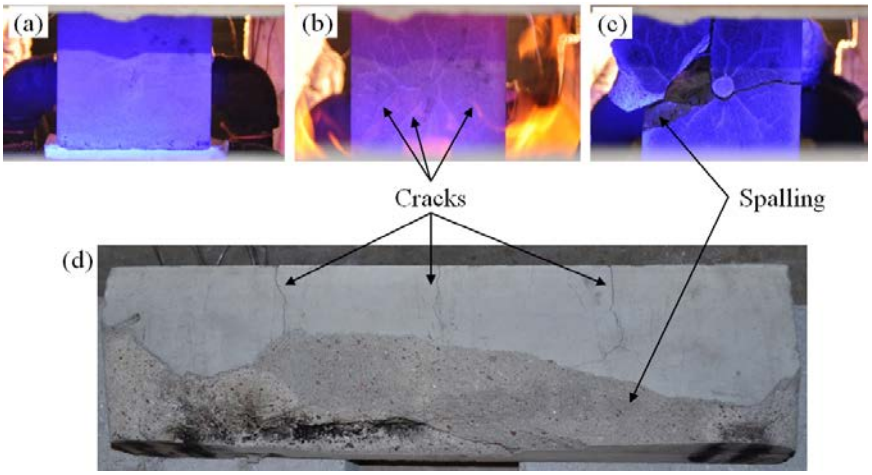

Figure 6.4. End and side views of Beam 4: (a) prior to ignition; (b) when engulfed in fire; (c) at the moment of fire extinction; (d) when cooled down to room temperature

Concrete cracking and spalling affect the heat transfer behavior of the beam as illustrated in Figure 6.5. Before cracks appear, the temperature of internal concrete increases mainly due to thermal conduction. Due to the low thermal conductivity of concrete, the temperature of the concrete away from the surface increases slowly. Once cracks appear, they can be filled with hot air. The internal concrete is then subjected to thermal radiation and convection along the crack, in addition to thermal conduction through the concrete cover. Therefore, the temperatures in the vicinity of cracks can increase more rapidly. Since the spatially-distributed sensors have greater chances to cross the cracks than discrete thermocouple beads, they are a potential method to monitor cracking within concrete.

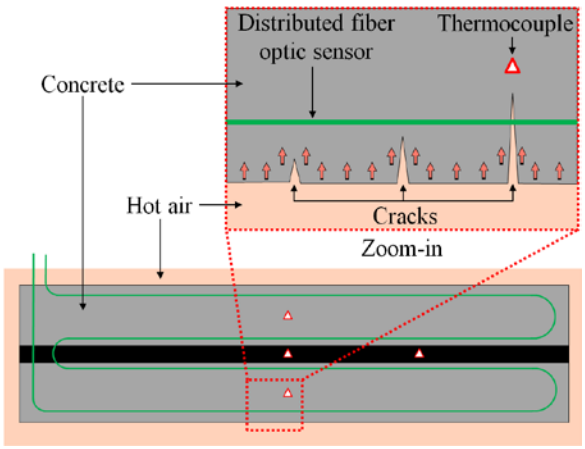

Figure 6.5. Heat transfer after concrete cracking

6.3.2. Temperature Histories. When the beams were subjected to fire, the temperature within the concrete gradually increased. At each HRR, the spatially-distributed Brillouin frequencies along the length of fiber optic sensor were measured and converted to temperatures using the calibration curve. Figure 6.6(a)–(d) show the temperature time histories in Beam 1 to Beam 4, respectively. The measurement results from the thermocouples and distributed fiber optic sensors were compared.

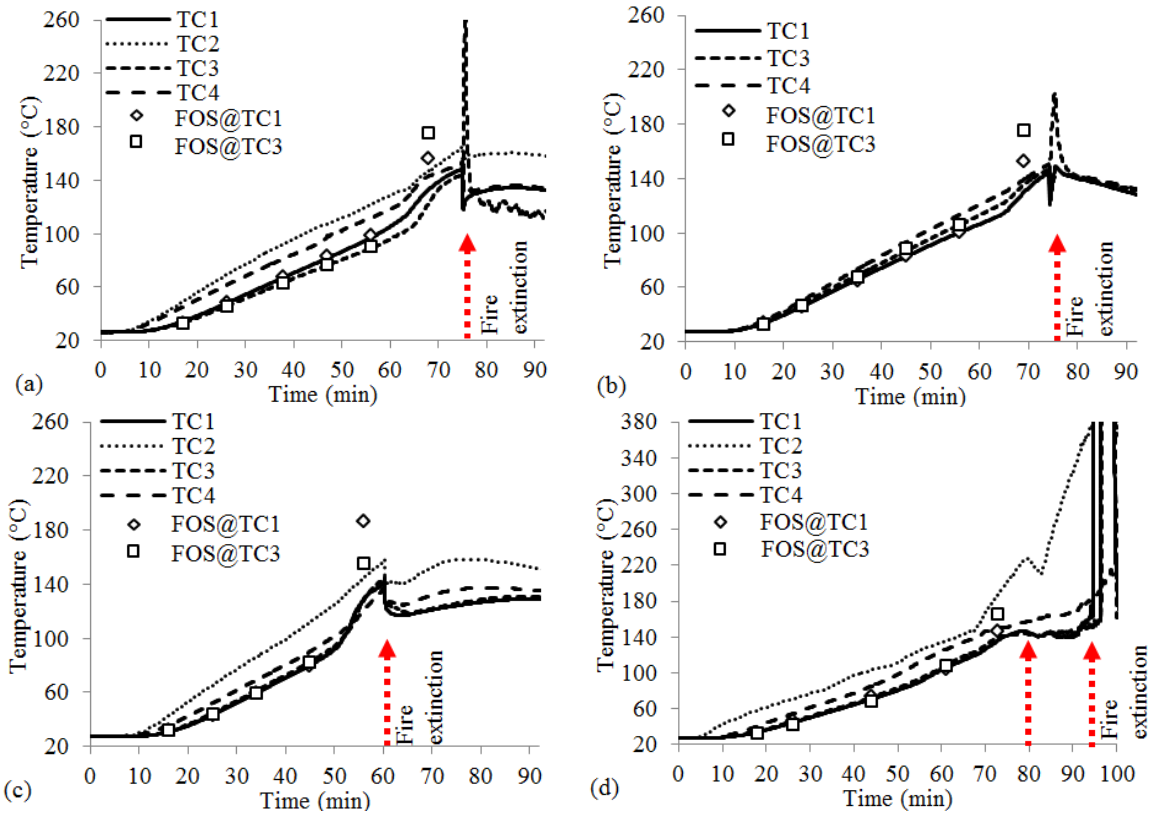

Figure 6.6. Temperature history in: (a) Beam 1; (b) Beam 2; (c) Beam 3; (d) Beam 4. "TC*n*" and "FOS@TC*n*" represent the measurements from the n^{th} thermocouple and a distributed sensor at the location of the n^{th} thermocouple

As expected, temperatures were typically highest at the bottom, mid-span of the beam (TC2) and lowest at the center of the beam (TC1 and TC3). At a HRR of 25 kW and 40 kW for Beam 1 to Beam 3 and at 15 kW to 40 kW for Beam 4, temperatures within the concrete increased almost linearly with time and the maximum discrepancy between the measurements from the thermocouples and fiber optic sensors was 8.8 %. However, at a HRR of 80 kW for Beam 1 to Beam 4, temperatures increased at higher

rates over time and the discrepancies between the measurements were increased up to 53.7 %. As discussed in the next section, these larger discrepancies are believed to be due to the influence of concrete cracking or spalling on the heat transfer. Indeed, the spikes in the thermocouple measurements immediately prior to fire extinction were due to exposure of the thermocouple beads to heated air after spalling.

6.3.3. Temperature Distributions. Figures 6.7(a)–(d) present temperature distributions in the four beams, measured from the distributed fiber optic sensors. The horizontal axis represents the distance along the distributed fiber optic sensor, starting from the pump end of the Neubrescope. The vertical axis represents temperature. The location of the distributed fiber optic sensor within the test beam was marked using capital letters from A to G. The length between A and G was embedded within concrete. The other portions of the fiber were exposed to air, and, in particular, the part of the fiber length within the compartment was subjected to heated air.

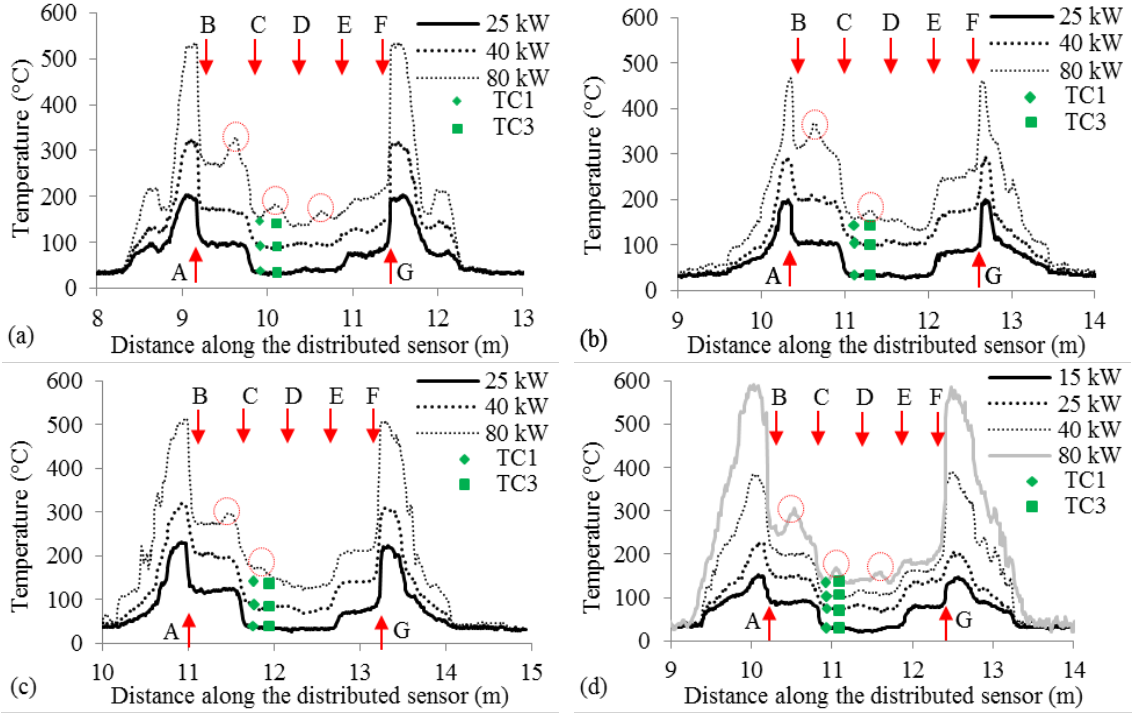

Figure 6.7. Measured temperature in: (a) Beam 1; (b) Beam 2; (c) Beam 3; (d) Beam 4

As indicated in Figures 6.7(a)–(d), air temperatures up to 600 °C were measured by the distributed fiber optic sensors. However, as the distance from the compartment

increased, the temperature dropped to room temperature. While the air temperatures measured by the fiber optic sensors generally agree with the compartment thermocouple measurements (comparison between Figure 6.3 and Figure 6.7), a direct comparison is not made since the sensors were not co-located inside the compartment.

The optical fibers between points A and G measured the temperature distributions within the concrete beams. Non-uniform temperature distributions are demonstrated in Figure 6.7. Overall, temperatures between B and C and between E and F are higher than those between C and E. This is because fiber sections B-C and E-F were closer to the exterior surfaces of the beam than C-E. Furthermore, temperatures between B and C are higher than those between E and F. This is because the bottom surface was closer to fire and had a higher temperature than the top surface, and B-C and E-F were respectively close to the bottom and top surfaces of the beams.

When the air temperature was below 400 °C corresponding to a HRR of below 40 kW, temperatures over B-C, C-D, D-E, and E-F sections were approximately constant in the four beams. However, when the air temperature exceeded 400 °C, peaks appeared as indicated by the dashed circles in Figure 6.7. For instance, as shown in Figure 6.7(a), the temperature at the middle of C-D was higher than that at C or D at a HRR of 80 kW. Additionally, the thermal gradients of C-D and D-E were approximately the same and symmetrical to D. This behavior is believed to be due to cracking in the concrete.

6.3.4. Effects of Concrete Cracking and Spalling. Concrete cracking and spalling may break the distributed fiber optic sensor in two mechanisms, as respectively illustrated in Figures 6.8(a) and (b): opening (Mode I) and sliding (Mode II).

Crack opening in concrete influenced the heat transfer behavior but had no effect on sensor function as evidenced from the test results since there was no bond between the optical fiber and its protective sheath. However, sliding can be detrimental to the distributed sensor by bending the optical fiber into an acute angle, which results in a significant signal loss and thus a reduction of signal-to-noise ratio. Fibers in a section of spalling concrete were sheared off as illustrated in Figure 6.8(c). Once broken, the distributed sensor with PPP-BOTDA measurements was no longer functional. However, BOTDR measurements can still be taken from one end of the optical fiber to determine the location of the spalling.

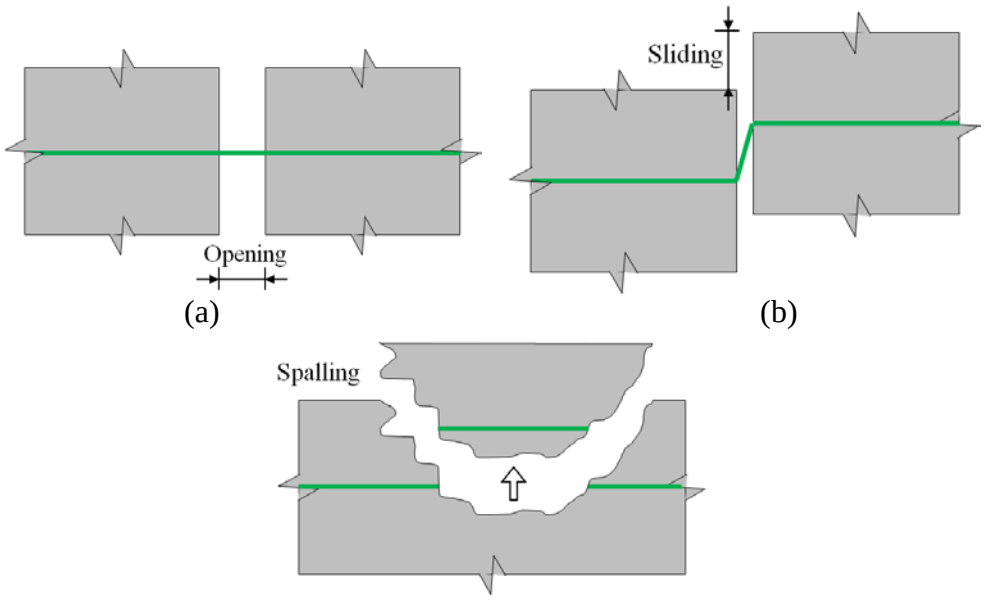

Figure 6.8. Fiber optic sensor behavior under: (a) crack opening (mode I); (b) crack sliding (mode II); (c) spalling

6.4. SUMMARY

Based on the test results, the main findings can be summarized:

A fused silica SMF with PPP-BOTDA was used to measure spatially-distributed internal temperature of concrete exposed to fire. This new approach in structural-fire applications is advantageous over conventional thermocouples and grating-type fiber optic sensors since it can provide a detailed temperature data (every 2 cm along the fiber). The availability of dense data allows for enhanced visualization and understanding of the concrete behavior. The distributed fiber optic sensor survived from crack opening as observed in all tests. At the moment of concrete spalling, the sensor was broken and the PPP-BOTDA measurements based on the optical fiber loop were no longer available. However, BOTDR can still be used to detect the location of concrete spalling from one end of the broken fiber.

Non-uniform temperature distributions were observed in all tested beams. Cracks in concrete were identified at sharp peaks of the measured temperature distribution since the cracks were filled with hot air, thus accelerating the local heat transfer from the surface to inside of the concrete beams. Prior to concrete cracking, the internal temperatures measured with the fiber optic sensor are in good agreement with those of

the bare-bead thermocouples by a relative difference of less than 9 % at 95 % confidence. When concrete cracks appeared, this difference increased because the thermocouples were not able to measure the local temperature changes as the fiber optic sensors captured. Continued development and application of the approach is needed to quantify the uncertainty of measurements under diverse conditions, to investigate the feasibility of crack width determination from measured temperature gradients, and to effectively separate temperature and stain effects on the Brillouin frequency shift for situations where strain measurements are desired.

7. TEMPERATURE MEASUREMENT AND THERMOMECHANICAL ANALYSIS OF STEEL BEAMS EXPOSED TO FIRE

7.1. BACKGROUND

The material properties and geometry of steel structural component subjected to elevated temperatures change with temperature. The Young's modulus and yield strength of steel degrade quickly with increasing temperature for temperatures greater than 400°C (Usmani *et al.* 2003). The degradation of mechanical properties directly reduces the load carrying capacity of a structure. Additionally, thermal expansion can cause changes in connection conditions leading to structural instability and collapse (Sunder 2005). Restraint of thermal expansion can result in large stresses that can cause buckling or yielding of structural members. Therefore, thermal effects can substantially influence the performance of steel structures in fire (Huang and Tan 2003; Tan *et al.* 2007).

To improve the safety of buildings in a fire, extensive experimental investigations of large-scale steel structures have been carried out in the past. Typical measurements in these investigations included temperature, strain, displacement, and load. With the exception of temperature, almost all measurements were obtained from locations outside of the heated zone. For example, Tan *et al.* (2007) and Dwaikat *et al.* (2011) investigated the behavior of steel columns in a furnace with displacements and loads measured using transducers placed outside of the heated zone. Dwaikat *et al.* (2011) applied strain gauges to a section of each steel test specimen located outside of a test furnace to measure localized strains. Li and Guo (2008) subjected steel beams to heating in fire and subsequent cooling and measured loads and deformations outside of the high-temperature zone. Strain gauges were installed on auxiliary members to indirectly determine forces based on force equilibrium. High-temperature resistance-based strain gauges have been reported to be unreliable in structural applications with fire (McAllister *et al.* 2012).

Fiber Bragg grating (FBG) sensors were used by Zhang and Kahrizi (2007) to measure strain and temperature; however, the sensors began to degrade when heated over 300 °C and the fiber gratings were erased completely around 600 °C. Similarly, Huang *et al.* (2010) used long period fiber grating sensors inscribed in optical fibers for strain and temperature measurement up to 700 °C. Both types of gratings had limited thermal stability for fire applications (Venugopalan 2010; Huang *et al.* 2013). Regenerated FBG

sensors with enhanced thermal stability were used to successfully monitor temperature changes in fire by Rinaudo *et al.* (2015). Nevertheless, grating sensors provide measurements only at discrete points. Therefore, distributed fiber optic sensors based on PPP-BOTDA that allows for the measurements along a fiber have recently attracted attention worldwide. However, implementation of distributed fiber optic sensors for structural fire research has not been fully explored.

Based on experimental investigations, analytical (Usmani *et al.* 2001; Huang and Tan 2003) and numerical (Choi 2008; Zhang *et al.* 2012, 2013) studies were carried out, and various computational models were proposed to predict the thermal and mechanical responses of steel beams and columns in fire, including the spatial and temporal temperature distributions and structural deflections.

Thermo-mechanical analysis procedures for structures or structural components in the literature can be categorized as sequentially-coupled or fully-coupled. When the thermal responses can be considered independent of the mechanical responses, a sequentially-coupled thermo-mechanical analysis (Jeffers and Sotelino 2012) can be performed. In this case, thermo-dynamic and heat transfer analyses are first conducted to predict the temperature distributions. Then, the predicted temperature distributions are applied to determine the thermal expansion and temperature-dependent material properties. Finally, mechanical analysis is carried out to predict the structural performance.

When the mechanical response can significantly influence the thermal response, a fully-coupled thermo-mechanical analysis must be performed. In a fully-coupled analysis, the incremental results of the structural model are used to incrementally update the boundary conditions in the thermo-dynamic model.

Both sequentially-coupled and fully-coupled thermo-mechanical analysis require the prediction of temperature distributions. Even though zone models (Cadorin and Franssen 2003; Li and Zhang 2012), computational fluid dynamics models; e.g. the Fire Dynamics Simulator (McGrattan *et al.* 2010), and stochastic models (Bertola and Cafaro 2009) for fire have been developed, it is difficult to accurately predict the resulting temperature distributions. The error in the predicted temperature distribution can result in inaccurate mechanical response of the structure. Most importantly, the error in

temperature distribution and the inaccuracy in mechanical response cannot be quantified without properly measured data, which is difficult to obtain when test objects and sensors are engulfed in flames.

In this study, temperature is measured using a distributed fiber optic temperature sensor under fire conditions. The measured temperature distributions are then applied for enhanced thermal-mechanical analysis of steel beams under combined fire and static loading to assess building code-specified relations for temperature-dependent mechanical properties of the steel. The measured temperatures from the distributed temperature sensor are compared to results obtained using thermocouples. The simulated strains and deflections from the structural analysis are validated using a distributed strain sensor that uses Brillouin scattering and two linear potentiometers, respectively.

7.2. EXPERIMENTAL PROGRAM

The detailed experimental program and specimens are introduced as follows.

7.2.1. Test Specimen and Setup. Three S3×5.7 ASTM A36 low carbon steel "I-shaped" sections (AISC 2011), designated as Beam #1, #2, and #3, were tested under three-point loading in a reconfigurable compartment fire setup ("flame channel") as shown in Figures 7.1(a)–(c). Each beam was 76 mm deep, 59 mm wide, and 1420 mm long. The cross-sectional area and moment of inertia about the strong axis were 1,077 mm^2 and 10^6 mm^4, respectively.

The flame channel, which was located under a 6 m × 6 m (plan) exhaust hood, included three subassemblies: a burner rack, an enclosure, and a specimen loading system. The burner rack (Figure 7.1(b)) had four independent natural gas diffusion burners made of sheet metal 300 mm × 300 mm × 140 mm (length × width × height) in dimension. After the natural gas entered a burner from the bottom, it filled the burner cavity and passed through a 20 mm thick ceramic fiber blanket to distribute the gas. The burners were manually regulated using a needle valve on the gas line, and the energy content of the supplied gas was measured with an expanded uncertainty of less than 2.4% (Bundy *et al.* 2007). An enclosure constructed of square tube steel, cold-formed steel C-profiles and gypsum board lined with thermal ceramic fiber enclosed the space above the burner rack. The enclosure was open at three faces: the bottom and the two ends in

longitudinal direction of the beam, creating the compartment flame dynamics. The heated "compartment" created by the enclosure was approximately 380 mm × 400 mm × 1830 mm (height × width × length) in size and reduced radiative heat losses.

Each beam was simply supported at a clear-span of 1250 mm on two supports constructed of 1-1/2" Schedule 40 pipe (outer diameter: 48 mm), which were supported on concrete blocks. The specimen was loaded by a U-shape 1/2" Schedule 40 pipe (outer diameter: 21 mm) "loading yoke" at the mid-span (Figure 7.1(a)). Both the supporting and the loading pipes were water-cooled with the exiting water temperature controlled to less than 50°C, which limited undesired thermal movement of the boundary conditions. Load was transferred to the yoke with the pulley system shown in Figures 7.1(a) and (c).

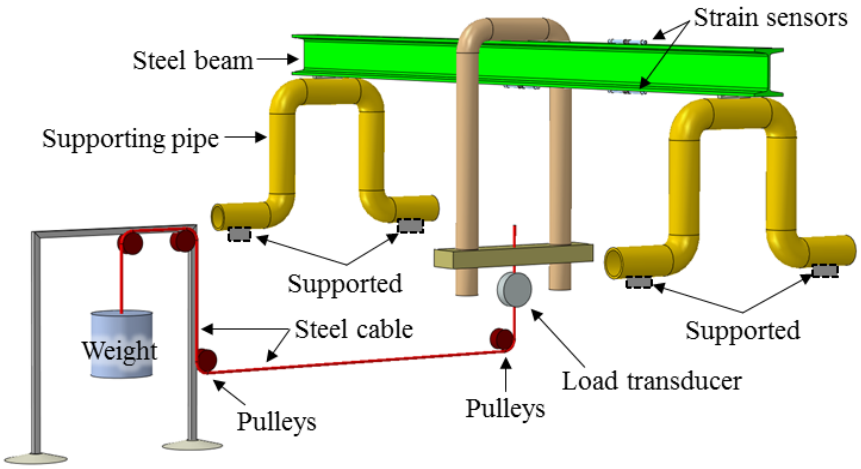

(a) Illustration of specimen loading system

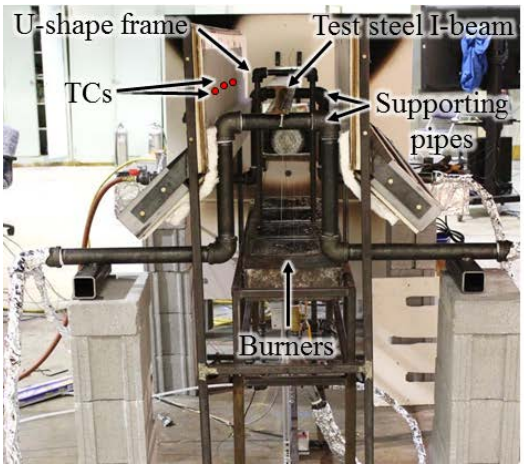

(b) Schematic of test setup

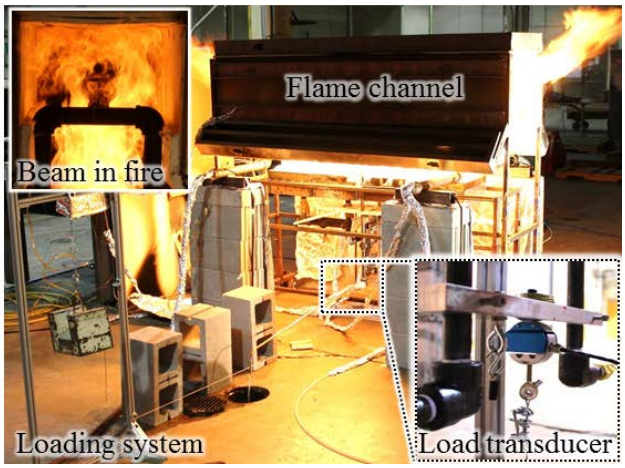

(c) Schematic of specimen loading system

Figure 7.1. Setup of fire test of steel beams

7.2.2. Instrumentation. Data from the fuel delivery system, thermocouples, displacement sensors and a load transducer were measured continuously using a National Instruments data acquisition system (NI PXIe-1082). Thermocouple data were recorded using 24-bit Thermocouple Input Modules (NI PXIe-4353), and load and displacement data were recorded using a high-speed, 16-bit multifunction module (NI PXIe-6363). Data were sampled at 90 Hz with average values and standard deviations recorded in the output file at a rate of 1 Hz.

The Neubrescope data acquisition system was used to perform PPP-BOTDA measurements. In this test, the sampling and spatial resolutions were set at 1 cm and 2 cm, respectively, meaning that data points were sampled at every 1 cm and the Brillouin frequency shifts of two points spaced at no less than 2 cm could be distinguished. The measurement distance was set to 50 m. The scanning frequency ranged from 10.82 GHz to 11.67 GHz, which approximately corresponded to a target temperature range from 20 °C to 1100 °C (Bao and Chen 2015). The reading time varied from 15 seconds to 40 seconds depending on the scanning frequency range.

7.2.3. Distributed Fiber Optic Sensors. Two single-mode optical fibers with dual-layer coating were used as a distributed temperature sensor (DFOS-T) and a distributed temperature and strain sensor (DFOS-ST) with the PPP-BOTDA, respectively.

For strain measurement, the coatings must be removed before the optical fiber is attached to a specimen to ensure effective strain transfer at high temperature. Figures 5.15(a) and (b) show the schematic and prototype of a strain sensor package. The bare optical fiber was passed through two glass tubes (Glass tube 1 in Figure 5.15) in series with a small gap between them, and fixed to the tubes at their far ends using a two-part high-temperature adhesive. The gap between the two tubes was covered with a third tube (Glass tube 2 in Figure 5.15) for additional protection of the fiber. Each Glass tube 1 was fixed near the gap on the steel beam with a clip and laterally constrained at the far end with a ring. The leg of each ring or clip was tightly inserted into a small hole (≈1.4 mm in diameter) pre-drilled on the steel beam. When installed, the two rings and the two clips were aligned using a steel guide bar as depicted in Figure 5.15(b). The strain sensor measures the elongation of steel between the two clips over a base length denoted by d.

To enable large strain measurements, the steel elongation is averaged over a gage length of the sensor, denoted by L. A gage length factor α of the sensor can thus be defined as the ratio of the gage length and the base length, or $\alpha = L/d$ (Huang *et al*. 2010). Since the optical fiber has limited strain capacity before rupture, increasing α allows for an increased strain measurement range, but leads to reduced sensitivity and spatial resolution. In this study, α was designed to be 10, providing a maximum strain capacity of approximately 10,000 με (1%). As shown in Figure 7.2(a), the optical fiber for strain sensing had a stand-off distance of 2.5±0.5 mm from the surface of the specimen.

For temperature measurement, the coatings of the optical fiber were left in place to provide protection during installation. The protective coatings burn off at 300 – 400 °C with negligible influence on the temperature measurement, while the glass core and cladding can survive to temperatures above 1000 °C.

Each beam was instrumented with three strain-temperature sensors as shown in Figure 7.2: DFOS-ST1 and DFOS-ST2 on the bottom flange at mid-span and quarter-span of the beam, respectively, and DFOS-ST3 on the top flange at quarter-span. The optical fiber as a light transmission cable of DFOS-ST1, DFOS-ST2, and DFOS-ST3 or as a distributed temperature sensor (DFOS-T in Figure 7.2) was passed along the top and bottom flanges of each beam to form a closed loop with the Neubrescope for PPP-BOTDA measurements. It was intermittently and loosely attached to the surface of the beam using a two-part high temperature adhesive. The transmission cable and the temperature sensor were closely spaced, and thus subjected to approximately the same temperatures. Therefore, the strain at the location of DFOS can be determined from the Brillouin frequency shift with temperature compensation.

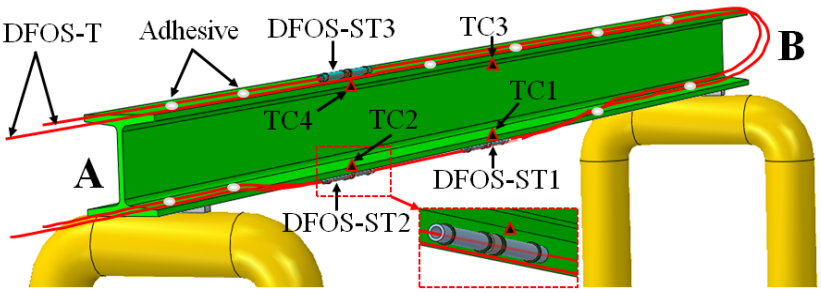

Figure 7.2. Deployment of fiber optic sensors (DFOS) and thermocouples (TC)

7.2.4. Thermocouple, Load, and Displacement Sensors. Each beam was instrumented with four glass-sheathed, K-type, bare-bead thermocouples (24 gage wire) peened into small (diameter < 2 mm) holes drilled into the bottom and top flanges as indicated in Figure 7.2: TC1 and TC3 at mid-span, and TC2 and TC4 at quarter-span. Additional thermocouples were located throughout the test setup to characterize the test environment and monitor safety-relevant temperatures. The thermocouples have a manufacturer-specified temperature standard limit of error of 2.2 °C or 0.75% (whichever value is greater) over a measurement range of 0 – 1250 °C.

A calibrated (linearity: ±0.03%, repeatability: ±0.01%) load transducer by Omegadyn (LCR-100), placed on a spanning bar at the bottom of the loading yoke, was used to measure the applied load as illustrated in Figures 7.1(a) and (c).

The mid-span vertical deflection at the bottom surface of the beam was measured using two linear potentiometers (Novotechnik TR-0050) located below the burner rack and connected to the beam via high-temperature ceramic fibers. The use of two fibers provided compensation for the unwanted influence of gas temperature on displacement measurements with an estimated expanded uncertainty of 0.2 mm (95% confidence).

7.2.5. Test Protocol. Each beam was subjected to both fire and mechanical loading. Figure 7.3 illustrates the fire test protocol. The heat release rate (HRR) was held approximately constant at five target levels: 25 kW, 65 kW, 120 kW, 195 kW, and 350 kW, which corresponded to beam temperatures at TC1 of approximately 200°C, 400°C, 600°C, 850°C, and 1050 °C, respectively. During the test of Beam #2, the gas was turned off for about 20 seconds before the HRR was increased to 120 kW and 195 kW, respectively, to allow for visual observation.

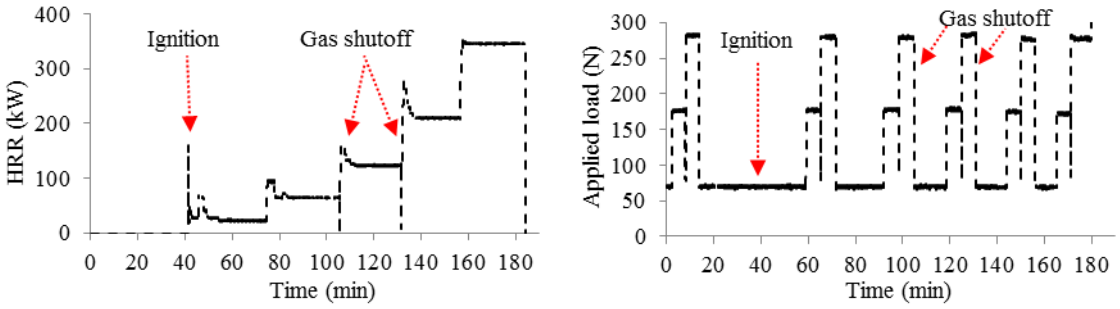

(a) Heat Release Rate (HRR) vs. time (b) Applied load vs. time

Figure 7.3. Protocols of fire test of steel beams

When the HRR was increased to a higher level, the target value was overshot and then quickly regulated down to the expected value. At each HRR level, in addition to the self-weight, the beam was subjected to three levels of loads at the mid-span. For Beam #1, the three loads were approximately 68 N, 98 N, and 126 N, and sustained for 7 minutes, 4 minutes, and 4 minutes, respectively. For Beams #2 and #3, the three loads were approximately 68 N, 176 N, and 285 N, each sustained for 6 minutes.

7.3. THERMO-MECHANICAL ANALYSIS

Traditionally, thermo-mechanical analysis of a structure subjected to fire is a multi-step process that starts with prediction of the fire behavior. Distributions of heat flux to member surfaces are calculated to provide boundary conditions to the thermo-mechanical analysis. Temperature distributions in members are then determined by solving heat conduction equations with the boundary conditions. Finally, the calculated temperature distributions are applied to determine material properties, and thermally induced strain and the structural response can be analyzed. This is a complex process and accumulated errors can be significant.

Researchers have previously investigated the relationship between the temperatures on a beam surface and within the beam. A so-called "section factor" – the ratio of the fire-exposed perimeter to the cross-sectional area – determines the heat transfer rate within the beam. Larger section factors lead to higher heat transfer rates. When the section factor of an unprotected steel section is larger than 300 m^{-1}, the temperature within steel can be considered to be the same as the surface temperature (Li *et al.* 2006; Li and Wang 2012). Since the S3×5.7 beams had a section factor of 353 m^{-1}, the measured surface temperatures at the top or bottom flange were approximately equal to those within the steel. Furthermore, due to the small beam height, the vertical distributions of temperature over the beam height can be approximated as linearly-distributed between the upper and lower surface temperatures (Choi 2008).

7.3.1. High Temperature Steel Properties. Temperature-dependent material properties governing structural behaviors include thermal, mechanical, and deformation properties (Kodur et al. 2010). The thermal properties include thermal conductivity, specific heat, and density. The mechanical properties include yield strength, elastic

modulus, and post-yielding stress-strain relationship. The deformation properties include thermal expansion and creep.

Various models of temperature-dependent mechanical properties were compared by Li and Wang (2012). In their study, four degradation laws of yield strength and elastic modulus of steel at elevated temperatures and their corresponding thermal strains as shown in Figure 7.4 were taken from four standards: EN 1993-1-2 (ECS 2005), AS 4100 (SA 1998), CECS 200 (CECS 2006), and ANSI/AISC 360-10 (AISC 2010). The reduction factors for yield strength and elastic modulus are denoted by η_y and η_E, respectively. $\eta_y = f_{yT}/f_{y20}$, and $\eta_E = E_T/E_{20}$, where f_{y20} and f_{yT} represent the yielding strengths at 20°C and arbitrary temperature T, respectively; E_{20} and E_T represent the elastic moduli at 20 °C and arbitrary temperature T, respectively.

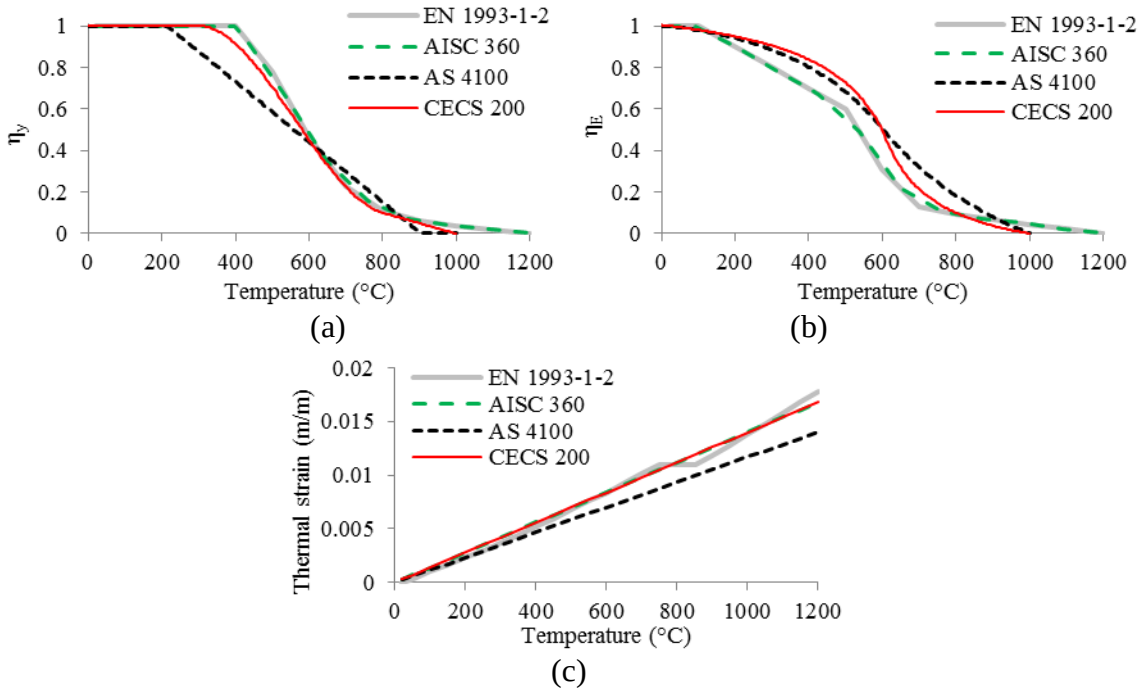

Figure 7.4. Material models: (a) yield strength; (b) elastic modulus; (c) thermal strain

7.3.2. Mechanical Analysis. With the measured temperature distributions and the temperature-dependent properties of the steel, a finite element model of the beam was created using ABAQUS®. Three-dimensional 8-node brick elements (2.5 mm mesh size) with reduced integration (C3D8R) were used to model the simply-supported beam, as

shown in Figure 7.5. Based on the measured temperature distributions and high temperature steel properties, user subroutines “UMAT” and “UTEMP” (SIMULIA 2014) were applied to define the temperature-dependent nonlinear plasticity of the steel and the non-uniform temperature distributions, respectively.

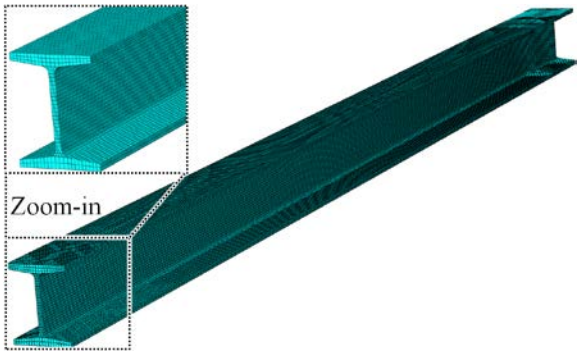

Figure 7.5. Finite element model of steel beam specimen

7.4. RESULTS AND DISCUSSIONS

The experimental and numerical results are presented and discussed below.

7.4.1. Temperature Distribution. Temperature distributions in steel Beam #2 are presented in Figure 7.6 at the five investigated HRR values ranging from 25 kW to 350 kW. At each HRR, the temperature distribution along the beam was not symmetric about the mid-span. The overall temperature distribution pattern varied as the HRR increased.

These results generally agree with the visual observation that the flames were somewhat asymmetrical during the tests. The asymmetry is attributed to variations in the ventilation of the flame channel compartment and in the gas distribution among the four burners. These results illustrate the complex behavior of fire that can cause predicted temperature distributions to differ significantly from actual conditions (Cadorin and Franssen 2003; McGrattan *et al.* 2010).

Figure 7.7 shows a representative temperature time history measured from TC1 in Beam #2. The five plateaus corresponded to the five HRR levels in Figure 7.3(a). At each sustained HRR level, the beam temperature gradually stabilized to a temperature with some variation. The variations were relatively small at low HRR values and became larger as the HRR was increased. To quantify the temperature variations, the mean values and standard deviations were calculated over 15 minutes for Beam #1, and 18 minutes for

Beams #2 and #3 when the mechanical loads were applied at each temperature level. The coefficient of variation for all the thermocouple readings is less than 3.6 %.

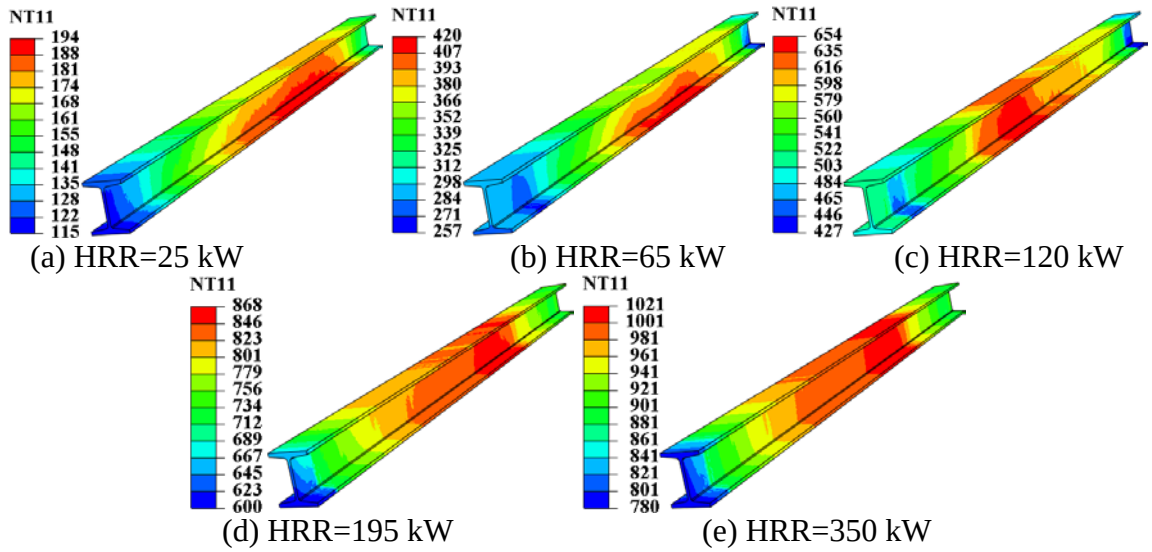

(a) HRR=25 kW (b) HRR=65 kW (c) HRR=120 kW

(d) HRR=195 kW (e) HRR=350 kW

Figure 7.6. Temperature distributions of Beam #2 at various HRRs

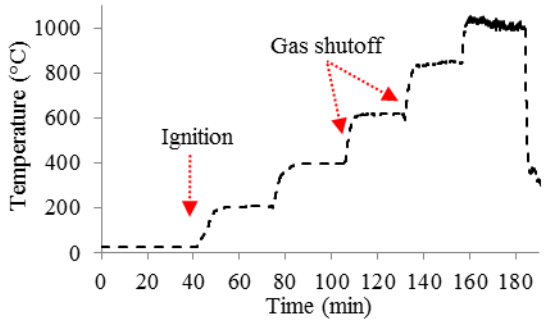

Figure 7.7. Temperature time history measured by thermocouple TC1 in Beam #2

Similarly, to average out the effects of temperature fluctuation, five measurements were made using the DFOS-T at each sustained temperature level. Each measurement was an average over 15 seconds to 40 seconds. The DFOS-T readings have a maximum coefficient of variation of 4%, which was similar to that of the thermocouples. The relative difference between the mean temperatures from the DFOS-T and the thermocouple ranges from -10% to 8%. To understand the statistical significance of the measurement differences, the average of mean temperature differences (four for Beam #1, three for Beam #2, four for Beam #3) was calculated at each HRR level and presented

in Figure 7.8 as an average temperature difference. In addition, the range of the mean differences at 95% confidence level is represented by the error bar in Figure 7.8. It can be observed that the mean difference at 95% confidence level is less than 4.7%, which is acceptable in most engineering applications. The discrepancies may be attributed to several factors. First, the DFOS-T sensor was installed in a slightly different location than the thermocouples. Second, the thermocouple beads were located slightly below the surface of the beam and the DFOS-T slightly above the surface, and thus, the influence of gas temperature variation on the measurements varied. Additionally, the thermocouples were not corrected for radiation.

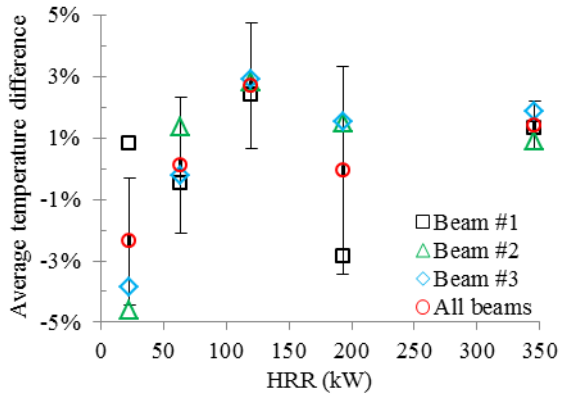

Figure 7.8. Average relative difference between the fiber optic sensor (DFOS-T) and thermocouple (TC) temperature readings

7.4.2. Strain. The simulated strains of Beam #2 under fire and 285 N loading using the mechanical properties specified in the EN1993-1-2 code are presented in Figure 7.9 for the first three HRR levels. They include the effects of thermal elongation due to uniform temperature change, thermal bending due to temperature gradient over the cross section, and mechanical bending due to the applied load.

At the applied load of 285 N, the mechanical bending caused elastic strain only. Creep strain was not explicitly modeled in the thermo-mechanical analysis, although creep was implicitly included in the stress-strain relationship and the measured temperature distributions that were input into the model. Furthermore, the beam changes its position with respect to the heat source when deflected significantly, altering the temperature distribution in beam (Baum 2011). As deflection increases, the influence of

deflection on the temperature distribution was taken into account in thermal analysis through the DFOS-T measurement.

The strains at the bottom flange and mid-span of Beam #2 due to thermal elongation, thermal bending and mechanical bending are presented in Figure 7.10 for the first three HRRs and all loading conditions. Figure 7.10 shows that the thermal elongation accounted for over 95% of thermal induced strain, and the thermal strain accounted for over 95% of total strain. The observation that thermal elongation effects dominated the response is supported by the fact that the top flange of the beam is always subjected to positive strains as illustrated by Figure 7.9.

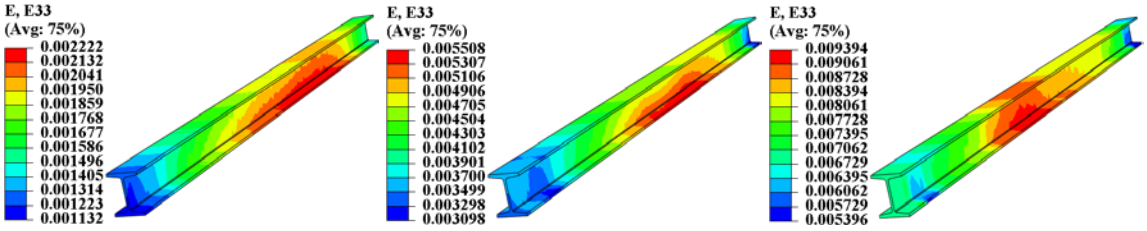

(a) HRR=25 kW (b) HRR=65 kW (c) HRR=120 kW

Figure 7.9. Total strain distributions of Beam #2 under 285 N loading and fire

The simulated strains are also compared in Figure 7.10 with the strains measured by the DFOS-ST1 sensors (average ± one standard deviation of five readings). The variations of the strain measurements – due mainly to temperature fluctuation – are small compared to their average amplitudes. The simulated strains at HRR of 195 and 350 kW are not included in Figure 7.10 because the DFOS-ST sensors failed due to excessive fiber deformation.

In general, the simulated strains under the investigated heating and loading conditions compared well with their corresponding measured strains. To quantify the difference, the strains simulated by finite element analysis using the temperature-dependent properties specified in Figure 7.5 and the measured strains at the three DFOS-ST locations are compared under the highest load applied and HRR up to 120 kW. Similar to Figure 7.8, Figure 7.11 shows the average of relative strain differences at the DFOS-ST locations (three for each beam) at each HRR level, and the margin of error (represented by the error bar) of the data for all beams at 95% confidence level. For the

four temperature-dependent material property models, the overall average strain difference ranges from 9.7% (EN 1993-1-2) to 13% (CECS 200) at 95% confidence level. The EN 1993-1-2 code gives the smallest margin of error.

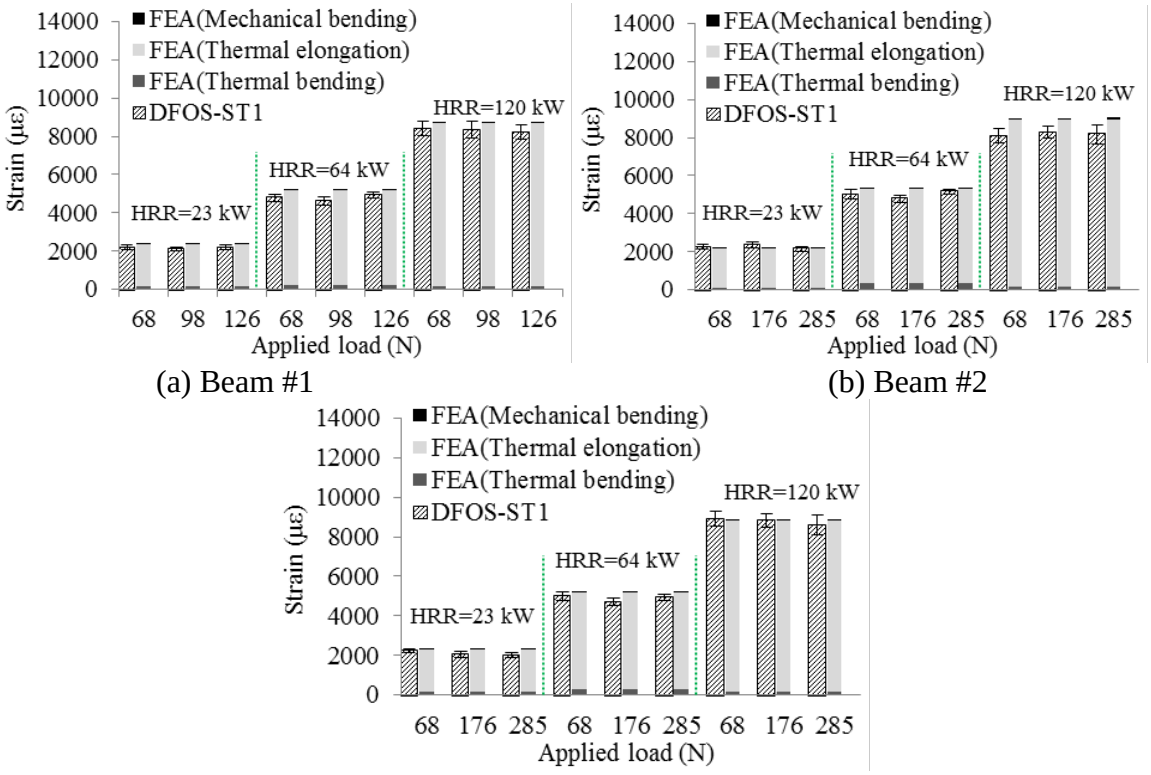

(a) Beam #1 (b) Beam #2

(c) Beam #3

Figure 7.10. Longitudinal strain on the bottom flange at mid-span of steel beams under three-point bending

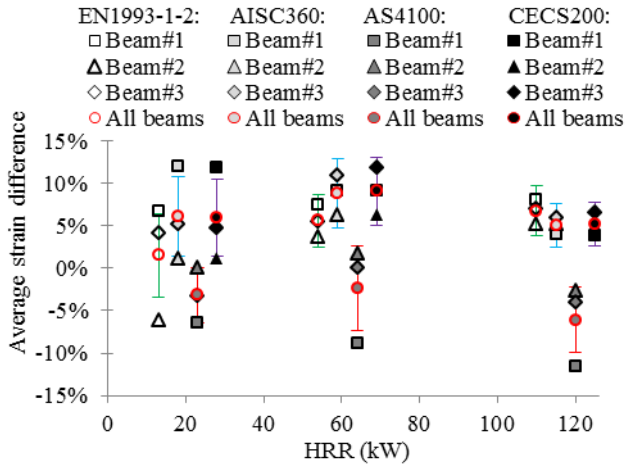

Figure 7.11. Average relative difference between the simulated and measured strains under the highest load

The differences between the simulated and measured strains can be attributed to two main physical phenomena. First, the temperature distribution selected in simulations from five readings could be different from that at the moment of strain measurement. Second, the adopted temperature-dependent properties in simulations may not accurately represent those of the test beam. For example, the temperature-dependent properties suggested in the EN 1993-1-2 code (ECS 2005) are based on the average values from a small number of steel types (Luecke *et al.* 2011). The second point can be further substantiated by the fact that the average strain differences in Figure 7.11 are mostly negative when the material properties specified in AS 4100 code are used since the thermal strain is the smallest as shown in Figure 7.4(c).

7.4.3. Mid-Span Deflection. Figures 7.12(a) and (b) compare the simulated and the measured mid-span deflections for Beam #1 and Beam #2 at all investigated HRRs and applied loads. Beam #3 is not reported because the displacement sensor failed at the start of the test. The measurements from the displacement sensors were corrected for the settlement of supports and thermal elongation of the sensor attachments.

The simulated mid-span deflection used the temperature-dependent material properties specified in EN1993-1-2 (ECS 2005). Figure 7.12 indicates that the simulated and measured results are in good agreement up through 120 kW (about 600 °C beam temperature). The discrepancies at higher temperatures result primarily from not modeling creep. Additional sources of error could come from a mismatch between the adopted temperature-dependent properties and those of the test specimens as well as uncertainties in the displacement and fiber optic sensor measurements. At elevated temperatures, the temperature-corrected displacement measurements are within ±0.2 mm of the manufacturer-specified accuracy of the linear potentiometers.

According to the finite element analysis, 80% to 95% of mid-span deflection was due to thermal bending when the HRR was at 120 kW. Since the thermal gradient of Beam #2 at HRR = 120 kW was smaller than that at HRR = 65 kW, the deflections at HRR = 120 kW were smaller as indicated in Figure 7.12(b). This seemingly surprising result suggests that the temperature distribution in the beam largely depended on the fire dynamics and air circulation in our specific test setup, and that prediction of structure response could be quite inaccurate of uniform heating assumed. The significant

difference in deflection trend between Beams #1 and #2 at HRR = 120 kW was likely due to the gas shutoff during the test of Beam #2. At beam temperatures below 600 °C (HRR < 120 kW in these tests), even the largest applied load of 285 N was insufficient to cause significant deformation of the beam. This was a limitation of the present tests. At beam temperatures above 600 °C, the applied loads were sufficient to cause extensive mechanical deformation through creep and allow for a more differentiated assessment of thermal and mechanical contributions to beam response.

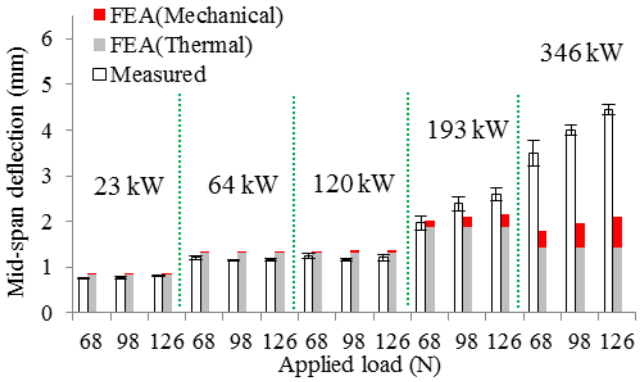

(a) Beam #1

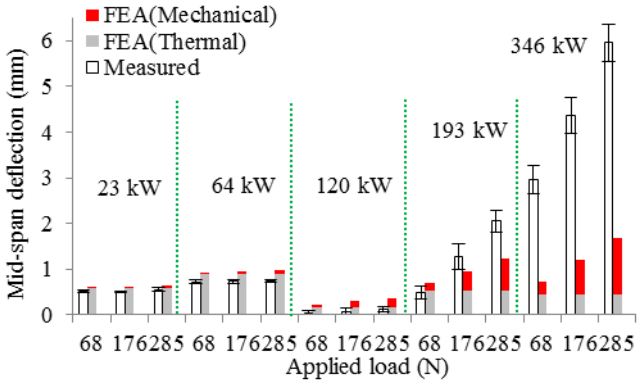

(b) Beam #2

Figure 7.12. Mid-span deflections of S3×5.7 steel beams under three point bending

7.5. SUMMARY

Distributed fiber optic temperature sensors can operate up to at least 1050 °C in fire with adequate sensitivity and accuracy for typical structural engineering applications. The measured temperatures were validated by thermocouple measurements resulting in an average relative difference of less than 4.7% at 95% confidence level.

When HRR was not more than 120 kW, the maximum beam temperature was approximately 600 °C. The computational model provided an acceptable prediction of strains (average relative difference < 13%) and mid-span deflections (0.31 mm maximum difference), when compared to direct strain measurements by distributed fiber optic strain sensors and temperature compensated potentiometers measurements, respectively. The material properties specified in EN 1993-1-2 resulted in the smallest margin of error among the four considered building codes. In our tests, the thermal elongation (not thermal bending) accounted for over 95% of thermal strain, and the thermal strain accounted for over 95% of total strain. At beam temperatures below 600 °C, about 80% to 95% of mid-span deflection was due to the effects of thermal bending.

When HRR was no less than 195 kW, the mechanical loads had a greater influence on the mid-span deflection due to substantial reduction of the mechanical properties of steel and the resulting creep. Without explicitly considering creep effects in the simulations, the deformation was significantly underestimated.

With a gage length factor of approximately 10, the distributed fiber optic strain sensors captured large strains and maintained the fiber integrity until the beam temperatures reached about 600 °C. For large strain measurements at higher temperatures, a gauge length factor of at least 20 is suggested.

8. CONCLUSIONS AND FUTURE WORK

8.1. MAIN FINDINGS FROM OVERALL DISSERTATION WORK

In this dissertation, distributed fiber optic sensors based on the PPP-BOTDA technology are proposed for real-time monitoring of concrete and steel structures under ambient and high temperature conditions. Based on the above comprehensive theoretical, experimental, and numerical investigations, several conclusions can be drawn from this study:

1. The analytical formulae of strain transfer can be used to interpret the strain distributions measured from the distributed fiber optic sensors packaged with polymer coating. In a uniform strain field, inaccurate strain measurements exist at the two ends of the host matrix. An 84-mm length is required to develop 95% of the normal strain for a distributed fiber optic sensor with a dual-layer coating. An abrupt strain change in a host matrix can lead to inaccurate strain measurements. Under uniaxial step loads, an 84-mm length at each side of the loading section is required to develop 95% of the normal strain. For beam members under three-point bending, the length of the inaccurate measurement decreases with the beam's span length. The strain transfer effect does not lead to inaccurate strain measurements in simply-supported beams under uniformly-distributed lateral loads. The strain transfer effect is dependent on the elastic modulus of the host matrix. However, for the commonly-used adhesives, whose elastic moduli are typically within the range of 5–50 GPa, the change of elastic modulus does not significantly influence the strain transfer behavior. Changing the host's elastic modulus from 1 to 80 GPa, causes about 3% change in the normal strain.
2. Standard test measurements of early-age autogenous shrinkage in cement-based materials are in excellent agreement with shrinkage measurements using the proposed optical fiber sensor. A shrinkage-induced crack can be identified from the strain distribution so long as it intercepts the optical fiber. It can be located at the center of strain peak and can be sized based on the magnitude of the strain peak.

3. The distributed fiber optic sensor can be applied to monitor the initiation and propagation of delamination at the overlay-substrate interface. Delamination occurs at the location of each sharp peak that appears on the strain distribution directly measured from the sensor. When the distributed sensor passes through the overlay-substrate interface at spatially distributed locations, delamination at the multiple locations enables the construction of a 3D delamination profile in space and its progression over time with continuous monitoring. The initiation and propagation of delamination at the overlay-substrate interface can be predicted using the finite element model with material properties obtained from standard tests and with cohesive elements used to represent delamination behavior. Delamination takes place when the interfacial traction caused by shrinkage in the overlay exceeds the bond strength of the interface. Thus, delamination can be mitigated by controlling the shrinkage effect of the overlay material and enhancing the bond strength between the overlay and substrate. Once initiated, delamination propagates along the interface and the bending curvature of the overlay and substrate is reduced.
4. The sensitivity coefficient of Brillouin frequency shift for strain measurement is determined to be 5.43×10^{-5} GHz/με. The field-applicable installation method for fiber optic sensors was demonstrated to be effective with full-scale panel tests. Optical fibers can be protected from brutal actions during concrete casting by half mortar cylinders of 12 mm in diameter after the mortar has been cured for at least initial setting time, which is approximately 90 min. The distributed fiber optic sensors that are embedded in concrete are feasible for structural health monitoring. The reduced size of optical fiber and detailed measurement results make them promising for wider applications in flexible pavements, thin bridge decks, and other infrastructures. However, due to the fragility of optical fiber, appropriate procedure should be followed during the installation of optical fiber and construction of the structures.
5. The Brillouin frequency of distributed fiber optic sensors increased quadratically with temperature. The frequency-temperature sensitivity coefficient linearly decreased from 1.113 MHz/°C to 0.830 MHz/°C in the

range of 22–800 °C. The measurement accuracy and precision were ±2.6 and ±5.5 °C, respectively. The Brillouin frequency of the sensors increased linearly with strain. The frequency-strain sensitivity coefficient linearly decreased from 0.054 MHz/με to 0.042 MHz/με in the range of 22–700 °C. The measurement accuracy and precision were ±45 and ±76 με, respectively. At 800 °C, creep became significant, thus reducing the strain sensing precision. The sensors were stable up to 800 °C in heating-cooling cycles or continuous heating processes.

6. The Young's modulus of optical fiber increased linearly from 73 GPa to 80 GPa in the range of 22–700 °C. The ultimate strain decreased from 19,100 με to 6,000 με in the range of 22–800 °C due to chemo-mechanical effect. Approximately 85% of the strain reduction occurred within the first 20 min of heating. Load tests indicated 90% efficiency of the gage length amplification mechanism in application setting. Therefore, a packaged strain sensor with a nominal amplification factor of 11 can potentially increase the measurement range by approximately 10 times of a corresponding bare fiber or from 6,000 (bare fiber sensor) to 60,000 με at 800 °C. Indeed, the packaged sensor was successfully applied to measure the thermal strain of steel up to 10,500 με at 700 °C, which was validated by a commercial dilatometer.
7. Distributed fiber optic sensors survived from crack opening as observed in all tests. At the moment of concrete spalling, the sensor was broken and the PPP-BOTDA measurements based on the optical fiber loop were no longer available. However, BOTDR can still be used to detect the location of concrete spalling from one end of the broken fiber. Non-uniform temperature distributions were observed in all tested beams. Cracks in concrete were identified at sharp peaks of the measured temperature distribution since the cracks were filled with hot air, thus accelerating the local heat transfer from the surface to inside of the concrete beams. Prior to concrete cracking, the internal temperatures measured with the fiber optic sensor are in good agreement with those of the bare-bead thermocouples by a relative difference of less than 9 % at 95 % confidence. When concrete cracks appeared, this

difference increased because the thermocouples were not able to measure the local temperature changes as the fiber optic sensors captured. Continued development and application of the approach is needed to quantify the uncertainty of measurements under diverse conditions, to investigate the feasibility of crack width determination from measured temperature gradients, and to effectively separate temperature and stain effects on the Brillouin frequency shift for situations where strain measurements are desired.

8. Distributed fiber optic temperature sensors can operate up to at least 1050 °C in fire with adequate sensitivity and accuracy for typical structural engineering applications. The thermal elongation (not thermal bending) accounted for over 95% of thermal strain, and the thermal strain accounted for over 95% of total strain. At beam temperatures below 600 °C, approximately 80% – 95% of mid-span deflection was due to the effects of thermal bending. Without explicitly considering creep effects in the simulations, the deformation was significantly underestimated. With a gage length factor of approximately 10, the distributed fiber optic strain sensors captured large strains and maintained the fiber integrity until the beam temperatures reached about 600 °C.

8.2. RELATED PUBLICATIONS

For more details, the above main findings can be referred to a number of papers that have been published or submitted for potential publication during the Ph.D. dissertation work. These papers are listed as follows:

8.2.1. Peer Reviewed Journal Papers. The following journal papers that are associated with this dissertation were published or submitted for publication.

Bao, Y., Valipour, M., Meng, W., Khayat, K.H., Chen, G. (2017). “Distributed fiber optic sensor-enhanced detection and prediction of shrinkage-induced delamination of ultra-high-performance concrete bonded over an existing concrete substrate,” Smart Materials and Structures, https://doi.org/10.1088/1361-665X/aa71f4.

Bao, Y., Chen, Y., Hoehler, S.M., Smith, M.C., Bundy, M., Chen, G. (2016). “Experimental analysis of steel beams subjected to fire enhanced by Brillouin scattering-based fiber optic sensor data,” *ASCE Journal of Structural Engineering*, 04016143.

Bao, Y., Chen, G. (2016). “High temperature measurement with Brillouin optical time domain analysis,” *Optics Letters*, 41(14), 3177–3180.

Bao, Y., Chen, G. (2016). “Temperature-dependent strain and temperature sensitivities of fused silica single mode fiber sensors,” *Measurement Science and Technology*, 27(6), 65101–65111.

Bao, Y., Tang, F., Chen, Y., Meng, W., Huang, Y, Chen, G. (2016). “Concrete pavement monitoring with PPP-BOTDA distributed strain and crack sensors,” *Smart Structures and Systems*, 18(3), 19p.

Bao, Y., Meng, W., Chen, Y., Chen, G., Khayat, K.H. (2015). “Measuring mortar shrinkage and cracking by pulse pre-pump Brillouin optical time domain analysis with a single optical fiber,” *Materials Letters*, 145, 344–346.

Bao, Y., Chen, G. (2015). “Strain distribution and crack detection in thin unbonded concrete pavement overlays with fully distributed fiber optic sensors,” *Optical Engineering*, 55(1), 011008.

Bao, Y., Hoehler, S.M., Smith, M.C., Bundy, M., Chen, G. (2017). “Temperature measurement and crack detection in concrete beam subjected to fire using PPP-BOTDA fiber optic sensors,” submitted.

Bao, Y., Huang, Y., Chen, G., Zhou, Z. (2017). “Strain transfer effect for distributed fiber optic sensors packaged with polymer coating,” submitted.

Bao, Y., Hoehler, S.M., Bundy, M., Chen, G. (2017). “Fire experiment of steel-concrete composite beams instrumented with Brillouin scattering based distributed fiber optic sensors,” submitted.

8.2.2. Peer Reviewed Conference Papers. The following conference papers that are associated with this dissertation were published or submitted for publication.

Bao, Y., Hoehler, S.M., Choe, L., Klegseth, M., Chen, G. (2017). “Monitoring early-age shrinkage strain and temperature distributions in full-scale steel-concrete composite beams with distributed fiber optic sensors,” Proc. Int. Workshop Struct. Health. Monit. 2017, Stanford University, CA.

Bao, Y., Chen, Y., Hoehler, S.M., Smith, M.C., Bundy, M., Chen, G. (2016). “Temperature and strain measurements with fiber optic sensors for steel beams subjected to fire,” Proc. Structures in Fire 2016, Princeton University, NJ.

Bao, Y., Chen, G. (2015). “Fully-distributed fiber optic sensor for strain measurement at high temperature.” Proc. Int. Workshop Struct. Health. Monit. 2015, Stanford University, CA.

Bao, Y., Chen, G., Chen, Y., Huang, Y., Palek, L. (2015). “Strain distribution in thin concrete pavement panels under three-point loading to failure with pump pre-pulse Brillouin optical time domain analysis,” Proc. SPIE Smart Structures/NDE 2015, San Diego, CA, USA.

Bao, Y., Cain, A.J., Chen, Y., Chen, G., Huang, Y., Palek, L. (2015). “PPP-BOTDA strain measurements in thin concrete panels under truck loads,” Proc. SHMII, Torino, Italy.

Bao, Y., Chen, G., Meng, W., Tang, F., Chen, Y. (2015). “Kilometer-long optical fiber sensor for real-time railroad infrastructure monitoring to ensure safe train operation,” Proc. Joint Rail Conference 2015, San Jose, CA, USA.

8.3. FUTURE WORK

In the derivation of strain transfer formulae, potential debonding at the interface between glass fiber and polymer coating is not taken into account. To understand the strain transfer effect at elevated temperatures is critical for strain measurement. Specifically, future research can be directed to address the following topics:

1. Single fiber pull out tests to characterize the interfacial properties for the interface between glass fiber and polymer coating at normal and elevated temperatures.
2. Investigation of the strain transfer effects for distributed fiber optic sensors embedded in various host matrixes subjected to elevated temperatures.
3. Implementation of developed distributed fiber optic sensing technologies in large-scale specimens for further validation.
4. Investigation of the durability (i.e. service life) of the distributed fiber optic sensors in different harsh environments.

BIBLIOGRAPHY

Ansari F, Yuan L, (1998), Mechanics of bond and interface shear transfer in optical fiber sensors. Journal of Engineering Mechanics, 124(4), 385–394.

Akçaoğlu T, Tokyay M, Çelik T, (2005), Assessing the ITZ microcracking via scanning electron microscope and its effect on the failure behavior of concrete. Cement and Concrete Research; 35 (2): 358–363.

Al-Attar TS, (2013), A quantitative evaluation of bond strength between coarse aggregate and cement mortar in concrete. European Sci J; 9(6); 46–61.

Alavi AH, Hasni H, Lajnef N, Chatti K, Faridazar F, (2016), Continuous health monitoring of pavement systems using smart sensing technology. Construction and Building Materials, 114, 719–736.

Azenha M, Faria R, Ferreira D, (2009), Identification of early-age concrete temperatures and strains: Monitoring and numerical simulation. Cement and Concrete Composites; 31:369–378.

Bao X, Chen L, (2011), Recent progress in Brillouin scattering based fiber sensors. Sensors, 11, 4152–4187.

Bao X, Chen L, (2012), Recent progress in distributed fiber optic sensors. Sensors, 12, 8601–8639.

Bao Y, Chen G, (2014), Development of bridge girder movement criteria for accelerated bridge construction. NUTC-36966, Center for Transportation Infrastructure and Safety.

Bao Y, Chen G, (2015a), Fully-distributed fiber optic sensor for strain measurement at high temperature. Proc. Int. Workshop Struct. Health. Monit. 2015, Stanford University, CA.

Bao Y, Chen G, (2015b), Strain distribution and crack detection in concrete overlays with pulse pre-pump Brillouin optical time domain analysis. MATC-25-1121-0003-196, Mid-America Transportation Center.

Bao Y, Meng W, Chen Y, Chen G, Khayat KH, (2015a), Measuring mortar shrinkage and cracking by pulse pre-pump Brillouin optical time domain analysis with a single optical fiber. Materials Letters, 145, 344–346.

Bao Y, Cain AJ, Chen Y, Chen G, Huang Y, Palek L, (2015b), PPP-BOTDA strain measurements in thin concrete panels under truck loads. SHMII, Torino, Italy.

Bao Y, Chen G, Chen Y, Huang Y, Palek L, (2015c), Strain distribution in thin concrete pavement panels under three-point loading to failure with pump pre-pulse Brillouin optical time domain analysis. SPIE Smart Structures/NDE 2015, San Diego, CA, USA.

Bao Y, Chen G, Meng W, Tang F, Chen Y, (2015d), Kilometer-long optical fiber sensor for real-time railroad infrastructure monitoring to ensure safe train operation. Joint Rail Conference 2015, San Jose, CA, USA.

Bao Y, Chen G, (2016a), Strain distribution and crack detection in thin unbonded concrete pavement overlays with fully distributed fiber optic sensors. Optical Engineering, 55(1), 011008.

Bao Y, Chen G, (2016b), Temperature-dependent strain and temperature sensitivities of fused silica single mode fiber sensors with pulse pre-pump Brillouin optical time domain analysis. Measurement Science and Technology, 27(6), 65101–65111.

Bao Y, Chen G, (2016c), High-temperature measurement with Brillouin optical time domain analysis of an annealed fused-silica single-mode fiber. Optics Letters, 41(14), 3177–3180.

Bao Y, Chen Y, Hoehler SM, Smith MC, Bundy M, Chen G, (2016a), Experimental analysis of steel beams subjected to fire enhanced by Brillouin scattering-based fiber optic sensor data. ASCE Journal of Structural Engineering, 04016143.

Bao Y, Tang F, Chen Y, Meng W, Huang Y, Chen G, (2016b), Concrete pavement monitoring with PPP-BOTDA distributed strain and crack sensors. Smart Structures and Systems, 18(3), 405–423.

Bao Y, Chen Y, Hoehler SM, Smith MC, Bundy M, Chen G, (2016c), Temperature and strain measurements with fiber optic sensors for steel beams subjected to fire. Proc. Structures in Fire 2016, Princeton University, NJ.

Bao Y, Ghasr MT, Ying K, Chen G, Zoughi R, (2016d), Evaluation of mechanically stabilized earth walls with microwave synthetic aperture radar imaging. ASCE Journal of Geotechnical and Geoenvironmental Engineering, 02816002.

Bao, Y., Valipour, M., Meng, W., Khayat, K.H., Chen, G, (2017), Distributed fiber optic sensor-enhanced detection and prediction of shrinkage-induced delamination of ultra-high-performance concrete bonded over an existing concrete substrate. Smart Materials and Structures, doi:10.1088/1361-665X/aa71f4.

Bao Y, Ghasr MT, Ying K, Chen G, Zoughi R, (2017), Microwave synthetic aperture radar imaging for nondestructive evaluation of mechanically stabilized earth walls. Materials Evaluation, American Society for Nondestructive Testing, 75(2), 177–184.

Bentz DP, (2000), Fibers, percolation, and spalling of high-performance concrete. ACI Mater J, 97(3), 351–359.

Bentz DP, (2008), A review of early-age properties of cement-based materials. Cement and Concrete Composites, 38, 196–204.

Bernini R, Minardo A, Ciaramella S, Minutolo V, Zeni L, (2011), Distributed strain measurement along a concrete beam via stimulated Brillouin scattering in optical fibers. Int. J. Geophysics, 2011, 710941.

Bjøntegaard Ø, Hammer TA, Sellevold EJ, (2004), On the measurement of free deformation of early age cement paste and concrete. Cement and Concrete Composites, 26, 427–435.

Blackshire JL, Sathish S, (2002), Near-field ultrasonic scattering from surface-breaking cracks. Applied Physics Letters, 80, 3442.

Boyce WE, DiPrima RC, (2001), Elementary Differential Equations and Boundary Value Problems, 7th ed. John Wiley & Sons, Inc., Hoboken, NJ, USA.

Burnham T, (2013), Thin concrete pavements and overlays – ongoing MnROAD research, 2013 NCC Spring Meeting, Philadelphia, PA. CP Tech Center.

Chan YW, Li VC, (1997). Age effect on the characteristics of fibre/cement interfacial properties. J Mater. Sci, 32, 5287–5292.

Chen G, Sun SS, Pommerenke D, Drewniak JL, Greene GG, McDaniel RD, Belarbi A, Mu HM, (2005), Crack detection of a full-scale reinforced concrete girder with a distributed cable sensor. Smart Materials and Structures, 14, 88–97.

Chen G, Huang Y, Bao Y, Palek LG, Burnham T, (2014), Unbonded portland cement concrete overlay/pavement monitoring with integrated grating and scattering optical fiber sensors. Report NUTC-41896, Center for Transportation Infrastructure and Safety.

Chen Y, Tang F, Bao Y, Chen G, Tang Y, (2015a), Corrosion monitoring of steel bar in mortar using Fe-C coated long-period fiber gratings. Corrosion 2015, Dallas, TX, USA.

Chen Y, Tang F, Bao Y, Tang Y, Chen G. (2015b). Corrosion monitoring of steel rebar by long-period fiber grating sensors coated with a thin Fe-C layer. SPIE Smart Structures/NDE 2015, San Diego, CA, USA.

Chen Y, Tang F, Bao Y, Chen G, Tang Y, (2016), Fe-C coated long period fiber grating sensors for steel corrosion monitoring. Optics Letters, 41(13), 344–346.

Cox HL, (1952), The elasticity and strength of paper and other fibrous materials. Br. J. Appl. Phys., 3, 72–79.

Deif A, Martín-Pérez B, Cousin B, Zhang C, Bao X, Li W, (2010), Detection of cracks in a reinforced concrete beam using distributed Brillouin fibre sensors. Smart Materials and Structures, 19, 1–7.

Diehl T, (2008), On using a penalty-based cohesive-zone finite element approach, part I: elastic solution benchmarks. Int J Adhesion Adhesives, 28, 237–255.

Duck G, LeBlanc M, (2000), Arbitrary strain transfer from a host to an embedded fiber-optic sensor. Smart Materials and Structures, 9, 492–497.

Farmand-Ashtiani E, Cugnoni J, Botsis J, (2013), Monitoring and characterization of the interfacial fracture in sandwich composites with embedded multiplexed optical sensors. Composite Structures, 96, 476–483.

Farrar CR, Worden K, An Introduction to Structural Health Monitoring. Philosophical Transactions of the Royal Society A, 365, 2007, 303–315.

Farrar CR, Lieven N, Damage Prognosis: The Future of Structural Health Monitoring. Philosophical Transactions of the Royal Society A, 365, 2007, 623–632.

Feng X, Zhou J, Sun C, Zhang X, Ansari F, (2013), Theoretical and experimental investigations into crack detection with BOTDR-Distributed fiber optic sensors. Journal of Engineering Mechanics, 139, 1797–1807.

Ghasr MT, Bao Y, Ying K, Combs KM, Zoughi R, Chen G, (2014), Nondestructive evaluation of mechanically stabilized earth walls with frequency-modulated continuous wave radar. MATC-25-1121-0003-196, Mid-America Transportation Center.

Glass GK, Buenfeld NR, (1997), The presentation of the chloride threshold level for corrosion of steel in concrete. Corrosion Science, 39, 1001–1013.

Glisic B, Inaudi D, (2011), Development of method for in-service crack detection based on distributed fiber optic sensors. Structural Health Monitoring, 11(2), 161–171.

Goldfeld Y, Klar A, Damage identification in reinforced concrete beams using spatially distributed strain measurements. Journal of Structural Engineering, 04013013, 1–11.

Huang Y, Zhou Z, Zhang Y, Chen G, Xiao H, (2010), A temperature self-compensated LPFG sensor for large strain measurements at high temperature. IEEE Trans. Instr. & Meas., 59(11), 2997–3004.

Huang Y, Fang X, Zhou Z, Chen G, Xiao H, (2013), Large-strain optical fiber sensing and real-time FEM updating of steel structures under the high temperature effect. Smart Materials and Structures, 22(1), doi:10.1088/0964-1726/22/1/015016.

Hoult NA, Ekim O, Regier R, (2014), Damage/deterioration detection for steel structures using distributed fiber optic strain sensors. Journal of Engineering Mechanics, 140(12), 04014097.

Jammalamadaka SN, Markandeyulu G, Kannan E, Balasubramaniam K, (2008), Development of a magetnetostrictive transducer for nondestructive testing of concrete structures. Applied Physics Letters; 92: 044102.

Jiang Y, Leung CKY, Ng M, Motavalli M, Feltrin G, Gsell D, (2009), Delamination detection in an I-section glass fiber reinforced plastic beam with an optical fiber-based stress wave method. Smart Materials and Structures, 18, 065003.

Jiang Z, Lian J, Yang D, Dong S, (1998), An analytical study of the influence of thermal residual stresses on the elastic and yield behaviors of short fiber-reinforced metal matrix composites. Mater. Sci. Eng. A, 248(1-2), 256–275.

Kishida K, Li CH, Nishiguchi K, (2005), Pulse pre-pump method for cm-order spatial resolution of BOTDA. Proc. of SPIE 5855 (17th Int. Conf. on Optical Fiber Sensors), Bruges, Belgium, May.

Kishida K, Li CH, (2006), Pulse pre-pump-BOTDA technology for new generation of distributed strain measuring system. Proc. Structural Health Monitoring and Intelligent Infrastructure, London, UK, 2006: 471–477.

Kouzmina I, Chien CK, Bell P, Fewkes E, (2010), Corning CPC Protective Coating – An overview, Report No. WP3703, Corning Inc, USA.

Krauß M, Hariri K, (2006), Determination of initial degree of hydration for improvement of early-age properties of concrete using ultrasonic wave propagation. Cement and Concrete Composites, 28, 299-306.

Lajnef N, Chatti K, Chakrabartty S, Rhimi M, Sarkar P, (2013), Smart pavement monitoring system. Report: FHWA-HRT-12-072, Federal Highway Administration (FHWA), Washington, DC.

Leung CKY, Yang Z, Xu Y, Tong P, Lee SKL, (2005), Delamination detection in laminate composites with an embedded fiber optical interferometric sensor. Sensor Actuator A-Phys, 119, 336–344.

Leung C, Elvin N, Olson N, Morse TF, He YF, (2000), A novel distributed optical crack sensor for concrete structures, J. Eng. Fract. Mech., 65, 133–148.

Li DS, Li HN, Ren L, Song GB, (2006), Strain transferring analysis of fiber Bragg grating sensors. Optical Engineering, 45(2), 024402.

Li HN, Zhou GD, Ren L, Li DS, (2007), Strain transfer analysis of embedded fiber Bragg grating sensor under nonaxial stress. Optical Engineering, 46, 054402.

Li HN, Zhou GD, Ren L, Li DS. (2009). Strain transfer coefficient analyses for embedded fiber Bragg grating sensors in different host materials. Journal of Engineering Mechanics, 135, 1343–1353.

Li Q, Li G, Wang G, Ansari F, Liu Q, (2002), Elasto-plastic bonding of embedded optical fiber sensors in concrete. Journal of Engineering Mechanics, 128, 471–478.

Li Q, Li G, Wang G, (2003), Elasto-plastic bond mechanics of embedded fiber optic sensors in concrete under uniaxial tension with strain localization. Smart Materials and Structures, 12, 851–858.

Li VC, Lim YM, Foremsky DJ, (1995), Interfacial fracture toughness of concrete repair materials. Fracture Mechanics of Concrete Structures, Proc. FRAMCOS-2, edited by Folker H. Wittmann: 1329–1344.

Li X, Wang J, Bao Y, Chen G, (2017), Cyclic behavior of damaged reinforced concrete columns repaired with environment-friendly fiber-reinforced cementitious composites. Engineering Structures, 136, 26–35.

Li X, Bao Y, Wu L, Yan Q, Ma H, Chen G, Zhang H, (2017), Thermal and mechanical properties of green engineered cementitious composites after exposure to high temperatures. Construction and Building Materials.

Li X, Bao Y, Xue N, Chen G, (2017), Bond strength of steel bars embedded in high-performance fiber-reinforced cementitious composite before and after exposure to elevated temperatures. Fire Safety Journal.

Lu S, Xie H, (2007), Strengthen and real-time monitoring of RC beam using ‘intelligent’ CFRP with embedded FBG sensors. Construction and Building Materials, 21, 1839–1845.

Lu S, Jiang M, Sui Q, Sai Y, Jia L, (2015), Damage identification system of CFRP using fiber Bragg grating sensors. Composite Structures; 125: 400–406.

Liao M. (2011), Towards fracture mechanics-based design of unbonded concrete overlay pavements. PhD Dissertation, University of Minnesota, Twin Cities.

Ling H, Lau K, Cheng L, Chow K, (2005), Embedded fibre Bragg grating sensors for non-uniform strain sensing in composite structures. Measurement Science and Technology, 16(12), 2415–2424.

Lura P, Couch J, Jensen O, Weiss J, (2009), Early-age acoustic emission measurements in hydrating cement paste: Evidence for cavitation during solidification due to self-desiccation. Cement and Concrete Research, 39, 861–867.

Meng W, Lunkad P, Kumar A, Khayat KH, (2016), Influence of silica fume and PCE dispersant on hydration mechanisms of cement. Journal of Physical Chemistry C, 120(47), 26814–26823.

Meng W, Khayat K, (2016a), Experimental and numerical studies on flexural behavior of ultra-high performance concrete panels reinforced with embedded glass fiber-reinforced polymer grids. Journal of Transportation Research Board: Transportation Research Record, 2592, 38–44.

Meng W, Khayat K, (2016b), Flexural performance of ultra-high performance concrete ballastless track slabs. Joint Rail Conference 2016, No. 5814, April 12–15, Columbia, SC, USA.

Meng W, Valipour M, Khayat KH, (2017), Optimization and performance of cost-effective ultra-high performance concrete. Materials and Structures, 50(1), 29p.

Meng W, Khayat KH, (2017), Improving flexural behavior of ultra-high performance concrete by rheology control. Composites Part B: Engineering, 117, 26–34.

Meng W, Khayat KH, (2017), Mechanical properties of ultra-high-performance concrete enhanced with graphite nanoplatelets and carbon nanofibers. Composites Part B: Engineering, 107, 113–122.

Meng W, Samaranayake VA, Khayat KH, (2017), Factorial design and optimization of UHPC with lightweight sand. ACI Materials Journal.

Minakuchi S, Banshoya H, Ii S, Takeda N, (2012), Hierarchical fiber-optic delamination detection system for carbon fiber reinforced plastic structures. Smart Materials and Structures, 21, 105008.

Morey WW, Meltz G, Glenn WH, (1989), Fiber optical Bragg grating sensors. Proc. SPIE, 1169, 98–107.

NCPTC, (2007), Guideline to concrete overlay solutions, ACPA Publication TB021P, Washington DC: National Concrete Pavement Technology Center.

Ouyang C, Landis E, Shah SP, (1991), Damage assessment in concrete using quantitative acoustic emission. Journal of Engineering Mechanics, 117 (11), 2681–2698.

Pak YE, (1992), Longitudinal shear transfer in fiber optic sensors. Smart Materials and Structures, 1, 57–62.

Pei H, Li Z, Zhang B, Ma H, (2014), Multipoint measurement of early age shrinkage in low w/c ratio mortars by using fiber Bragg gratings. Materials Letters, 131, 370–372.

Raoufi K, (2010), Restrained shrinkage cracking of concrete: the influence of damage localization. PhD Dissertation, Purdue University, West Lafayette, USA.

Russell HG, Graybeal BA, (2013), Ultra-high performance concrete: a state-of-the-art report for the bridge community. Report FHWA-HRT-13-060, Federal Highway Administration.

Semperlotti F, Conlon SC, (2010), Nonlinear structural surface intensity: an application of contact acoustic nonlinearity to power flow based damage detection. Applied Physics Letters, 97, 141911.

Seoa DS, Choi HB, (2014), Effects of the old cement mortar attached to the recycled aggregate surface on the bond characteristics between aggregate and cement mortar. Construction and Building Materials, 59(30), 72–77.

Shen B, Hubler M, Paulino GH, Struble LJ, (2008), Functionally-graded fiber-reinforced cement composite: processing, microstructure, and properties. Cement and Concrete Composites; 30(8): 663–673.

Shin HC, Lange DA, (2012), Effects of overlay thickness on surface cracking and debonding in bonded concrete overlays. Can J Civ Eng; 39: 304–312.

Sirkis JS, Haslach HW, (1991), Complete phase strain model for structurally embedded interferometric optical sensors. J. Intell. Mater. Syst. Struct., 23.

Sierra-Pérez J, Torres-Arredondo MA, Güemes A, (2016), Damage and nonlinearities detection in wind turbine blades based on strain field pattern recognition: FBGs, OBR and strain gauges comparison. Composite Structures; 135: 156–166.

Stephen JM, (2012), Fiber Bragg grating sensors for harsh environments. Sensors, 12, 1898–1918.

Tang F, Bao Y, Chen Y, Tang Y, Chen G, (2016), Impact and corrosion resistances of duplex epoxy/enamel coated plates. Construction and Building Materials, 112, 7–8.

Takeda S, Aoki Y, Nagao Y, (2012), Damage monitoring of CFRP stiffened panels under compressive load using FBG sensors. Composite Structures, 94, 813–819.

Wang C, Tang GC, Wang WB, Zevallos M, Alfano RR, Kassir MK, (2006), Detection of subsurface defects using a hybrid heating and cooling imaging technique. Applied Physics Letters, 88, 194101.

Wang XH, Jacobsen S, He JY, Zhang ZL, Lee SF, Lein HL, (2009), Application of nanoindentation testing to study of the interfacial transition zone in steel fiber reinforced mortar. Cement and Concrete Research, 39(8), 701–715.

Wu Z, Xu B, Takahashic T, Haradaa T, (2008), Performance of a BOTDR optical fibre sensing technique for crack detection in concrete structures. Struct. Infrastruct. Eng., 4, 311–323.

Xu D, Banerjee S, Wang Y, Huang S, Cheng X, (2015), Temperature and loading effects of embedded smart piezoelectric sensor for health monitoring of concrete structures. Construction and Building Materials, 76, 187–193.

Zhang Q, Cheng Z, Cui C, Bao Y, He J, Li Q, (2017), Analytical model for frictional resistance between cable and saddle of suspension bridges equipped with vertical friction plates. ASCE Journal of Bridge Engineering, 22(1), 04016103.

Zhang Q, Pei S, Cheng Z, Bao Y, Li Q, (2017), Theoretical and experimental studies on internal force transfer mechanism of perfobond rib shear connector group. ASCE Journal of Bridge Engineering, 23, 04016112.

Zhao Y, Ansari F. (2001), Quasi-distributed fiber-optic strain sensor: principle and experiment. Applied Optics, 40, 3176–3181.

VITA

Yi Bao was born in Shijiazhuang, Hebei Province, the People's Republic of China in 1987. He entered Southwest Jiaotong University, Chengdu, China, in 2005, and received his bachelor's degree in Civil Engineering in June 2009. He was awarded the *Si Shi Yang Hua Medal*, which was the highest honor no more than one from a thousand students at Southwest Jiaotong University, and the *Provincial Outstanding Graduates*, which was the highest honor of graduates in China. The Graduate School of Southwest Jiaotong University offered him the *Fellowship for Exceptional New Graduate Students* and *The First Class Scholarship* for his master's study and exempted the mandatory entrance exam because of his outstanding academic performance. He received his master's degree in Bridge and Tunnel Engineering in December, 2011. He was the *Speaking Representative* of over 5000 students to be graduating in the Graduation Ceremony in June 2009, and the Speaking Representative of graduate students in the Opening Ceremony in September 2009.

Yi Bao enrolled in the Ph.D. Program in Civil Engineering at Missouri University of Science and Technology, Rolla, Missouri, USA, in August 2012. He served as a Graduate Research and Teaching Assistant from August 2012 to August 2016, and the Manager of the System Process and Assessment Research (SPAR) Laboratory from August 2014 and July 2017. In December 2015, he was selected as one of the seven students in the *Graduate Leadership Development Program* and certified by the President and four Provosts of the University of Missouri System for successful completion of the one year Program. In August 2016, he was appointed the *Missouri S&T Inaugural Franklin Y. Cheng Teaching Scholar* and independently taught the course *Structural Analysis* for two semesters (Fall Semester in 2016 and Spring Semester 2017). In April 2017, he was awarded the *Academic Excellence – Outstanding Ph.D. Student Achievement Award* by the Academy of Civil Engineers in the Department of Civil, Architectural and Environmental Engineering. In July 2017, he graduated with a Ph.D. degree in Civil Engineering from Missouri University of Science and Technology, Rolla, Missouri. He was a student member of ASCE, SEI, ACI, and ASME.